

WIRELESS SENSING AND ACQUISITION SYSTEM FOR NON DESTRUCTIVE
EVALUATION AND STRUCTURAL HEALTH MONITORING

By

Deepak Kumar

A DISSERTATION

Submitted to
Michigan State University
in partial fulfillment of the requirements
for the degree of

Electrical Engineering – Doctor of Philosophy

2021

ABSTRACT

WIRELESS SENSING AND ACQUISITION SYSTEM FOR NON DESTRUCTIVE EVALUATION AND STRUCTURAL HEALTH MONITORING

By

Deepak Kumar

Wireless sensing and communication techniques are superior and preferred over tethered counterparts. Wireless system has already replaced or replacing commonly used data transmission methods for applications such as voice communication, internet, sensing, monitoring, etc. Recently, real-time infrastructure or asset monitoring for safety critical application is gaining attention, due to its ease of better visibility and predictive maintenance. A few of those applications belong to industries such as aerospace, defense, oil and gas, nuclear, etc., which require top of the line materials and an extra level of attention to safety. Every material or product used for such applications need to go through extensive testing and evaluation to mitigate any risk of failure. The next generation nondestructive evaluation system would provide sensing and characterization capabilities from raw materials to the final product for manufacturing on factory grounds as well as monitoring products' desired operation in their respective in-service conditions. However, the current evaluation and internet-of-things (IoT)-based monitoring techniques have limited capabilities and cannot meet the sensitivity, range, versatility, and scalability requirements for these applications while being economical and maintenance-free. In this work, the current challenges associated with traditional NDE and SHM methods have been described and an alternative approach is proposed using new wireless sensing mechanisms.

First, a wireless near-field high-Q sensing resonator is described, which has a high sensitivity to dielectric changes in composites and polymers. Second, a battery-free wireless communication system with enhanced range is demonstrated that overcomes high power requirements and radio frequency (RF) clutter issues. Third, passive (resistive and capacitive) sensors are integrated with the battery-free RFID platform and the sensor information is transmitted via a hybrid data frame with digital ID and analog sensor data. Fourth, the hybrid data frame is exploited further, an active

piezoelectric transducer pair is used to actuate an acoustic pulse and measure time-of-flight (ToF) via the battery-free RFID tag, without using a power-hungry analog to digital conversion approach. The RFID-based wireless sensing system is versatile, scalable, and economically superior to battery-based IoT nodes and it can last for decades in field conditions without any routine maintenance that truly opens the pathway for embedded sensing in next generation NDE systems.

This dissertation is dedicated to my beloved family. . .

ACKNOWLEDGEMENTS

My last few years at MSU have been very enjoyable, exciting, enlightening, and enriching. I have a lot to be thankful for and I would like to express my gratitude to all people whom I have worked with and who have helped me learn and grow during this PhD.

First and foremost, I would like to express my deepest gratitude to my advisor, Dr. Yiming Deng, who in many ways has molded my professional life. He has given his time and patience to make me what I am today and for which I am forever indebted. Next, I am thankful to the rest of my committee members Dr. Premjeet Chahal, Dr. Satish Udpa, Dr. Lalita Udpa, and Dr. Venkatesh Kodur for their valuable suggestions and feedback through my PhD work. I am especially thankful to Dr. Chahal for guiding me during my turbulent times and encouraging me both professionally as well as personally. His inspirational ideas to tackle difficult engineering problems, support during failure, and encouragement to retry was exceptional.

I would like to thank the US Department of Transportation (DOT), Gas Technology Institute, Chicago (GTI) and Consolidated Edison, New York for sponsoring my research and making all this work possible, especially Arthur Buff, Ernest Lever and Vijay Srinivasan. I sincerely appreciate the MSU's College of Engineering and Department of Electrical and Computer Engineering for multiple fellowships and travel grants. Special thanks to Mr. Brain Wright, Mr. Gregg Mulder, Mr. Cameron Crump, and Mrs. Roxanne Peacock for all technical and logistical help.

Having spent most of my time in and around the lab, I'm very thankful to previous members Dr. Chaofeng Ye, Dr. Anders Rosell, and Dr. Zhiyi Su for their valuable advices and welcoming when I joined the lab. I was extremely lucky to find great friends who made this PhD a better experience; Saran, Saikat, Suhas, Anmol, and Paul. I would like to mention other colleagues and friends Xiaodong Shi, Mohand Alzuhiri, Dr. Oleksii Karpenko, Dr. Anton Efremov, Dr. Saptarshi Mukherjee, Dr. Portia Banerjee, Dr. Vivek Rathod, Rajendra Prasath, Eric Tarkleson, Subrata Mukherjee, Srijan Datta, Guillermo Huanes-Alvan, Fares Alharbi, Xuhui Huang, Zi Li, Bharath Shenoy, Ciaron Hamilton and everyone else in NDEL who offered a great opportunity to learn from

the vastly different expertise and research directions.

Finally, I would like to thank my parents, Kuldeep and Kavita, and little sister, Bharti, for constant sources of love, support, and encouragement throughout my life. Special shout-out to Satya, Kamal, Kirnesh, and Karan who never fails to inspire and entertain me. I am also thankful to Cara for all her continuous support during my PhD journey. I dedicate this thesis to them.

TABLE OF CONTENTS

LIST OF TABLES	x
LIST OF FIGURES	xii
CHAPTER 1 INTRODUCTION	1
1.1 Motivation for NDE and SHM applications	3
1.2 Near-field Dielectric Inspection Methods for NDE	5
1.2.1 Capacitive Imaging	6
1.3 Far-field Inspection Methods for SHM	8
1.3.1 Battery based Sensor Tags	8
1.3.1.1 Passive Resistive and Capacitive Sensor Tag	8
1.3.1.2 Active Ultrasonic Sensor Tag	9
1.4 Scope of wireless systems in NDE and SHM	10
1.4.1 Wireless High-Q resonators for NDE	11
1.4.2 Battery-free Wireless Sensor Tags for SHM	11
1.5 Thesis Organization	12
CHAPTER 2 WIRELESS NEAR-FIELD HIGH-Q SENSING RESONATOR FOR DI- ELECTRIC EVALUATION OF COMPOSITES AND POLYMERS	14
2.1 Introduction	14
2.2 Theory and Design	17
2.2.1 Single Element Probe @ 5 MHz	17
2.3 Measurement and Characterization	19
2.3.1 Dielectric Reference Measurements	19
2.4 Dielectric Imaging	23
2.4.1 CFRP Imaging	26
2.4.2 GFRP Imaging	27
2.4.3 Polyethylene Imaging	28
2.5 Array Design and Measurement	29
2.6 Summary	32
CHAPTER 3 WIRELESS FAR-FIELD HARMONIC RFID COMMUNICATION PLAT- FORM FOR ENHANCED RANGE	33
3.1 Introduction	33
3.2 Design	37
3.2.1 Harmonic RFID Interrogator	37
3.2.2 Harmonic RFID Tag	41
3.2.2.1 RFID IC	42
3.2.2.2 RFID Antenna	42
3.3 Results	44
3.4 RF Analysis of Harmonic Communication	47

3.5	Discussion, Challenges and Limitations	51
3.6	Summary	52
CHAPTER 4 PASSIVE SENSOR INTEGRATION WITH ADC-FREE RFID TAG FOR		
	ULTRA-LOW POWER OPERATION	53
4.1	Introduction	53
4.2	Analog RF Sensing	57
4.2.1	Design	58
4.2.1.1	3D Printed Pressure Sensor	58
4.2.1.2	Harmonic RF Sensor Tag	61
4.2.1.3	Harmonic RF Interrogator	63
4.2.2	Results	64
4.2.3	Discussion and Limitations	68
4.3	Hybrid RFID Sensing	69
4.3.1	Design	70
4.3.1.1	Hybrid Single-Frequency RFID Tag Architecture	71
4.3.1.2	Hybrid Harmonic-Frequency RFID Tag Architecture	74
4.3.1.3	Hybrid Multi-Frequency Interrogator	78
4.3.2	Results	80
4.3.2.1	Wireless Demonstration	80
4.4	Summary	89
CHAPTER 5 ACTIVE SENSOR INTEGRATION WITH ADC-FREE RFID TAG FOR		
	ULTRA-LOW POWER OPERATION	90
5.1	Introduction	90
5.2	Design	91
5.2.1	Active Sensing Architecture	92
5.2.2	Integrating Acoustic Actuation Transducer	92
5.2.3	Integrating Acoustic Detection Transducer	94
5.2.3.1	Acoustic continuous wave detection	95
5.2.3.2	Acoustic pulse detection	95
5.3	Results	96
5.3.1	Wireless Acoustic Actuation and Detection Demonstration	96
5.3.1.1	Detection of Acoustic Time-of-Flight in Steel	96
5.4	Summary	97
CHAPTER 6 CONCLUSION AND FUTURE WORK		
	99	
6.1	Summary	99
6.2	Future Work	100
6.2.1	Imaging using an array	100
6.2.2	Miniaturization	100
6.2.3	Ultrasonic Material Characterization	101
APPENDICES		102

APPENDIX A	AN RF BACKSCATTERER SYSTEM FOR REAL-TIME MULTI-SENSING APPLICATIONS	103
APPENDIX B	IDENTIFICATION AND SENSING SYSTEM (ISS): AN OPEN SOURCE RFID PLATFORM	120
BIBLIOGRAPHY		135

LIST OF TABLES

Table 2.1: Comparison of commonly used NDE Methods for composites and polymers . . .	16
Table 2.2: Dimensions of the fabricated sensor probe	18
Table 2.3: Dimensions of the polyamide sample	23
Table 2.4: Dimensions of the aluminum sample	25
Table 2.5: Dimensions of the CFRP sample	26
Table 2.6: Dimensions of the GFRP sample	27
Table 2.7: Dimensions of the HDPE sample	28
Table 2.8: Dimensions of the array probe	30
Table 3.1: Dimensions of the Hairpin bandpass filter	39
Table 3.2: Dimensions of the five stage bandpass filter	41
Table 3.3: Dimensions of the hRFID antenna	43
Table 4.1: Commercially available RFID ICs with sensitivity data	56
Table 4.2: Dimensions of the 3D-printed pressure sensor	60
Table 4.3: Dimensions of the analog pressure sensor tag	62
Table 4.4: Data frame format for Digital ID with Analog Sensor Data Reply	70
Table 4.5: Data frame format for Analog Sensor Data Reply	70
Table 4.6: Dimensions of the designed 915 MHz antenna	74
Table 4.7: Dimensions of the designed 434 MHz antenna	77
Table 4.8: Dimensions of the designed 868 MHz antenna	78
Table 5.1: Data frame format for Digital ID with Acoustic Transducer Data Reply	92
Table A.1: Dimensions of the 915 MHz antenna	106

Table B.1: Data frame format for Digital ID Reply	122
Table B.2: Data frame format for Digital ID with Sensor Data Reply	122
Table B.3: 4-bit codes for different sensing parameters	122
Table B.4: 8-bit codes for different sensor types	123

LIST OF FIGURES

Figure 1.1: Illustration of application for NDE and SHM at different levels	2
Figure 1.2: Example illustration of NDE and SHM for same product with different stakeholders	3
Figure 1.3: Schematic of conventional capacitive imaging; (A) Using impedance analyzer, (B) Differential bridge circuit, (C) LC resonator	7
Figure 1.4: Schematic of conventional capacitive probe interaction with dielectric sample under test with an example imaging output plot	7
Figure 1.5: Battery-based passive sensor nodes acquiring data from digital or analog resistive or capacitive sensor	9
Figure 1.6: Battery-based active sensor node with acoustic signal actuating and detecting capabilities for monitoring mechanical properties	10
Figure 2.1: Schematic of the LC tank along with the fabricated sensor probe	18
Figure 2.2: Measurement setup for the single probe	18
Figure 2.3: Measured S_{11} (magnitude and phase) of the single LC sensor probe	19
Figure 2.4: Frequency response of the standard dielectric materials (Teflon = 2.1, Plexiglass = 3.1) with known relative permittivity	20
Figure 2.5: Frequency response of the composites and polymers with different dielectric constants	21
Figure 2.6: Frequency response of the conductive materials with different conductivity	21
Figure 2.7: Frequency response (magnitude and phase) of GFRP with defect and no defect	22
Figure 2.8: Change in resonance frequency for increasing depth of sub-surface defects in polyamide target	23
Figure 2.9: Schematic of the dielectric imaging setup	24
Figure 2.10: Measurement setup for dielectric imaging with the single probe mounted on a X-Y raster scanner	24

Figure 2.11: (A) Image of the aluminum target with dimensions, (B) Imaging results for profiling of defects using single probe	25
Figure 2.12: (A) Image of the CFRP target, (B) Imaging results for profiling of defects using single probe	26
Figure 2.13: (A) Image of the GFRP target, (B) Imaging results for profiling of defects using single probe	27
Figure 2.14: (A) Image of the HDPE target, (B) Imaging results for profiling subsurface defects in HDPE target	28
Figure 2.15: Schematic of the designed array probe along with the dimensions	30
Figure 2.16: Measured frequency response of the 1 x 4 array probe under no loading conditions	30
Figure 2.17: Measured results for GFRP with surface defects for (A) All four elements of the array, (B) Focused frequency Shift in fourth element of the array	31
Figure 3.1: Range limiting phase noise issue with conventional RFID system	34
Figure 3.2: Hypothesis for harmonic communication towards range enhancement	35
Figure 3.3: The hRFID communication system	35
Figure 3.4: The hRFID communication platform using conventional UHF system	38
Figure 3.5: Hairpin bandpass filter, F1 (2.6-3.4 GHz): (A) Schematic with dimensions, and (B) Simulated and measured S-parameters	39
Figure 3.6: Five stage bandpass filter, F2 (1.7-1.9 GHz): (A) Schematic with dimensions, and (B) Simulated and measured S-parameters	40
Figure 3.7: (A) Schematic of the designed hRFID antenna along with its dimensions, and (B) Measured frequency response of RFID IC and hRFID antenna with conjugate matching points	43
Figure 3.8: Measured backscattered signal visualized using a spectrum analyzer, with a transmitted power of +8 dBm and a read range of 0.35 m: Received signal at the fundamental and the third harmonic frequency with and without the RFID tag in the interrogator's field of view	44

Figure 3.9: Measured backscattered signal visualized using a spectrum analyzer, with a transmitted power of +8 dBm and a read range of 0.35 m: Reference signal at the second harmonic frequency generated using a frequency doubler and the down converted signal at the fundamental frequency after mixing	46
Figure 3.10: Received third harmonic signal from the designed hRFID tag.	47
Figure 3.11: Received backscattered power at the interrogator, with transmitted EIRP of 36 dBm, from the designed hRFID tag for both the fundamental frequency and the harmonic frequency operation.	48
Figure 3.12: Power budget analysis of backscattering based communication system: (A) Detection range using fundamental and harmonic bands with no tag losses, and (B) Detection range using fundamental and harmonic bands with 5 and 10 dB losses, respectively.	49
Figure 3.13: Effects of the IC sensitivity on the RFID read range with fundamental and harmonic communication.	51
Figure 4.1: Example battery-free wireless sensing system architecture for the pipeline infrastructure	57
Figure 4.2: Air cavity-based fully 3D printed pressure sensor	58
Figure 4.3: Exploded view of 3D printed pressure sensor with three main components	59
Figure 4.4: Fully assembled 3D printed pressure sensor with component annotation and dimensions	59
Figure 4.5: (A) Pressurizing chamber (pipe) with integrated pressure sensor, (B) Schematic of the measurement setup, and (C) Fabricated pressure sensor	60
Figure 4.6: Measured impedance at 2 GHz for pressure range from 0 to 20 psi with a direct wired connection using vector network analyzer (VNA)	61
Figure 4.7: Schematic of the pressure sensing harmonic RF tag along with its dimensions. Signal received using 2 GHz antenna forwarded to the hybrid coupler for phase shift according to the integrated pressure sensor and the second harmonic signal with double shifted phase, generated using diode frequency doubler, is transmitted out using 4 GHz patch antenna	62
Figure 4.8: Simulated and measured frequency response; (A) Fundamental (2 GHz) and (B) Harmonic antenna (4 GHz)	63

Figure 4.9: Schematic of the harmonic RF Interrogator consist of a VNA for RF source and phase measurement unit, transmitting and receiving antennas, and miscellaneous RF peripheral circuits for communicating with the harmonic RF sensor tag	63
Figure 4.10: Simulated frequency response of the designed phase shifting hybrid coupler with a variable reactance from 6.82 Ω to 36.73 Ω : (A) No power loss is observed at 2 GHz due to changing reactance, (B) A total phase shift of 28.55 $^\circ$ is observed at 2 GHz due to changing reactance	64
Figure 4.11: Measured phase change due to variable reactance introduced with direct current (DC) biasing the varactor diode in a wired configuration ($\Delta\Phi = 18.28^\circ$) using a single frequency approach and wireless configuration ($\Delta\Phi = 36.78^\circ$) using the harmonic frequency approach	66
Figure 4.12: Pressurized polypropylene pipeline setup with the fabricated harmonic RF sensor tag for real-time wireless communication	67
Figure 4.13: Phase change is wirelessly measured using harmonic RF interrogator due to applied pressure ranging from 0 to 20 psi. The linearity of change in phase due to pressure is represented using coefficient of determination ($R^2 = 0.9915$)	68
Figure 4.14: Schematic of the hybrid single-frequency RFID tag	71
Figure 4.15: (A) Schematic of a lumped hybrid coupler with integrated reactance sensors for modulation, (B) Simulated and measured response of the coupler at 915 MHz	71
Figure 4.16: Measured change in phase due to shift in capacitance of the varactor diode using VNA, at 915 MHz	72
Figure 4.17: (A) Measurement setup for testing backreflection at 915 MHz, (B) Measured backreflected signal with digital ID and analog sensor data.	73
Figure 4.18: Meandered Dipole antenna for 915 MHz	73
Figure 4.19: (A) Simulated and Measured frequency response of the 915 MHz antenna, (B) Simulated radiation pattern of the antenna	74
Figure 4.20: Schematic of the hybrid harmonic-frequency RFID tag	74
Figure 4.21: (A) Schematic of a lumped hybrid coupler with integrated reactance sensors for modulation, (B) Simulated and measured response of the coupler at 434 MHz	75
Figure 4.22: Measured change in phase due to shift in capacitance of the varactor diode using VNA, at 434 MHz	76

Figure 4.23: (A) Measurement setup for testing backreflection at 868 MHz, (B) Measured backreflected signal with digital ID and analog sensor data.	76
Figure 4.24: Meandered Dipole antenna for 434 MHz	77
Figure 4.25: (A) Simulated and Measured frequency response of the 434 MHz antenna, (B) Simulated radiation pattern of the antenna	77
Figure 4.26: Meandered Dipole antenna for 868 MHz	78
Figure 4.27: (A) Simulated and Measured frequency response of the 868 MHz antenna, (B) Simulated radiation pattern of the antenna	78
Figure 4.28: Block diagram of the hybrid multi-frequency interrogator	79
Figure 4.29: Wireless setup for hybrid single-frequency RFID communication	80
Figure 4.30: Demodulated hybrid data received at 915 MHz wirelessly from designed RFID tag	81
Figure 4.31: Snapshot of the hybrid single-frequency communication with digital information	81
Figure 4.32: Analog sensor data recorded using oscilloscope from 915 MHz hybrid RFID tag	82
Figure 4.33: Analog sensor data recorded using oscilloscope from 915 MHz hybrid RFID tag; 0.0V input (Red and 1.0V input (Blue))	83
Figure 4.34: Analog sensor data recorded using oscilloscope from 915 MHz hybrid RFID tag; (A) 0.2V, (B) 0.4V, (C) 0.6V, (D) 0.8V	83
Figure 4.35: Difference in reference (RAD) and sensor (SAD) data for different sensor voltage across Varactor	84
Figure 4.36: Wireless setup for hybrid harmonic-frequency RFID communication	85
Figure 4.37: Demodulated hybrid data received at 868 MHz wirelessly from designed RFID tag	85
Figure 4.38: Snapshot of the hybrid harmonic-frequency communication with digital information	86
Figure 4.39: Analog sensor data at harmonic signal recorded using oscilloscope	86
Figure 4.40: Analog sensor data at harmonic signal recorded using oscilloscope; 0.0V input (Red and 1.0V input (Blue))	87

Figure 4.41: Analog sensor data recorded at 868 MHz using oscilloscope; (A) 0.2V, (B) 0.4V, (C) 0.6V, (D) 0.8V	87
Figure 4.42: Difference in RAD and SAD of 868 MHz signal for different sensor voltage across varactor	88
Figure 5.1: Schematic of active sensor integrated hybrid harmonic RFID tag	93
Figure 5.2: (A) Acoustic actuation and detection wired setup, (B) PZT actuation pulse signal generated by microcontroller and detected signal profile with averaging	93
Figure 5.3: Schematic of the PZT integration with non-linear transmission line	94
Figure 5.4: (A) Test setup to check the analog modulation capabilities of RFID tag, (B) Harmonic output of the NLTL is modulated with 200 kHz acoustic signal detected by PZT	95
Figure 5.5: (A) Test setup to check the acoustic pulse modulation capabilities of RFID tag, (B) Demodulated acoustic signal detected by PZT	96
Figure 5.6: (A) Wireless hybrid harmonic RFID tag with integrated PZT setup for acoustic actuation and detection, (B) Picture of the practical setup	97
Figure 5.7: Wireless acquired and demodulated harmonic signal for acoustic signal	98
Figure A.1: Schematic of a passive wireless system with multi-sensing RF tag and Interrogator	105
Figure A.2: UHF RFID Antenna: (A) Schematic of the dipole antenna and dimensions, (B) Simulated and measured frequency response	106
Figure A.3: (A) Schematic of RF-to-DC converter, (B) Input RF power vs Output DC power	107
Figure A.4: (A) Input voltage vs Input current at 100 kHz oscillation frequency, (B) Oscillation frequency in kHz vs required Input power in microwatts	109
Figure A.5: Circuit diagram of the designed multi-sensing module	110
Figure A.6: Sensing information modulation: (A) Schematic of the modulation scheme and (B) Modulated sensor information of 100 kHz and 150 kHz on 908 MHz carrier frequency	111
Figure A.7: Schematic of the RF interrogator radiating +36 dBm EIRP and visualizing the back reflected sensor information using a spectrum analyzer and an oscilloscope	112

Figure A.8: Wired validation: Received side band power of a carrier signal due to first and second sensor with varying input power	114
Figure A.9: Frequency change of temperature and luminescence sensors (A) with linear fit and (B) with second order polynomial fit	115
Figure A.10: The prototype of RF Tag with designed antenna, integrated sensors, and assembled PCB	116
Figure A.11: Wireless demonstration with 9 dBm transmitted power at 908 MHz: Received RF power at multisensor tag vs distance and backscattered	117
Figure A.12: Wireless demonstration with 9 dBm transmitted power at 908 MHz: (A) Frequency spectrum of the demodulated sensor data, and (B) Received sensor information in time domain with a switching frequency of 6 kHz ($\sim 160 \mu\text{s}$)	118
Figure B.1: Schematic of the digital single frequency tag for receiving and transmitting at 915 MHz	121
Figure B.2: (A) Schematic of the designed energy harvester, (B) Measured frequency response of the energy harvester with input power sweep	123
Figure B.3: (A) Measurement setup for ASK modulation at 915 MHz, (B) Measured back reflected RF signal with modulated ID	124
Figure B.4: Schematic of the digital harmonic tag for receiving at 434MHz and transmitting at 868MHz	125
Figure B.5: Schematic of the 434-868 MHz digital RFID tag	125
Figure B.6: (A) Measurement setup for ASK modulation at 434 MHz, (B) Measured back reflected RF signal with modulated ID	126
Figure B.7: Block diagram of the ISS interrogator	127
Figure B.8: (A) Modulated “Query” command on 915 MHz signal, (B) Demodulated received reply “RN16” from 915 MHz	128
Figure B.9: Digital RFID data received at 915 MHz with +7 dBm transmitted power; (A) with 5 inch interrogation distance, (B) with 10 inch interrogation distance	129
Figure B.10: Snapshots of tag and interrogator communication in digital single-frequency mode; (A) Decoded output with 0.0V at tag, (B) Decoded output with 0.2V at tag, (C) Decoded output with 0.4V at tag, (D) Decoded output with 0.6V at tag, (E) Decoded output with 0.8V at tag, (F) Decoded output with 1.0V at tag	130

Figure B.11: Received digital sensor data at 915 MHz 131

Figure B.12: Digital RFID data received at 868 MHz with +7 dBm transmitted power with
10 inch interrogation distance 131

Figure B.13: Snapshots of tag and interrogator communication in digital harmonic-frequency
mode; (A) Decoded output with 0.0V at tag, (B) Decoded output with 0.2V
at tag, (C) Decoded output with 0.4V at tag, (D) Decoded output with 0.6V at
tag, (E) Decoded output with 0.8V at tag, (F) Decoded output with 1.0V at tag . 132

Figure B.14: Received digital sensor data at 868 MHz 133

CHAPTER 1

INTRODUCTION

In the age of artificial intelligence (AI), data is key and the size reflects its worth. The number of sensors and sensing resolution always go hand in hand, therefore, a futuristic world with AI will require integrating more sensors than ever. High resolution sensing is the path forward for mitigating even the minimal risk of any failure. The collected data from installed sensors not only reflect safety parameters but also help predicting necessary maintenance to maximize the operating life of the infrastructure. These upraised requirements has pushed the inspection industry to bring forth the best sensing and data transmission technologies at a faster pace.

The scope of infrastructure safety is very wide and commonly divided into two main categories; Non Destructive Evaluation (NDE) and Structural Health Monitoring (SHM). The difference is NDE and SHM is very narrow but precise, because both mechanisms are put in place for ensuring and increasing safety. NDE works at a more fundamental level with material properties, whereas, the SHM is more concerned about the reliable operation of the designed product for a specific application. Fig.1.1 illustrates the two sides of infrastructure that require either NDE or SHM safety mechanism.

Fundamentally, bulk materials like metals, composites, and polymers are used in various different shapes or forms to create any product. More than 90% of artificially made common use objects belong to one of the material class mentioned here. Therefore, selecting a bulk material is the first step in every product design. Bulk materials come with different properties like conductive or insulating, malleable or ductile, etc. that needs to be quantified for classifying materials into different grades for easier selection and use. The material property quantification methods are usually part of NDE techniques, which can test the material for its electrical or mechanical properties. For example, metals can be classified according to their respective conductivity, stiffness, density, etc., and polymers can have different dielectric permittivity, porosity, etc. These electrical and mechanical properties are interdependent that indirectly gives a measure of each

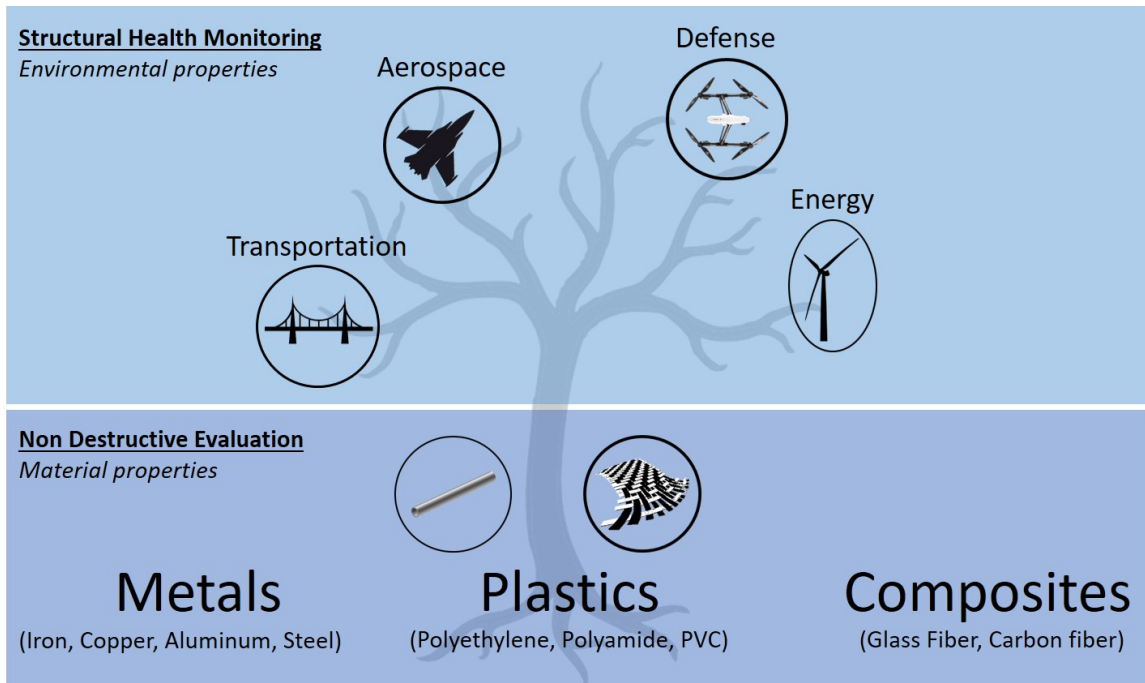


Figure 1.1: Illustration of application for NDE and SHM at different levels

other [1]. Researchers have developed numerous techniques to evaluate material properties at both micro level and bulk level [2–8]. Usually the resolution is inversely proportional to technique’s complexity, therefore, a resolution trade-off can be made according to the application, after-all complexities arise from necessities.

The next step after material selection is product development and operation. The newly developed product hangs on both sides of the evaluation and monitoring methods. To test the quality of the newly developed product, a second evaluation test of material properties can be a good measure to ensure safety and reliability as well as a short operation or dry run under monitoring scenario is also an acceptable method. For example, a medium density polyethylene pipe is manufactured in a plant, a quality assured polyethylene with known material properties would be molded into a new pipe shape, the molding process can alter the properties of the material due to applied heat and curing pressure. Measuring the density or dielectric permittivity again after the mold is a good quality assurance step but the pipe can also be checked with a quick pressure test with monitoring sensors. If the pipe quality comes out well, it can be used in a refinery or chemical plant to transport oil and gas, where its operating condition also needs to be monitored continuously for avoiding any failure.

Therefore, at the operation stage, SHM kicks-in with its capability of measuring environmental/global properties; like pressure, temperature, humidity that contributes to its optimal operation.

Fig.1.2, shows the polyethylene pipe as an example, where the manufacturer is interested in parameters like permittivity and density while user at a refinery plant is interested in pressure and temperature.

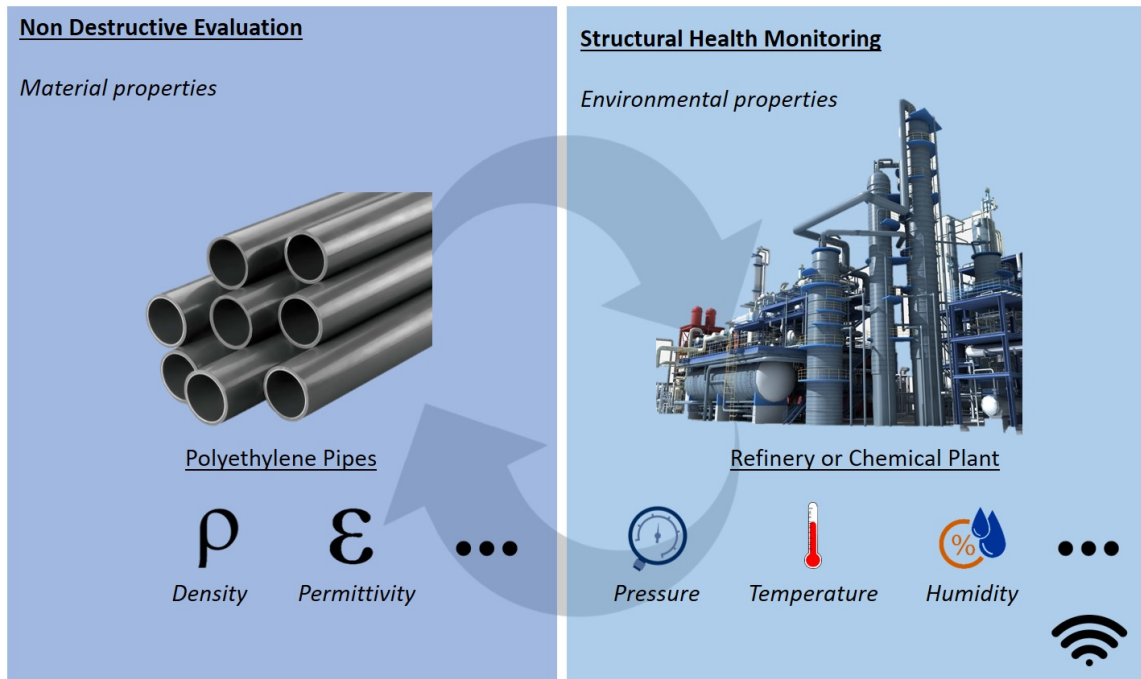


Figure 1.2: Example illustration of NDE and SHM for same product with different stakeholders

1.1 Motivation for NDE and SHM applications

An efficient evaluation and monitoring system requires a comprehensive map of the structural integrity of the target object. Real-time monitoring techniques are best suited for providing instantaneous mapping of the structural stability and the nature of the targeted objects for enhancing predictive maintenance strategies. In general, a target object such as a pipeline is constructed using a combination of fundamental building blocks such as metals, composites, and polymers, whose properties define its structural integrity and mechanical stability.

Structural health monitoring (SHM) of massive infrastructures is necessary due to the rapidly growing urban infrastructure as it has huge impact on human safety and well-being [9, 10]. Struc-

turally deficient infrastructures over time increase the possibility of catastrophic failures leading to loss of human life and economy. There has been several thousand deaths reported around the globe due to infrastructure collapse or failure in the last decade [11–14]. For example, in the United States alone, **PHMSA and NTSB reported numerous pipeline failures in last decade leading to billions of dollars in monetary loss** [15–17]. Although the exponential growth in the number of massive structures has mandated regulatory authorities to enforce rigorous maintenance protocols to mitigate risks for improved safety, the failure incidents are not uncommon. Hence, there is always a growing need to develop NDE and SHM technologies for efficient condition monitoring and evaluation techniques for predictive maintenance. Implementing efficient predictive maintenance strategies enables saving lives and prevents huge economical losses. Moreover, SHM is not limited to just civil infrastructure but can be extended for providing predictive maintenance strategies in multiple domains such as transportation, aerospace, environment, etc.

The common properties that are evaluated for structural integrity are stress, strain, permittivity (ϵ), permeability (μ), and conductivity [18]. These intrinsic properties depend directly on the combination of materials used in manufacturing the object. Any variation in these properties from the standard values will enhance the visibility of the structural integrity of the object. For example, the periodic evaluation of a material's stress and strain is required to detect the occurrence of cracks or other anomalies in walls of a bridge or a pipeline, allowing precautionary safety measures to be enforced in real-time. Apart from the intrinsic properties, extrinsic properties such as humidity, temperature, vibration, moisture, and pressure are also commonly monitored. These properties are important to predict the damage caused due to external environmental factors on the structure. For example, excessive pressure on a pipeline may compromise the structural integrity over time. The combination of the intrinsic and extrinsic properties provides a comprehensive map of the structural integrity of the target object.

In order to promote best predictive maintenance strategies, multiple properties should be monitored in real-time for providing instantaneous feedback on the structural integrity of the target object [19–21]. A number of NDE and SHM techniques are available in the literature for monitor-

ing both the intrinsic and extrinsic properties of the target [22–27].

In general, for electrical probing of the properties of the targeted object, different monitoring and evaluation methods track the three fundamental electrical parameters, resistance (R), capacitance (C), or inductance (L) to estimate the intrinsic or extrinsic properties. For example, by employing microwave based method, the defect of the target material is mapped by tracking the change in impedance across the microwave sensor and indirectly estimating the effective dielectric constant of the target [28–30]. Overall, the monitoring and evaluation of different materials and their intrinsic as well as extrinsic properties fall under major sensing methods that directly or indirectly depends on the change in the three fundamental electrical parameters, Resistance (R), inductance (L), or capacitance (C).

Dielectric imaging is an important technique for evaluating composites and polymers. Electromagnetic methods are well suited for this task as RF waves behave according to the different dielectric properties of the medium. Far-field and near-field imaging techniques have been widely studied for dielectric characterization [31–34]. The far-field imaging resolution is related to the wavelength, therefore, a 300 GHz system is needed for sub-mm resolution. Due to high frequency requirements, the system becomes very complex and the limited availability of RF parts makes it difficult to design such system. The alternative is near-field imaging using fringing fields that can achieve sub-mm resolution with a raster scanning mechanism.

The conventional methods for both near-field NDE inspection and far-field SHM inspection are discussed below.

1.2 Near-field Dielectric Inspection Methods for NDE

The capacitive and microwave imaging techniques are commonly known to evaluate the dielectric properties of composites and polymers. Both techniques operate in near-field region that detects a perturbation in the electric field due to permittivity change. Capacitive and microwave imaging methods can evaluate dielectric materials like CFRP and GFRP for common problems like air bubbles, contamination, delamination, and epoxy saturation [31, 35].

The microwave system operates at a respectively higher frequency compared to capacitive and it uses radiative probes for detection. Due to the radiative nature of microwave probes, making the multidimensional array for simultaneous data acquisition is very difficult. The isolation between array elements is poor, which reduces the sensitivity of the imaging system. The near-field microwave imaging in S or C-band comes across the issue of large aperture window of the probe, which corresponds to a lower spatial resolution due to convolution over a larger volume. The higher frequency operation in X or K-band has complex design and limited component availability issues. The alternative capacitive imaging is better in terms of isolation and circuit design ease. The procedure of conventional capacitive imaging is explained below.

1.2.1 Capacitive Imaging

The capacitive imaging conventionally operate in shortwave frequency range (3–30 MHz) that use a parallel plate capacitive probe for generating fringing fields in its near-by region. The fringing field die off very quickly with the distance that helps with making array probes without isolation issue. The reading mechanism is the primary factor for determining the sensitivity of the probe. In literature, researchers have used direct probing using impedance analyzers for detecting change in capacitance due to the dielectric medium [36]. The direct capacitance probing is too slow for imaging applications. Other capacitive imaging system includes differential reading using bridge circuit, which output change in voltage only due to the change in capacitance. The differential method is fast for imaging but not sensitive due to impedance mismatches, which reflect back most of the input power.

For matching with a capacitive imaging probe, researchers have used series or parallel inductor matching to create an LC resonator. The resonance-based methods are superior over other described methods. However, the Q-factor for wired LC resonator is not very high [37]. In wired configuration the loaded quality factor (Q_L) is measured at resonance frequency (f_o) as shown in Equation.1.1.

$$Q_L = \frac{f_o}{BW} \quad (1.1)$$

where BW is the bandwidth either at -3 dB or -10 dB.

Fig.1.3, shows the conventional capacitive imaging circuits for dielectric evaluations.

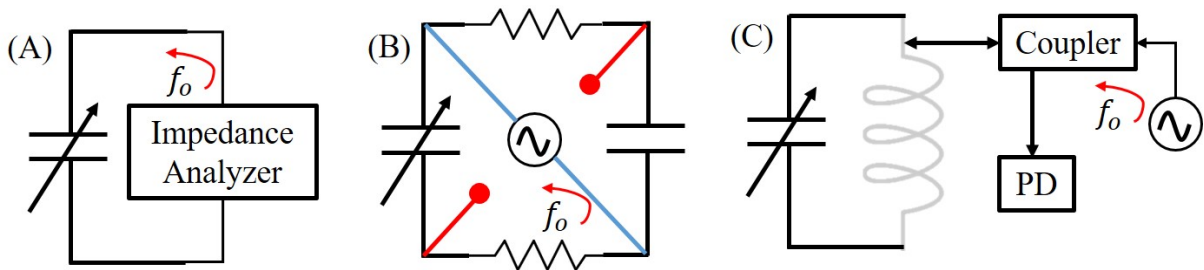


Figure 1.3: Schematic of conventional capacitive imaging; (A) Using impedance analyzer, (B) Differential bridge circuit, (C) LC resonator

The capacitive probe radiates fringing-field that interact with the dielectric sample under test and perturb according to the effective relative permittivity. The measurement setup is shown in Fig.1.4.

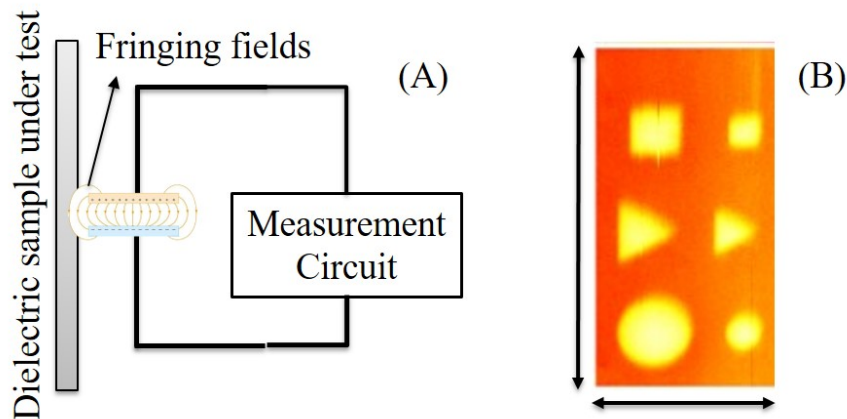


Figure 1.4: Schematic of conventional capacitive probe interaction with dielectric sample under test with an example imaging output plot

The conventional methods do not exhibit high-Q or high sensitivity, therefore, there is a scope of improvement for capacitive imaging in the directions of achieving high-Q, sub-mm resolution, and simultaneous actuation of array elements and detection.

1.3 Far-field Inspection Methods for SHM

Structurally deficient infrastructure increases the probability of catastrophic failure over time, leading to a significant impact on human safety. The demand for developing efficient structural health monitoring (SHM) techniques for promoting effective predictive maintenance strategies is necessary to prevent deaths and substantial economical losses. The evaluation should be nondestructive in nature and should provide instantaneous and accurate feedback on the nature of the structure.

1.3.1 Battery based Sensor Tags

In literature, a number of battery-based SHM platforms are proposed for monitoring and evaluating different structural properties using a plethora of sensors [38,39]. Common battery-based platforms that are used for wireless SHM have an intercommunication link between sensor nodes for real-time data monitoring. Few example platforms are Zigbee, LoraWAN, SigFox, BLE, etc. These platforms are designed for a long-range reliable communication of data from the sensor nodes. Although battery-based SHM platforms are fully evolved, a few challenges still exist in realizing an economical system, such as requirement of **an on-board battery at each node, limited lifetime, and requires periodical maintenance**. The best alternative solution to the current active sensing platforms is to employ infinite lifetime battery-less passive sensing platforms which limits maintenance requirements and reduces the overall cost.

1.3.1.1 Passive Resistive and Capacitive Sensor Tag

The passive (resistance and capacitance) sensors are commonly used for all IoT based infrastructures. The sensor nodes consist of a microcontroller, a wireless communication module, sensing circuit, and a battery to power everything. The microcontroller runs a logic in-loop, which fully wake up the microcontoller and acquires data from the sensing circuitry either using digital bus like SPI, I2C, UART, etc. or using ADC to convert the voltage potential into a digital number. The

acquired data is stored in local microcontroller’s memory that eventually transmitted out to either the cloud or control station using the wireless network. The architecture shown in Fig.1.5.

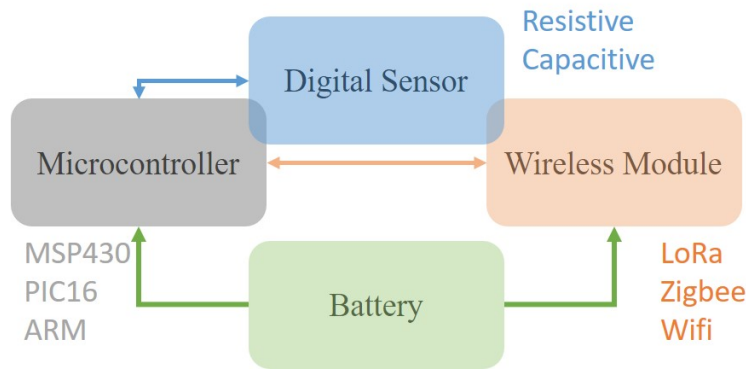


Figure 1.5: Battery-based passive sensor nodes acquiring data from digital or analog resistive or capacitive sensor

The commonly used products in our daily life, for example, smartphones, smartwatches, intelligent lighting, garage opener, pet trackers, thermometers, etc. follows the same architecture as described. Some of these devices last for months before requirement of battery replacement or charging and some need a daily boost, which depends on the amount of activity and use case.

1.3.1.2 Active Ultrasonic Sensor Tag

The active sensors like ultrasonic transducers require an actuation signal for generating an acoustic wave, which travel through a medium under test and change its properties like traveling speed, dispersion, etc. according to the material properties. The traveled signal can be picked up at a distance which holds the time-of-flight information that can be used to back calculate the velocity, young’s modulus, and other mechanical properties [40].

The architecture of such a node includes a microcontroller, wireless module, ultrasonic pulser-receiver module, and a battery as shown in Fig.1.6. The small changes in time-of-flight are picked up by the pulser-receiver module that corresponds to changing material behaviour with traveling acoustic waves. Active ultrasonic sensor tags are commonly used in automotive applications for driver assistance systems.

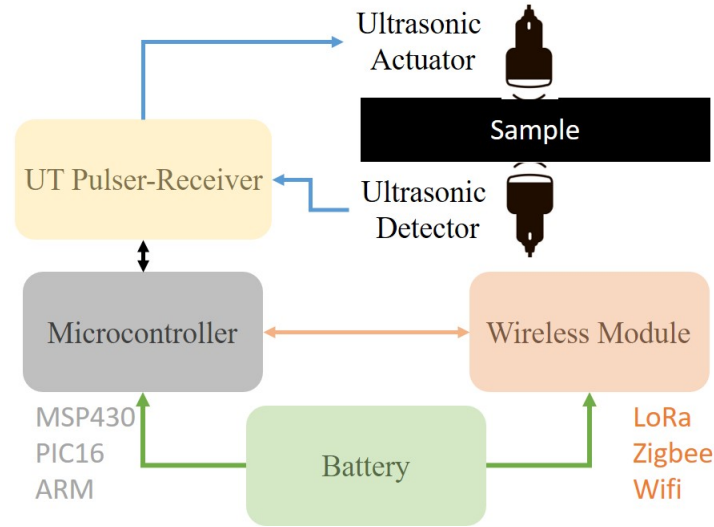


Figure 1.6: Battery-based active sensor node with acoustic signal actuating and detecting capabilities for monitoring mechanical properties

1.4 Scope of wireless systems in NDE and SHM

A number of sensors are necessary to monitor different parameters of interest. These sensors should be efficient and should be able to provide the necessary information in real-time. There are **two methods for probing these sensors, wired and wireless**. The conventional wired techniques involves employing physical wires or probes to connect and obtain data from different sensor nodes. A major limitation of **wired approach** is that it is tedious to run wires on the external surface of the target object from the cluster of sensor nodes making this approach **expensive as well as impractical** for monitoring large infrastructures such as pipelines, bridges, aircrafts, etc. For example, multiple sensor nodes are connected to the pipeline which detects different electrical parameters.

To overcome the impracticality of wired systems to probe large infrastructures **wireless probing of the sensors** is an excellent choice to make the system reliable. The sensor nodes should be able to communicate the sensing information wirelessly to the interrogator or among themselves in an efficient manner to provide an economical solution for evaluating the structural integrity of large objects.

Wireless techniques offer a significant advantage over wired techniques due to the ability to

non-destructively extract data from sensors or transducers that are not in the direct line of sight or located in places that are not easily accessible. With the advent of the internet, and the advancement in wireless communication techniques, a number of conventional systems have been transformed to a "smart system" in which the operation of the system is controlled remotely. The conversion of conventional system to a cloud based remote controlled system commonly known as Internet-of-things (IoT), have revolutionized the world [41]. Applying IoT to create a "Smart" monitoring system for a huge infrastructure by enabling real-time and reliable wireless data communication among the cluster of sensor nodes enhances the visibility of the structure's health [42]. There are two common techniques available in the literature for implementing an IoT based SHM system are either battery-based or battery-less [43, 44].

1.4.1 Wireless High-Q resonators for NDE

The wireless high-Q resonance probe would be ideal for imaging dielectric composites and polymers [45]. The high-Q directly correlates with the sensitivity and small changes due to cracks, delamination, foreign objects, etc. can be easily detected [5, 46]. The wireless mechanism allows to read the resonance of an LC tank without directly loading it with the source impedance and make the probe more immune to higher order modes and spurious noise signal in the system. With a high Q-factor, the change in reflection coefficient due to defect will be significantly higher than a mismatched sensor probe.

1.4.2 Battery-free Wireless Sensor Tags for SHM

A number of battery-free sensing solutions have been proposed in the literature as an alternative low cost system for SHM. One such system is the passive Radio Frequency Identification (RFID) with integrated sensors that are suited to monitor different SHM parameters such as temperature, humidity, and moisture [47, 48]. To collect sufficient information to determine the nature and map the structural integrity of the target, multiple parameter monitoring becomes essential. In the literature, two types of passive multisensing RFID platforms are available, one is a CMOS based

RFID sensing platform, and the other is a passive wireless identification and sensing platform (WISP) [49–51]. These platforms are mostly limited to monitoring extrinsic parameters and very few intrinsic parameters that do not allow a comprehensive structural integrity mapping of the target. In this report, a few passive sensing techniques are proposed that allows to obtain an improved comprehensive map for structural integrity of any large infrastructure.

Comprehensive mapping of the structural integrity of the target requires a host of discreetly positioned sensors or transducers monitoring both intrinsic and extrinsic parameters. To realize an efficient and an economic system, the overall power consumption should be reduced and this can be achieved by adapting passive battery-free sensors or transducers for monitoring different parameters. Furthermore, adapting efficient wireless techniques to retrieve data from the passive sensors or transducers allows remote monitoring of the target. A high performing system requires an efficient retrieval of data, which is possible by developing new routines using conventional modulation techniques which are noise immune, power-efficient, and are capable of modulating multiple sensors or transducer information onto the re-transmitted signal [52–55].

1.5 Thesis Organization

The dissertation thesis is organized as follows:

- Chapter 2 presents the technique to make a wireless near-field high-Q sensing resonator for dielectric evaluation of composites and polymers.
- Chapter 3 introduces the harmonic RFID to enhance the communication range by eliminating the RF clutter.
- Chapter 4 extends the capabilities of RFID-based battery-free communication system by integrating the passive sensors and transmitting a hybrid data packet without increasing any power requirement.
- Chapter 5 exploits the concept of hybrid data packets even further by actuating and detecting the acoustic signal using a battery-free RFID tag.

- Chapter 6 finally concludes the thesis and presents possible future work.

CHAPTER 2

WIRELESS NEAR-FIELD HIGH-Q SENSING RESONATOR FOR DIELECTRIC EVALUATION OF COMPOSITES AND POLYMERS

2.1 Introduction

This chapter introduces a wireless near-field sensing system for evaluating the composite and polymer-based dielectric materials. Composites and polymers are widely used in numerous industries like aerospace, renewable energy, automotive, defense, etc. for making low cost, light weight, and long lasting products.

Composites and polymers have an ever increasing demand, so does the requirement of evaluating techniques for avoiding any potential operational issues. Quality analysis of these materials is critical during manufacturing to prevent higher maintenance and repair costs. These materials are produced using various methods under different environmental conditions, where the output yield and quality can vary significantly. Some of the common manufacturing issues of the composites include surface and subsurface defects such as delamination, voids, cracks, fiber breakage, improper bonding and misalignment, etc. [56]. While polymers show problems like density differences, bonding, permeation, and brittling issues, etc.

There is a growing demand for developing rapid, low cost, non-destructive evaluation (NDE) techniques to identify and quantify these issues in composites and polymers to prevent any future economic and structural losses.

In recent years, the advancement in sensing technology has fueled the development of different probing techniques to evaluate the structural integrity of the target under test. In literature, many novel sensing modalities are available analyzing different aspects of the composite and polymer evaluation from direct contact surface mounted probes to non-contact, non-invasive probes. Some of the common NDE techniques are vibration analysis, microwave imaging, thermography, shearography, X-ray imaging, acoustic emission technique, and ultrasonic scanning [56–60]. Most of these

methods suffer from common limitations such as rigorous data analysis and processing, complex scanning, high power transducers, not real-time or robust, lower defect sensitivity, increased cost and surface mount with hard-wired connections. For example, the acoustic methods require physical contact with the materials by surface mounting of sensors using a low attenuation flexible glue, a large number of sensors are required to cover the complete material area makes it impossible to perform real-time scanning on the manufacturing line [59]. Moreover, the thermography methods are sensitive to spatial and temporal temperature variations leading to unreliable sensitivity and depends on the resolution of the expensive thermal camera for imaging [61–63]. The technique also requires a preparation of the surface before implementation due to hot and cold spot. Microwave imaging are the alternative EM methods for evaluating defects in composite and polymer structures. Single element near-field microwave probes can test the dielectric materials, but the high frequency operation makes the circuitry more complicated and expensive. Design of multi-element near-field array probe is intricate due to element size and coupling effects. Additionally, sensitivity of the direct-wired probes depends on the length of the cable, bending effects of the cable, cable losses and connectors. The Q-factor of these sensors are low due to contact loading leading to dampening effects. Table 2.1 lists some of the common NDE methods for composite and polymers. The comparison shows the fundamental limits and the cost of implementation and operation of these methods. In order to overcome these limitations, a low cost, low frequency, real-time, non-contact, and non-invasive wireless sensing technique is needed. The growth of hand-held wireless devices enables the realization of an economical wireless sensing system.

The surface and subsurface manufacturing defects of the composites and polymers can be detected by monitoring the change in material properties such as the relative permittivity, tensile strength, deflection temperature, etc. The defects in composite lead to a change in effective dielectric constant across the surface of the material. In literature, dielectric characterization of different targets such as solids, liquids, and gases has been well studied using wireless near-field and far-field sensor probes [70–73]. Inductor-Capacitor (LC) based wireless resonant tanks are commonly used dielectric probes in which the inductance or capacitance is perturbed by the target under test

Table 2.1: Comparison of commonly used NDE Methods for composites and polymers

Method	Probe/ Feed Type	Cost (Capital/ Operation)	Fundamental Limitations
Magnetic Flux Leakage [64]	Contact/ Wired	Medium/ Low	Limited to ferromagnetic materials
Eddy Current [65]	Near-Surface/ Wired	Low/ Low	Limited to Conductors
Near-field Microwave [60]	Near-Surface/ Wired	Medium/ Low	High Frequency Circuitry, Element Coupling
Far-filed Microwave [66]	Distance Operation/ High Power	Medium/ Low	High Frequency Circuitry, Heavy Data Processing
Frequency Selective Surfaces [67]	Distance Operation	Medium/ Low	Sensor Embedding in Structure
X-Ray [59]	Distance Operation/ High Power	High/ High	No Good Contrast, Radiation Hazard
C-Scans (Ultrasonic) [68]	Via Couplant/ Wired	Medium/ Low	Poor SNR due to high Attenuation
Ultrasonic Guided Wave [69]	Contact/ Wired	Medium/ Medium	Heavy Data Processing
Thermography [61]	Distance Operation	High/ Very Low	Surface preparation
Wireless Near-field (This Work)	Near-Surface/ Wireless	Low/ Very Low	Limited to dielectrics

leading to shift in the resonance frequency. There is a direct correlation between the sensitivity to the Q-factor of the sensor that warrants high-Q sensor design for improved sensitivity [74].

The goal of this work is to develop a novel wireless LC resonant tank-based imaging sensor for detecting dielectric defects in real-time for composites and polymers. The imaging probe requires to have **high-Q, sub-mm resolution and simultaneous actuation and detection capability in array configuration.**

Two different sensor designs are studied in this work, a single capacitive sensor probe and an array probe. The single probe consists of a parallel plate capacitor with strong fringing fields along the edges and a coupled inductor coil forming an LC resonant tank. The inductor coil also allows wireless magnetic coupling with a secondary pick-up coil for resonance interrogation. The resonant frequency of the sensor probe varies due to the capacitive loading of the fringing fields by the target

under test.

The second approach is the array probe that consists of four independent LC resonant tanks with resonance frequencies closer to each other but at independent resonant frequencies. The resonant peaks have sufficient frequency spacing that prevents peak overlap during target sensing. The four tanks are fabricated side by side in a 1x4-array fashion and this array is interrogated using a single external pick-up coil. The array allows two-dimensional simultaneous scanning of the targets under test.

In this work, the capabilities of the proposed sensors are demonstrated by detecting sub-surface and surface defects along different composites and polymers such as glass fiber reinforced polymer (GFRP), and high density polyethylene (HDPE).

2.2 Theory and Design

2.2.1 Single Element Probe @ 5 MHz

A single capacitive sensor probe is investigated to track changes in the relative permittivity of the target under test. The sensor consists of an LC tank, which has an unshielded parallel capacitor fabricated on a Roger's 4350 board with the dielectric constant of 3.66 and a thickness of 1.52 mm. Fig. 2.1 shows the schematic and the actual developed sensor probe with dimensions in Table 2.2. The strip lines with solder pads are designed to couple the capacitor plates with a commercial inductor coil ($100 \mu H$) to form the LC tank. The strip lines on either side of the Roger's board are separated to avoid an increase in the effective capacitance, but offer additional series inductance. The length and width of the strip lines dictate the additional series inductance. Capacitive loading of the target material changes the effective impedance of the LC tank leading to shift in the resonance frequency.

The parallel plate capacitor is designed to have strong fringing fields along the edges of the capacitor that are used for target monitoring. In order to enhance the fringing field at the probe end, the width of the capacitive sensor is kept more than the width of the strip lines. The fringing fields can be tailored according to the defect types of the target under test.

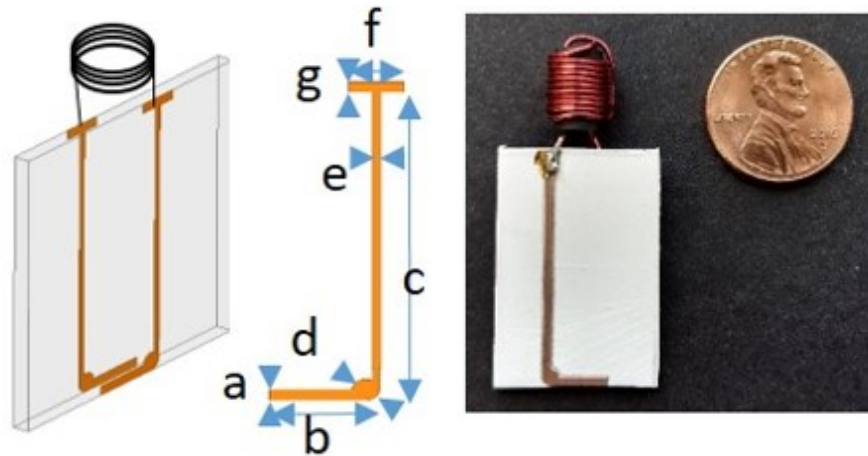


Figure 2.1: Schematic of the LC tank along with the fabricated sensor probe

Table 2.2: Dimensions of the fabricated sensor probe

Parameter	a	b	c	d
Dimensions (mm)	1	8	29	2
Parameter	e	f	g	
Dimensions (mm)	0.6	4	1	

The default response (in Air) of the RF sensing probe is measured using an external pick up coil for interrogation of the LC tank connected to a Vector Networks Analyzer (E5070B). The measurement setup is shown in Fig. 2.2.

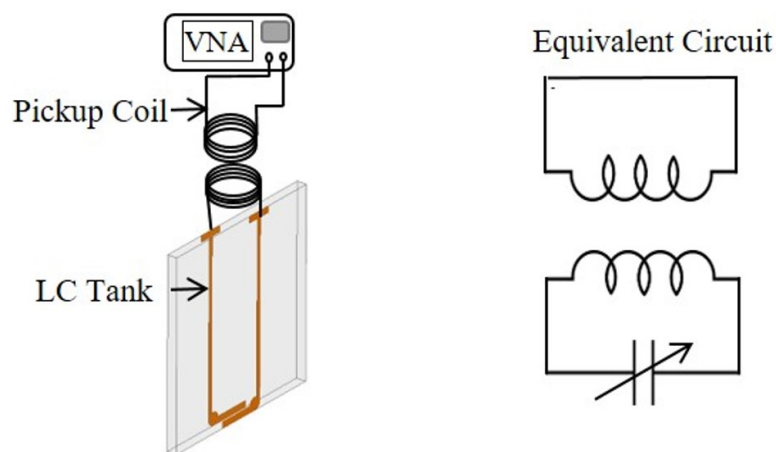


Figure 2.2: Measurement setup for the single probe

The interrogator pick-up coil is designed such that the self-resonance of the inductor is way beyond the resonance frequency of the sensor probe. The pick-up coil is optimally positioned above the sensing resonator probe using a 3D printed cylindrical cap. The coil is wound around the cylindrical cap to interrogate the sensor probe. The reflection coefficient is recorded using the VNA. The measured resonance frequency of the single probe LC tank is at 5.34 MHz. Fig. 2.3 shows the measured S_{11} demonstrating the **high Q-factor** (~ 3800) of the sensor probe.

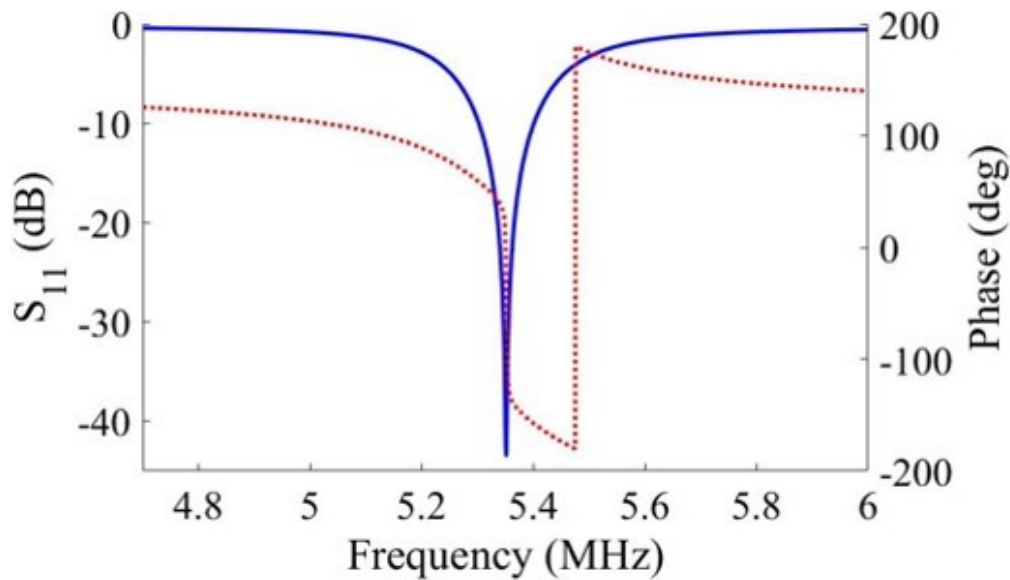


Figure 2.3: Measured S_{11} (magnitude and phase) of the single LC sensor probe

2.3 Measurement and Characterization

2.3.1 Dielectric Reference Measurements

The dielectric reference measurements are performed to demonstrate the change in resonance frequency due to the change in target properties. In this experiment, well-characterized and standard dielectrics were chosen as targets for demonstrating the sensitivity of the sensor probe. Teflon and Plexiglass with the dielectric constant (ϵ_r) of 2.1 and 3.1, respectively, were chosen [75, 76]. The targets were placed in the fringing field region of the LC tank and the resonance frequency was recorded. Equation 2.1 gives the formula for the resonance frequency (f_r) of an LC tank.

$$f_r = \frac{1}{2\pi\sqrt{LC}} \quad (2.1)$$

The resonance frequency is inversely proportional to the total capacitance of the sensor, which is directly proportional to the effective dielectric constant. The **first** set of experiments shows the change in resonance frequency for different dielectric standards in Fig. 2.4. All measurements were taken in triplicates and averaged out, with 1 mm lift-off distance from the dielectric sample. It can be inferred from the graph that, as the dielectric constant increases, the resonance frequency decreases and hence the peak shifts towards the left (lower frequency) as expected.

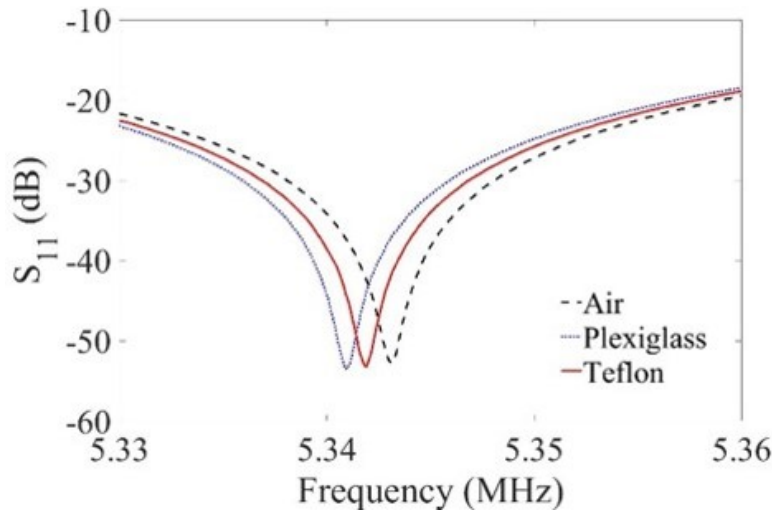


Figure 2.4: Frequency response of the standard dielectric materials (Teflon = 2.1, Plexiglass = 3.1) with known relative permittivity

The single element probe detects less than 5% change in dielectric constant and this was verified by measuring, **second** set of experiment, two samples of high frequency laminates with precisely defined relative permittivity, Rogers's 4003 substrate (thickness = 1.52 mm, dielectric = 3.55) and Rogers's 4350 substrate (thickness = 1.52 mm, dielectric = 3.66). The frequency shift was ~ 0.45 kHz between the two samples, which were measured using VNA with 1 Hz resolution.

The **third** set of experiment was performed on composites and polymers such as polyamide (PA-11), high density polyethylene (HDPE), and glass fiber reinforced polymer (GFRP). The dielectric properties of the targets are 2.8-3.5, 2.3-2.5, and 3.5-3.4, respectively [77–79]. Fig. 2.5 shows the

plot for change in resonance frequency for different composites and polymers. It can be inferred from the plot that, the developed sensor has good sensitivity towards a small change ($\epsilon_r=0.2$) in dielectric constant.

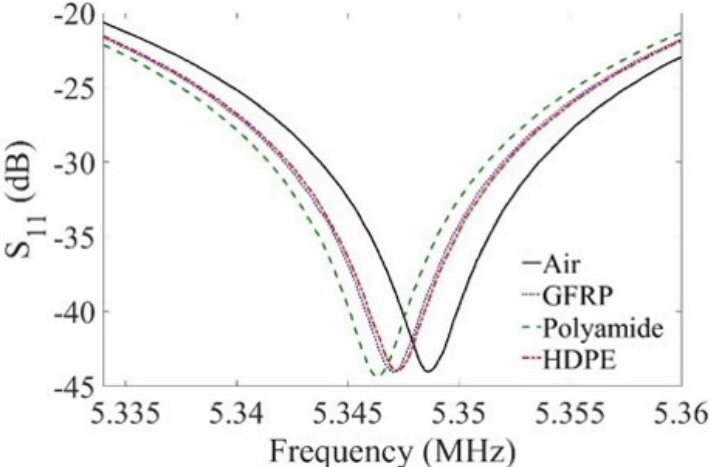


Figure 2.5: Frequency response of the composites and polymers with different dielectric constants

The **fourth** set of experiments were performed to analyze the performance of the sensor probe with conductive targets. Aluminum and Carbon fiber reinforced polymer (CFRP) with a conductivity (σ) of $1e^7 S/m$ and $1000 S/m$, respectively, were chosen as targets. Fig. 2.6 shows the change in resonance frequency for different conductor targets.

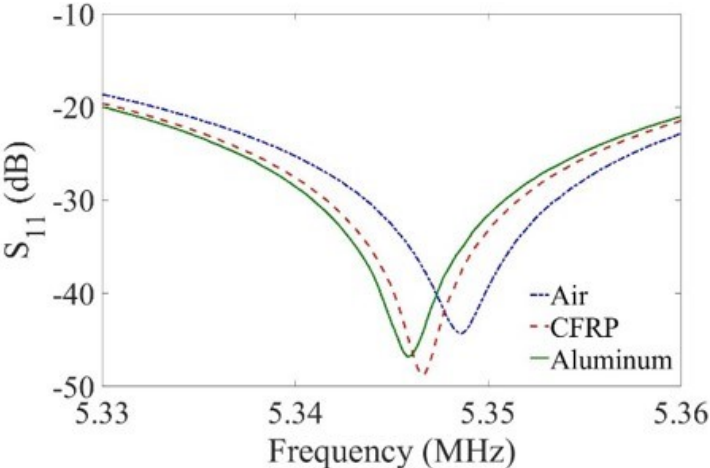


Figure 2.6: Frequency response of the conductive materials with different conductivity

The **fifth** set of experiment shows GFRP with surface defects, which was placed as a target for

testing the sensitivity of the single probe. The surface circular defect had 4 mm radius and a scan across the surface was performed. Each measurement was repeated five times and averaged out. Fig. 2.7 shows the change in resonance frequency and phase for the change in effective dielectric constant due to presence of surface defects on glass fiber reinforced polymer.

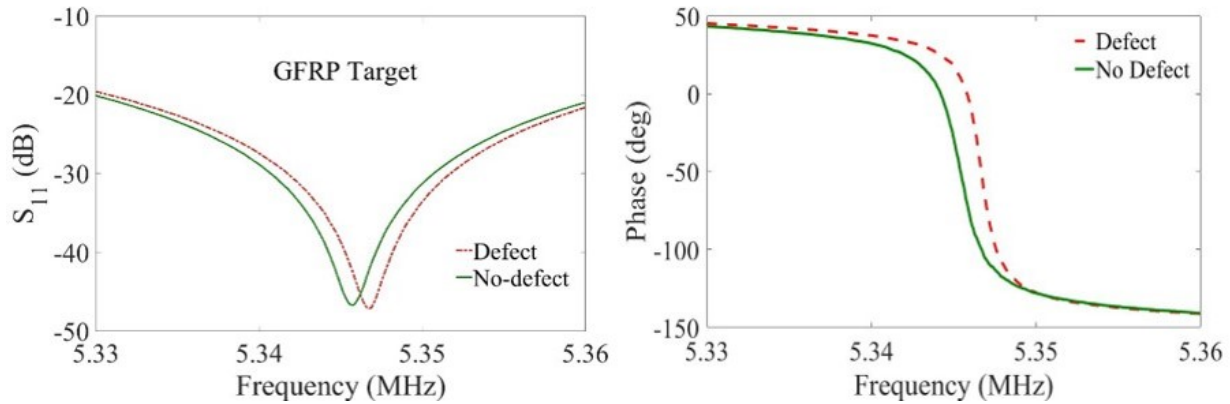


Figure 2.7: Frequency response (magnitude and phase) of GFRP with defect and no defect

The **sixth** set demonstrates the sensitivity of the single probe in detecting subsurface defects. Polyamide with different depths of subsurface defects ranging from 3 to 6 mm was chosen as a target, dimensions of the target are shown in Table 2.3. A horizontal scan was performed across the surface of the target. The effective dielectric constant of the surface decreases with increase in the depth of the defects, which in turn decreases the effective capacitance of the probe thereby increasing the resonance frequency. The measurements were performed in triplicates and the data was averaged out. Fig. 2.8 shows the change in resonance frequency with reference to the resonance frequency of the single probe without any defects for different depths. The resonance frequency change increases with increase in depth as expected. The sensitivity of the probe depends on the strength of the fringing fields and the depth of penetration along the parallel plate capacitor. Based on the sensing application and location of the subsurface defects, the fringing fields of the parallel plate capacitor can be tailored by modifying the design to accommodate greater penetration depth with increased sensitivity.

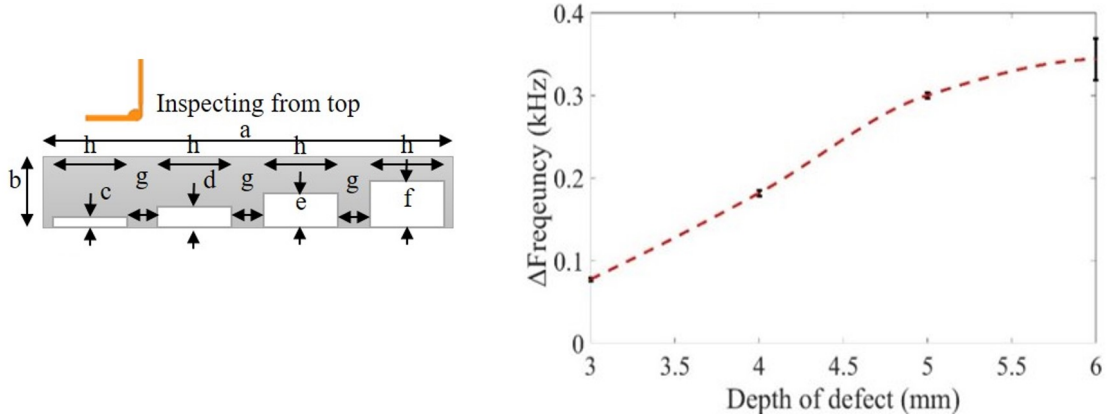


Figure 2.8: Change in resonance frequency for increasing depth of sub-surface defects in polyamide target

Table 2.3: Dimensions of the polyamide sample

Parameter	a	b	c	d	e	f	g	h
Dimensions (mm)	160	8	3	4	5	6	20	24

2.4 Dielectric Imaging

The sensitivity of the single probe is verified using an imaging setup. The probe is mounted on an X-Y raster scanner and the target is placed at a distance of 1 mm from the probe. An RF source operated at the resonance frequency of the single probe (5.34 MHz and 0 dBm input power) is connected to a power splitter which generates two signals, the reference signal and the measurement signal. The measurement signal is fed into the input of the directional coupler and the coupler is connected to the pick-up coil of the probe. The reflected signal (magnitude and phase) from the pick-up coil is fed to one of the input ports of the lock-in amplifier from the directional coupler. The reference signal from the power splitter is fed into the lock-in amplifier for synchronization. The lock-in amplifier generates voltage signals for the difference in reference and reflected signal. The output of the lock-in amplifier is fed into a National Instrument Data Acquisition card (PCIe-6341) which samples and digitizes the data using an imaging software and the output is plotted on a computer. The output is the change in voltage signal as a function of position on the target. A low frequency -3 dB directional coupler was designed for this purpose. The schematic of the imaging

setup is outlined in Fig. 2.9 and the measurement setup is shown in Fig. 2.10.

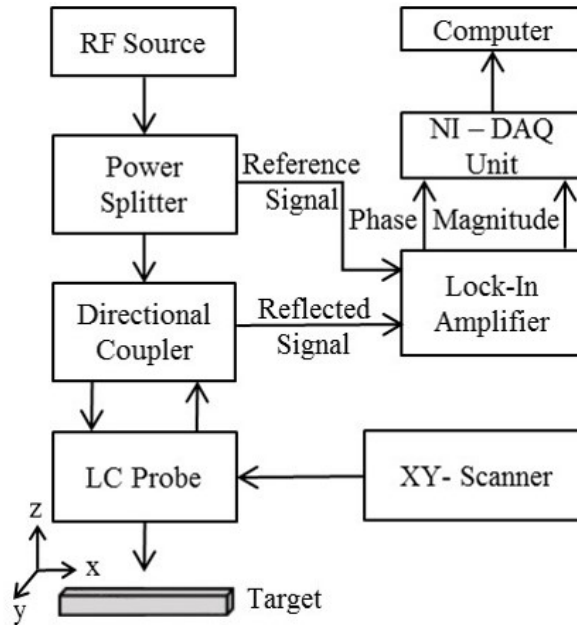


Figure 2.9: Schematic of the dielectric imaging setup

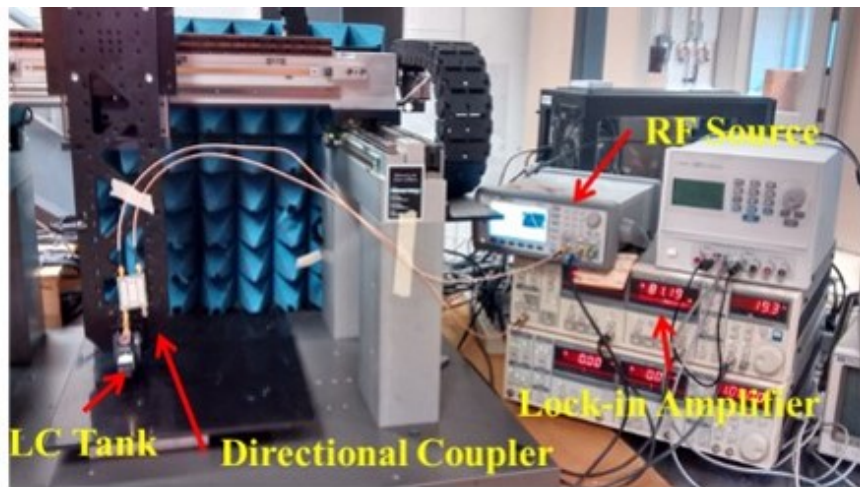


Figure 2.10: Measurement setup for dielectric imaging with the single probe mounted on a X-Y raster scanner

Aluminum was selected as a first demo target material with surface defects. The dimensions of the sample were 180 mm x 220 mm x 3.5 mm and had twelve different sizes of surface defects as shown in Fig. 2.11A and Table 2.4. The defects were also in the shapes of basic geometries such as triangle, circle and squares to analyze the sub-mm resolution of the developed probe. The output

from NI-DAQ was plotted in terms of complex voltages to understand the nature of the defects. Fig. 2.11B shows the changes in output voltage of the reflected signal for different surface defects on aluminum. It can be inferred clearly from Fig. 2.11 that the probe was able to recognize different surface defects with different sizes and shapes.

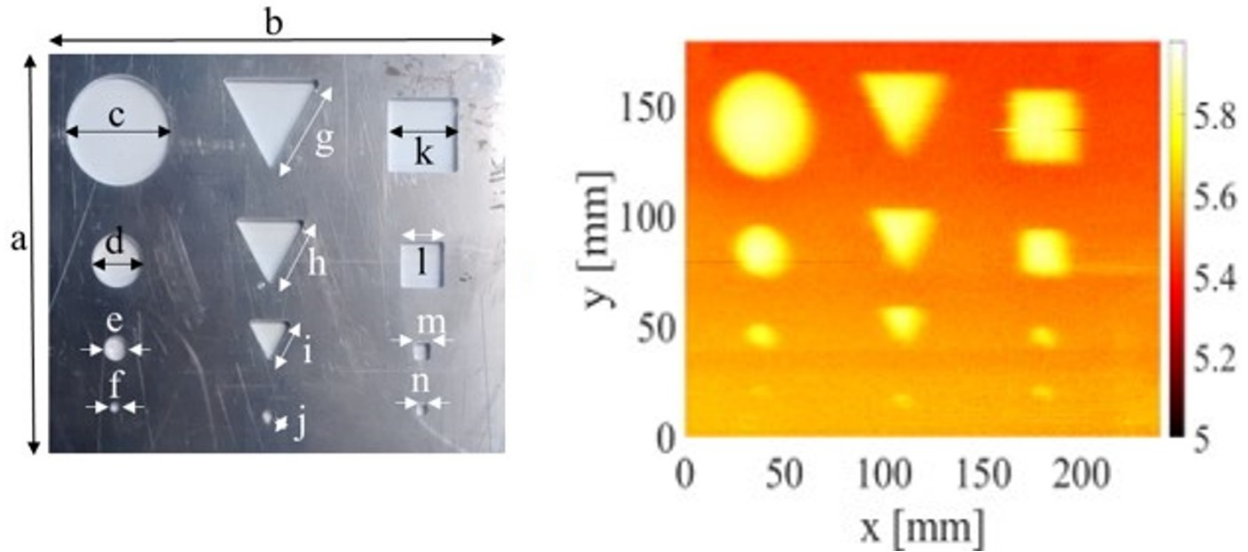


Figure 2.11: (A) Image of the aluminum target with dimensions, (B) Imaging results for profiling of defects using single probe

Table 2.4: Dimensions of the aluminum sample

Parameter	Dimensions (mm)	Parameter	Dimensions (mm)
a	180	h	30
b	220	i	20
c	48	j	5
d	23	k	32
e	10	l	20
f	3	m	8
g	45	n	5

The calibration (aluminum) sample shows promising results and demonstrates the sub-mm resolution capabilities. Dielectric sensor probes shift its resonance according to the effective capacitance and work well with the new custom designed imaging setup. Next step is to check the capabilities of the probe over composite and polymer sample that represents the real world issues.

Three different samples are selected for demonstrating the dielectric imaging capabilities; CFRP, GFRP and HDPE. The imaging results are shown in the sections below.

2.4.1 CFRP Imaging

First, CFRP sample is selected, which is provided by Con-Edison for detecting multiple defects like air gap, contamination, epoxy saturation, mold, and delamination. The CFRP is also wrapped on a steel sample, mimicking the corrosion protection layer and acting as new pressure layer. Fig. 2.12A and Table 2.5 shows the sample image and dimensions. Fig. 2.12B shows the imaging results that clearly detect the embedded defects.

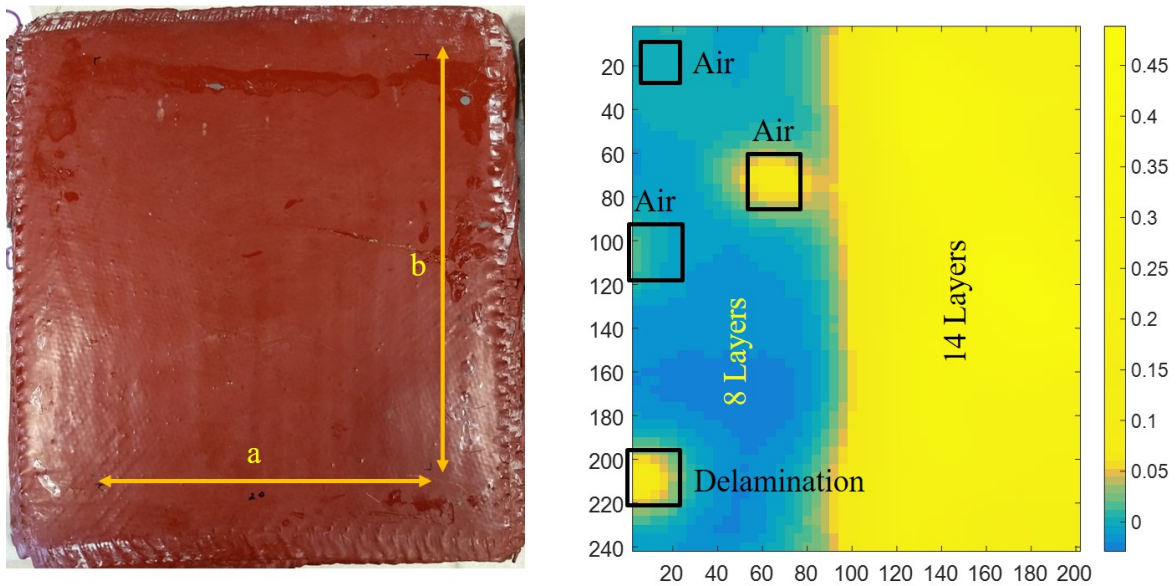


Figure 2.12: (A) Image of the CFRP target, (B) Imaging results for profiling of defects using single probe

Table 2.5: Dimensions of the CFRP sample

Parameter	Dimensions (mm)
a	200
b	240

2.4.2 GFRP Imaging

GFRP was chosen as the second dielectric target for verifying the RF probe capabilities. The dimensions of the target are 128 mm x 126 mm x 3 mm and had multiple defects such as impact damage at the center and fiber breakage (through hole defects) along the four edges of the target as shown in Fig. 2.13A and Table 2.6. Fig. 2.13B shows the changes in imaging results clearly distinguishing the defects.

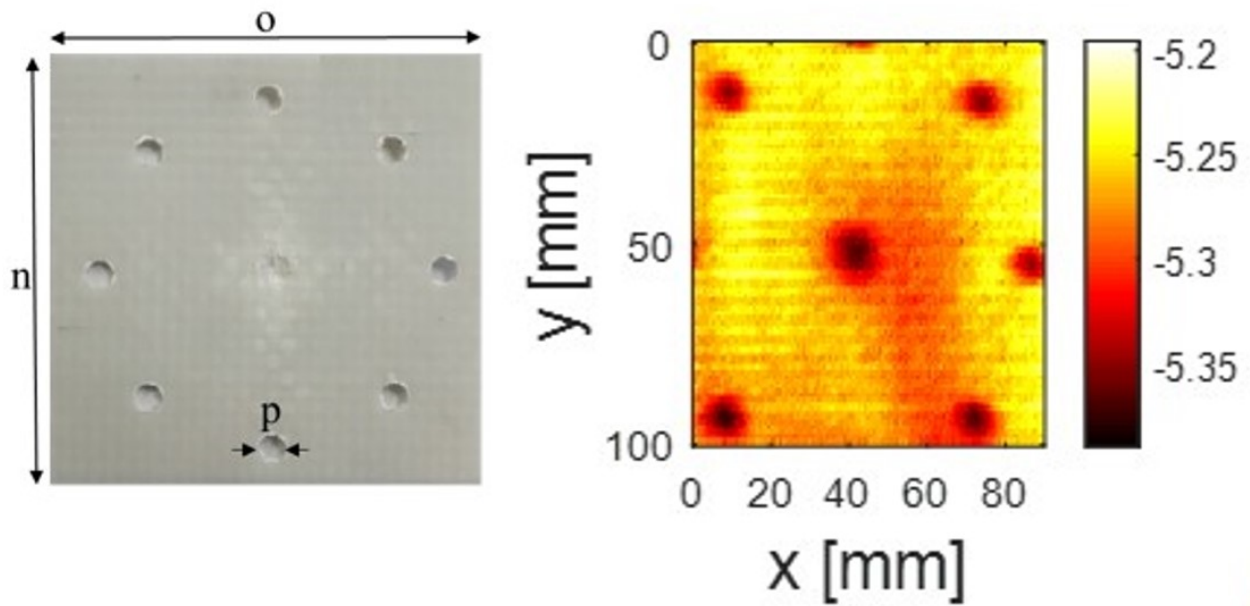


Figure 2.13: (A) Image of the GFRP target, (B) Imaging results for profiling of defects using single probe

Table 2.6: Dimensions of the GFRP sample

Parameter	Dimensions (mm)
n	128
o	126
p	8

2.4.3 Polyethylene Imaging

Polyethylene was chosen as the third target to demonstrate the sensitivity of the probe in detecting subsurface defects. The dimensions of the target are 60 mm x 40 mm x 8 mm and had two different depths of subsurface defects in the shape of a triangle at a depth of 3 mm from the target surface as shown in Fig. 2.14A with Table 2.7 and the imaging verification results are shown in Fig. 2.14B. The results show that the developed probe had stronger fringing fields with higher penetration depth to clearly differentiate the subsurface defects. The penetration depth can be tailored based on the intended application for the detection of deeper subsurface defects.

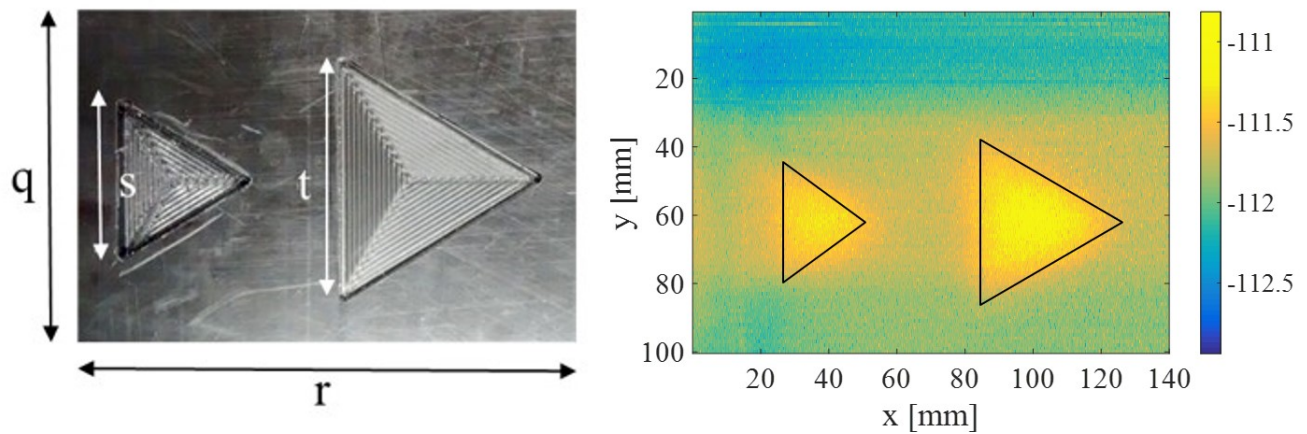


Figure 2.14: (A) Image of the HDPE target, (B) Imaging results for profiling subsurface defects in HDPE target

Table 2.7: Dimensions of the HDPE sample

Parameter	Dimensions(mm)
q	60
r	140
s	25.4
t	38

The imaging verification step demonstrates the capability of the single probe as an RF sensor for detecting surface and sub-surface defects on conductive, composites and polymers materials. The single probe showed very minimal effects when measured using either side of the elongated capacitor while performing the image scans. The orientation of the probe effects the edge response

due to the field distribution along one directions, which can be deconvoluted by signal processing or running multiple scans in different directions. The sensitivity of the probe depends on the strength of the electric-field of the parallel plate capacitor and on the penetration depth of the fringing fields. The developed probe has a sub-mm resolution and can differentiate a small change in dielectric constant ($\Delta\epsilon_r \geq 0.2$), which can be further enhanced by tailoring the fringing fields of the parallel plate capacitor. The spatial resolution is dictated by the scanning step size and the probe size. The probe size depends upon the separation between electrodes (1.5 mm) that can easily detect any crack with size 1 mm or larger. Moreover, the probe is shown to detect sub-surface defects 3 mm from the surface and this could be further improved by tailoring the penetration depth of the fringing fields by further optimizing the probe design. To reduce deflection time and enhance performance, the single probes can be placed in a 2D array format and can be used to simultaneously scan a large surface are while maintaining the resolution. The distance between the sensor probe and the target should be fixed throughout the scan and during successive scans between different samples. A standard set of dielectrics should be used as test targets before the actual measurements to verify the frequency shift dynamics to prevent false positives.

2.5 Array Design and Measurement

A 1x4 array probe was designed with four individual single probe sensing elements on the same substrate. The resonance frequencies of the four probes were spaced apart such that it does not interfere or overlap with each other. The optimization of the resonance frequency was performed by varying the capacitance or inductance of the individual LC tanks. The schematic of the array probe along with the dimensions are shown in Fig. 2.15 and Table 2.8.

A single pick up coil was used to interrogate the array and the measured result of the 1x4 array is shown in Fig. 2.16. The resonance frequencies with high Q factor for the four LC tanks were at 2.41, 3.51, 4.56 and 5.46 MHz, respectively.

GFRP sample was selected to demonstrate the sensitivity of the array probe. A sample of dimensions 128x126 mm with surface defects was placed 1 mm from the fourth element of the

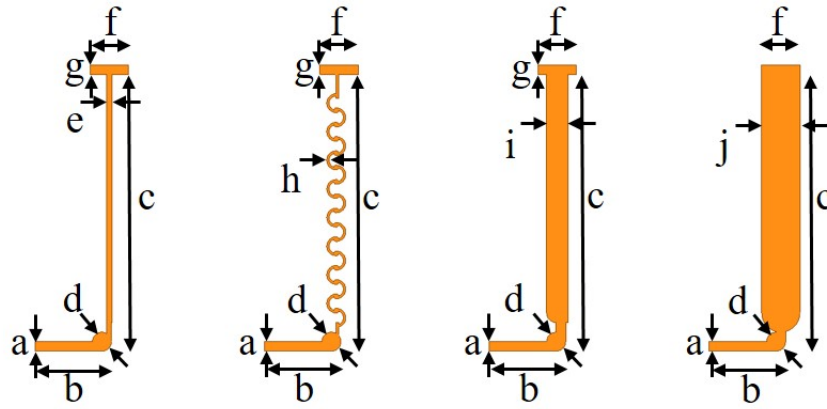


Figure 2.15: Schematic of the designed array probe along with the dimensions

Table 2.8: Dimensions of the array probe

Parameter	Dimensions (mm)	Parameter	Dimensions (mm)	Resonance freq (MHz)
a	1	f	4	2.41
b	8	g	1	3.51
c	29	h	0.25	4.56
d	2	i	2.25	5.46
e	0.6	j	4	

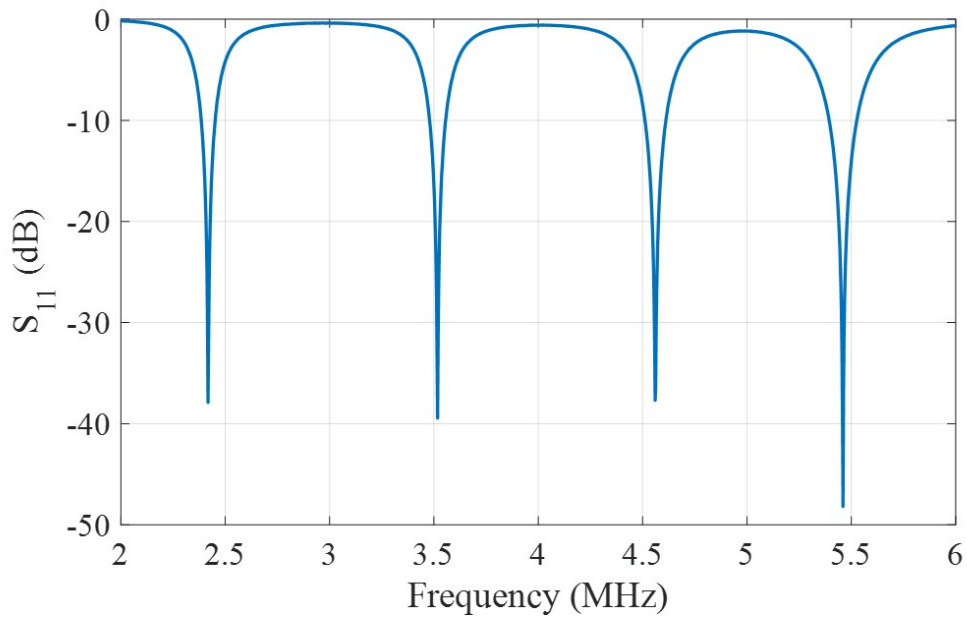


Figure 2.16: Measured frequency response of the 1 x 4 array probe under no loading conditions

array probe to illustrate 2D scanning. Fig. 2.17A shows the measured result of the array probe with the change in resonance frequency for all four frequencies due to the GFRP sample. Since the defect was placed in the near-field region of the fourth element, it can be inferred from the graph that the resonance frequency shifts only for that particular element and remains the same for the first three elements. Fig. 2.17B shows the change in resonance frequency for the fourth array element due to surface defects in GFRP material. The LC array can be further improved by making an $n \times n$ and can be used for simultaneously scanning a large area of the target. The standard dielectric laminates Roger's 4003 and Roger's 4350 are tested that gives a frequency shift of ~ 0.5 kHz.

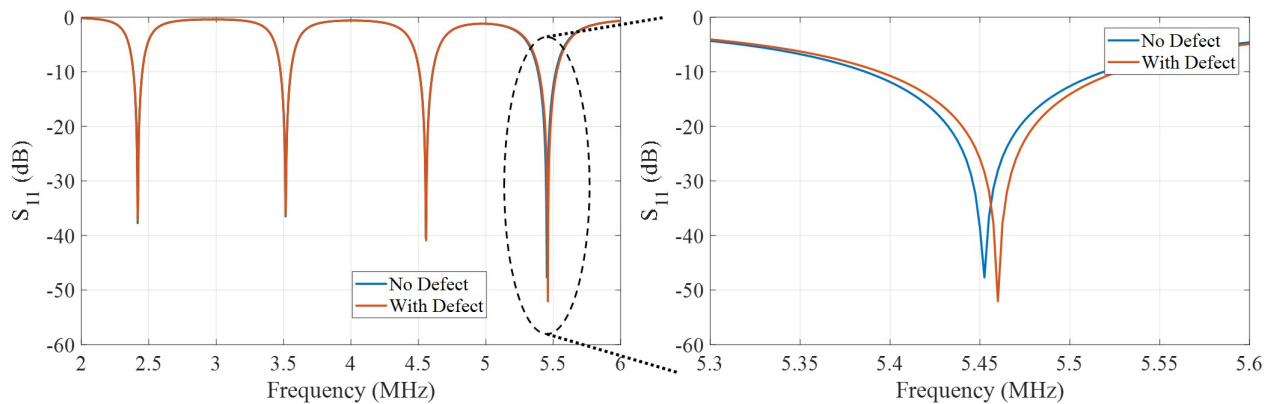


Figure 2.17: Measured results for GFRP with surface defects for (A) All four elements of the array, (B) Focused frequency Shift in fourth element of the array

The array probe allows a second degree of freedom in measuring defects. A major factor that influences the accuracy of the measurements is the isolation between successive frequency peaks in the array. The number of elements in the array are limited by the available frequency band and the isolation factor. The challenge building an efficient array lies in incorporating multiple sensor elements within a short frequency spectrum and at the same time maintaining a high-Q factor for each of them. Another limiting factor for the number of elements is the frequency shift between successive sample scans. Ideally, the shift should not exceed the isolation factor.

2.6 Summary

This work demonstrated a low-cost passive wireless sensor for evaluating structural integrity of composites and polymers. The sensor probe can be easily adapted to scan different kinds of materials for surface and subsurface defects, including material loss, fiber breakage, and impact damage as presented. The electric-field of the capacitive probe can be tailored to detect defects at various depths depending on the application.

The 1 x 4 array probe can be extended to a faster 2D scanning by increasing the number of array elements ($n \times n$). The developed sensor probe can detect less than 5% change in dielectric constant making it a highly sensitive probe for practical applications that can analyze the structural integrity of different targets. The array sensor probe can be readily used in manufacturing lines for quality control applications.

CHAPTER 3

WIRELESS FAR-FIELD HARMONIC RFID COMMUNICATION PLATFORM FOR ENHANCED RANGE

3.1 Introduction

Radio frequency identification (RFID) system is a well established infrastructure used across multiple avenues such as logistics, security, automobiles, health-care, toll tags, animal tracking, quality control, and applications based on internet-of-things (IoT) [80–84]. A typical RFID system consists of RFID tags as markers for tracking and identification, and an interrogator to read the tags [80]. A passive UHF RFID tag consists of an antenna and an application specific integrated chip that can be powered up using the received RF signal. The interrogator transmits the query signal which is received by the tag, the signal powers up the chip which then re-transmits the modulated signal back to the receiver with the identification information [85]. Although the current system is well-established, there exists a number of drawbacks such as self-jamming and multi-path interference that limits realizing the full potential of the RFID system [86, 87].

Typically, a passive UHF RFID system operates in a single frequency band, 902-928 MHz in the United States. The isolation of transmitter and receiver paths is vital to prevent self-jamming of the RF signal. Most RFID readers use either a bistatic or a monostatic antenna configuration to transmit and receive the information. Due to single frequency operation, both configurations suffer from low transmitter-to-receiver isolation. This signal leakage weakens the sensitivity and limits the performance of the RFID system [88]. The low isolation (leakage) limitation of the interrogator increases the phase noise and raises the power spectral density higher than the side bands of the weak reflected signal, increasing the bit-rate error between the RFID tag and the interrogator. Moreover, another limiting factor that reduces the overall system performance is the multi-path interference due to reflections from surrounding structures, as well as interference from other tags operating in the same frequency band. The problem is depicted in Fig.3.1.

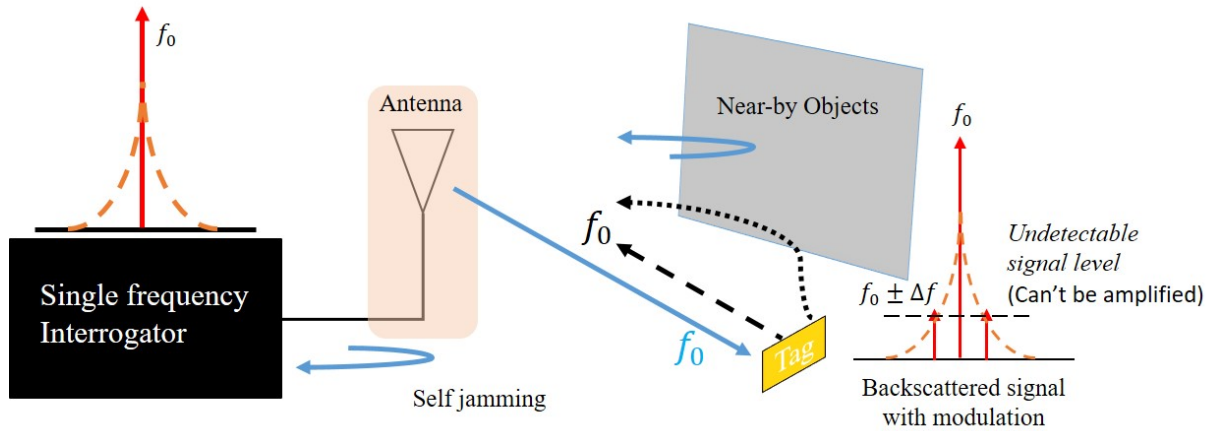


Figure 3.1: Range limiting phase noise issue with conventional RFID system

Over the last decade, a number of techniques have been proposed that cancels self-jamming and limits the multi-path interference. For example, a sample of the transmitted signal with opposite phase is added to the receiver to cancel out the self-interference [89, 90]. Moreover, adaptive self-jamming cancellation algorithms have been proposed that automatically optimize the parameters chosen for the cancelling signal and alter the cancelling signal based on the dynamic changes in the tag environment such as reflections from surrounding objects when the tag is in motion to suppress self-jamming [91, 92]. However, these techniques do not provide a robust, reliable solution to the limitations of the system and hence in recent years, harmonic RFIDs and software defined radio (SDR) based interrogators are proposed as an alternative solution for conventional single frequency RFID systems [86, 93, 94]. The primary idea for using clutter free communication method is to enhance the detection range as shown in Fig.3.2. The communication distance is divided into 3 different regions. Region 1 represents the range of the conventional RFID system where the tag turns on using harvested power and the reflected signal is strong enough to be detected by the interrogator. Region 2 represents where RFID tag turns on using the harvested power due to its low sensitivity but do not able to reflect the strong signal that can be detected by the interrogator due to high phase noise levels. Region 3 represents where the tags do not able to harvest enough received RF power so it would not reflect any signal back. Among these 3 regions, using harmonic communication, the range can be extended up to the end of Region 2, which offers a clutter free

operating mechanism.

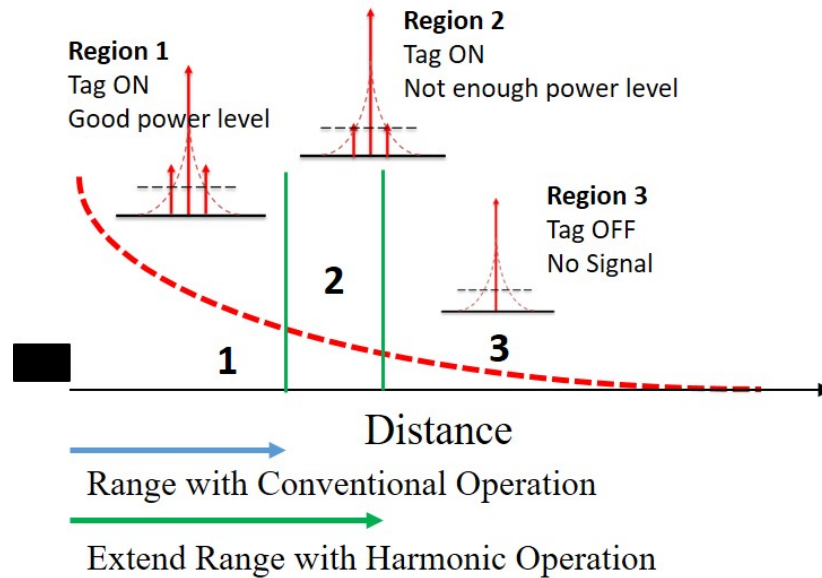


Figure 3.2: Hypothesis for harmonic communication towards range enhancement

A harmonic radar concept is illustrated in Fig.3.3. The harmonic radar illuminates the tag at the fundamental frequency (f_0), and the non-linear elements in the tag generates higher order harmonics (nf_0) and re-radiates it back to the interrogator.

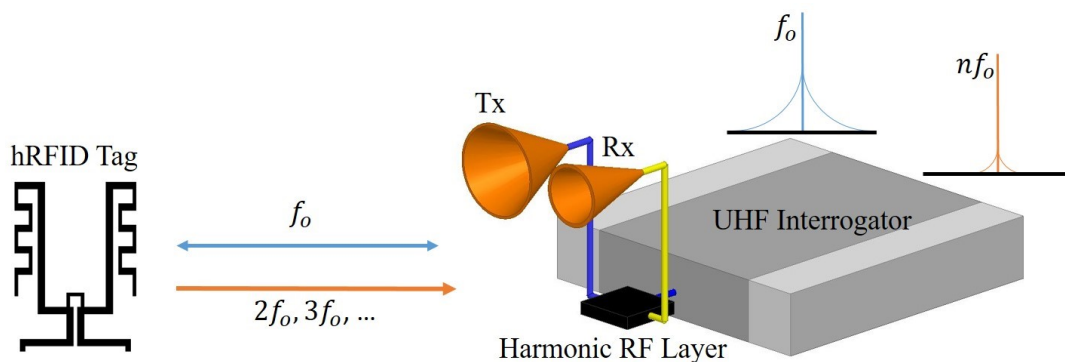


Figure 3.3: The hRFID communication system

In literature, a number of papers have been published on the concept of using harmonic radar for RFID applications. These tags exploit the non-linearity in active components to generate harmonics separating the uplink and the downlink frequency thereby completely eliminating self-jamming. Moreover, these tags do not require a more sophisticated RF isolator to prevent leakage or cross-

talk at the front-end, reducing the system complexity. The tags range from chipless harmonic passive tags (battery-free) to harmonic tags integrated with RFID digital components [86, 95]. The nonlinearity is achieved by using a single or a series of active devices, such as a Schottky or a Varactor diode [96]. In order to adapt the harmonic radar concept with the current RFID technology, two possible options are commonly explored. First option is to redesign both the RFID tag and the interrogator to generate harmonics and read harmonics, respectively. Second option is a cost-effective one to use the current infrastructure to generate and read harmonics from the commercial RFID tags.

The commercially available UHF RFID tags are passive in nature and are constrained by the availability of real-estate for additional sophisticated electronics such as on-board filters to suppress the nonlinearities generated from the diodes and MOSFETs of the RFID chip. The concept of harmonic generation from commercially available UHF RFID tags was explored in [97] and the authors concluded that the current RFID tags can generate and scatter harmonics depending on three parameters. First, the specific tag antenna design, second, the IC sensitivity or the minimum RF power required for the interrogator query signal to activate the chip, and third, the power and bandwidth of the interrogation signal. An RFID test platform for characterizing the nonlinearities generated by the conventional tags is presented in [98]. A method to read the harmonic backscattered information by manipulating the physical layer of the interrogator is presented in [99, 100], where an oscilloscope is used to detect the backscattered RFID signal at the harmonic frequency. Recently, the integration of UHF passive RFID tag with harmonic energy harvesting function is explored, wherein the third harmonic power generated by the RFID ICs is utilized to harvest energy and improve the read range of the tag [101, 102] as well as for activating sensors coupled to the tag [103]. In order to exploit the full potential of the harmonic signals generated by the RFID IC, not just for harvesting or sensing but also as carrier of information, harmonic communication platform using the existing single frequency UHF RFID system is necessary.

In this work, a method to utilize the existing UHF RFID platform for harmonic communication is explored for the first time by designing an interface RF harmonic layer between the commercially

available RFID interrogators and the RFID tags. The advantages of the harmonic system are realized fully in a conventional UHF RFID system by utilizing the proposed architecture without any internal design change to the interrogator as shown in Fig.3.3. A new harmonic hRFID tag antenna design is proposed for efficiently radiating the harmonic signal back to the interrogator. The proposed system utilizes the advantages of harmonics in terms of improved signal to noise ratio, higher clutter rejection, and enhanced read range. An analysis of harmonic communication is also performed demonstrating the relationship between the read range, the RFID IC sensitivity, and the received signal power. The proposed system can be used for interrogating commercially available existing UHF RFID tags or custom antenna-designed hRFID tags. The harmonic solution with increased read range can be easily adapted for any current UHF RFID application.

3.2 Design

The hRFID system shown in Fig.3.3 consists of two main units: A) hRFID Interrogator, and B) hRFID Tag.

3.2.1 Harmonic RFID Interrogator

The hRFID communication platform has significant advantages than the conventional single band RFID system. However, the current RFID infrastructure is built upon the conventional UHF RFID platform and millions of interrogators are in place. Replacing all interrogators with hRFID system is impractical and uneconomical. Hence, a cheaper alternate solution is proposed by using the existing conventional RFID system for harmonic communication by integrating an additional RF front-end to the interrogator for receiving the backscattered tag information at the harmonic frequencies.

The additional RF front-end will act as an intermediate communication layer between the conventional RFID interrogator and the hRFID tag. The harmonic RF layer receives the query signal from the interrogator at the fundamental frequency (f_0) and radiates it using an UHF antenna operating at the fundamental frequency band. The hRFID tags that are present within the field of radiation will receive the query signal and respond back to the interrogator with

fundamental signal is extracted from the circulator's output port before forwarding it to the UHF antenna using a directional coupler (MC ZABDC20-25H-S+) with a 22 dB coupling factor. The Laird's circularly polarized patch antenna with 6 dBi gain is used for radiating the fundamental frequency signal to the tag.

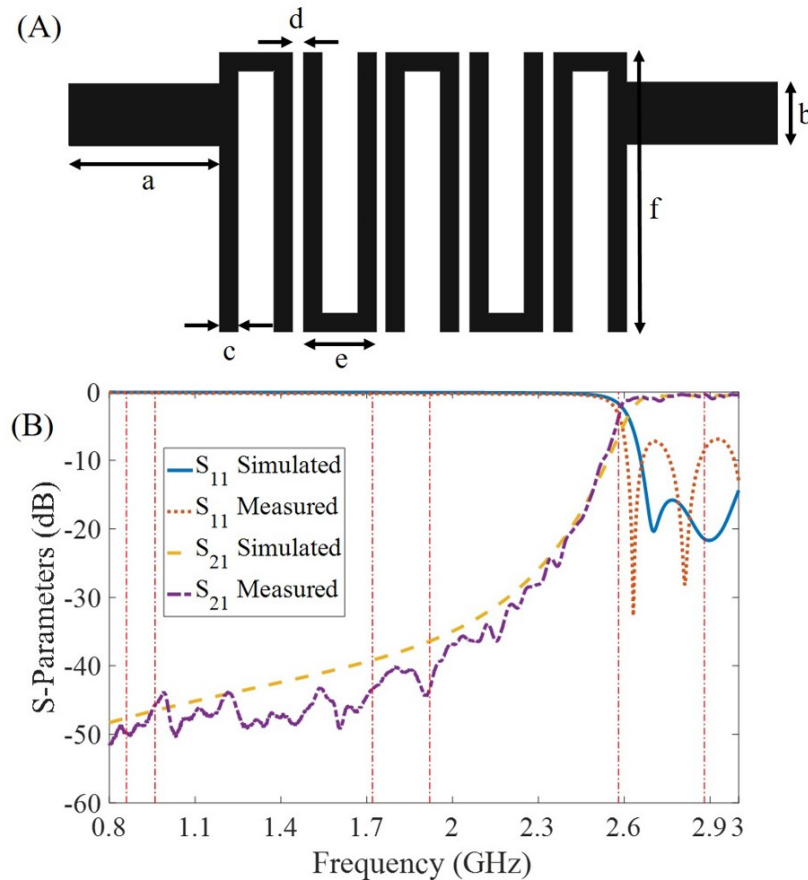


Figure 3.5: Hairpin bandpass filter, F1 (2.6-3.4 GHz): (A) Schematic with dimensions, and (B) Simulated and measured S-parameters

Table 3.1: Dimensions of the Hairpin bandpass filter

Parameter	a	b	c	d	e	f
Dimensions (mm)	8.0	3.32	1.0	0.575	3.92	15.0

The third harmonic reflected signal from the hRFID tag is received using a Vivaldi antenna. The choice of third harmonic signal for reflecting information from the tag is explained in the next section and also in refs [97, 98]. In this work, the harmonic system is designed to query the RFID

tag at the fundamental frequency and read the backreflected information at the third harmonic frequency. Since the Vivaldi antennas are wide band, it is necessary to filter out the fundamental frequency signal and allow only the third harmonic signal to be downconverted in order to extract the information. To achieve this, a hairpin filter in a bandpass configuration is designed and fabricated on Rogers's 4350 substrate (thickness = 1.52 mm, dielectric = 3.66, loss tangent = 0.003) using a standard photolithography process. The schematic of the designed hairpin filter along with its dimensions, simulated, and measured results are shown in Table.3.1 and Fig.3.5.

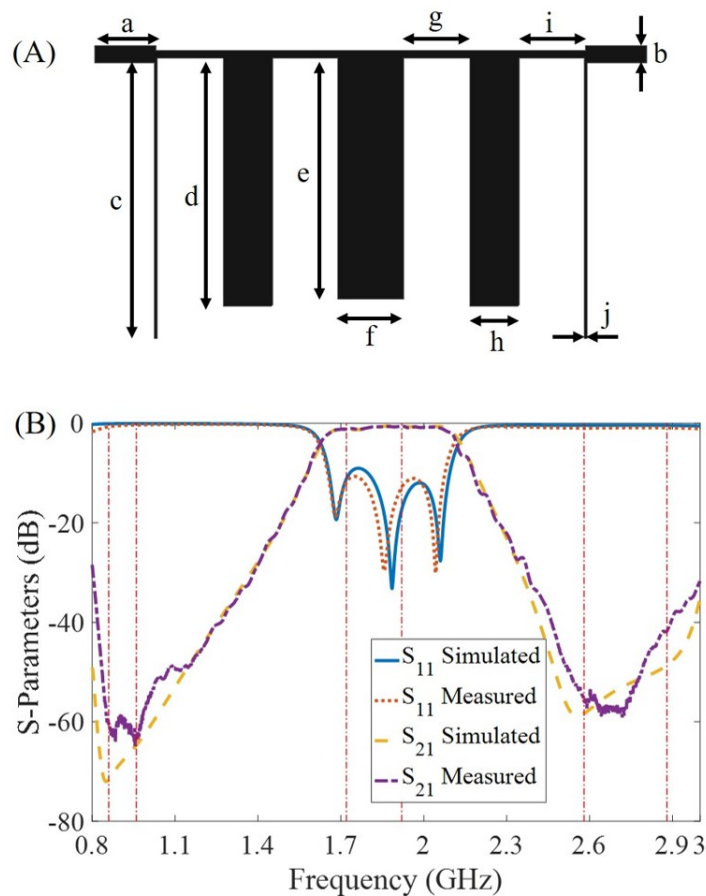


Figure 3.6: Five stage bandpass filter, F2 (1.7-1.9 GHz): (A) Schematic with dimensions, and (B) Simulated and measured S-parameters

Fig.3.5 shows that the designed filter provides a 45dB isolation of the reflected signal from the tag at the fundamental frequency (915 MHz), and allows only the third harmonic frequency (2.745 GHz). The received third harmonic signal is amplified using a Mini-Circuit's LNAs (MC ZX60-

Table 3.2: Dimensions of the five stage bandpass filter

Parameter	a	b	c	d	e
Dimensions (mm)	11.6	3.27	52.36	47.0	45.71
Parameter	f	g	h	i	j
Dimensions (mm)	12.44	12.56	9.30	12.56	0.35

53LNB-S+ and ZX60-43+) with a total gain of 36 dB. To feed the information into the conventional UHF RFID interrogator, the amplified third harmonic frequency signal should be downconverted to the fundamental frequency using an RF mixer. For this purpose, the second harmonic signal at 1.830 GHz is required at the LO port of the mixer. To obtain the second harmonic signal, the reference 915 MHz signal from the output port of the directional coupler is fed into a frequency multiplier (MC FK-3000+) for doubling. The output of the frequency multiplier is amplified using an LNA (MC ZX60-2531MA-S+) with a gain of 34 dB and is fed into a five-stage bandpass filter. The purpose of the filter is to allow just the second harmonic frequency (1.830 GHz) into the mixer. The filter is designed with Roger's 4350 of thickness 1.52 mm and the schematic with dimensions and its frequency response are shown in Fig.3.6.

The second harmonic signal is fed into the LO-port of the RF mixer, and the third harmonic signal reflected from the tag is fed into the RF-port of the RF mixer for down conversion. After down conversion, the output fundamental frequency signal with the RFID information is received at the IF-port of the RF mixer (MC ZX05-42MH-S+). The output of the mixer is fed back into the conventional RFID interrogator through a circulator.

The designed harmonic RF layer allows uplink at the fundamental frequency and downlink at the third harmonic frequency. The RF layer operates within the bounds of the conventional RFID system at the same time providing the advantages of a harmonic platform.

3.2.2 Harmonic RFID Tag

The conventional single band RFID tags designed by various companies (for example, IMS, Alien, Impinj, etc) are commercially available. The fundamental architecture of a tag consists of an UHF

antenna and an RFID IC. The IC performs logical controls and responds to specific query signals from the interrogator. The IC uses a MOSFET for modulating the ID information on a backscattered RF signal by switching between "on" and "off" states. The digital part of the IC requires a DC power for operation and is generated using an RF-to-DC converter with rectifying diodes in a charge pump configuration [86]. The internal circuitry of the IC with non-linear components including diodes and MOSFETs collectively generates the third harmonic signal. The details of the third harmonic generation from commercial RFID tags are available in the literature [97,98]. The conventional off-the-shelf RFID tags (COTS-RT) are designed to operate in a single frequency band (902-928 MHz), and do not radiate the internally generated third harmonic signals efficiently. This section shows the design of an RFID tag antenna for efficient third harmonic radiation. The radiated third harmonic signal has very low signal strength, but for the case of harmonics, the noise level is also extremely low, which in turn increases the SNR of the received signal.

3.2.2.1 RFID IC

The RFID chip chosen for integration with the designed hRFID tag antenna is the Higgs-3 from Alien Technology [104]. According to the data sheet, the chip has a -15 dBm read sensitivity and is capable of operating in the frequency band of 860-960 MHz. Due to the requirement of a smaller footprint and low sensitivity level, RF filters are not integrated as a part of any commercially available RFID chips. This leads to an internal generation of harmonics that are not suppressed and these contains the modulated identification information as well. This third harmonic signal can be radiated back to the interrogator using a dual band antenna design. The Alien's Higgs-3 IC has a characteristic input impedance of $39.5-j60 \Omega$ and $15+j0 \Omega$ at fundamental (915 MHz) and third harmonic frequency (2745 MHz), respectively.

3.2.2.2 RFID Antenna

To efficiently radiate the third harmonic signal, a new antenna design is required that operates in two different frequency bands, the fundamental band from 902-928 MHz, and the third harmonic

band from 2706-2784 MHz. Commercially available RFID tags commonly use a single meandered dipole configuration for an antenna operating at a single UHF band. Whereas, the hRFID antenna consists of two antennas operating at the fundamental and the third harmonic frequency bands.

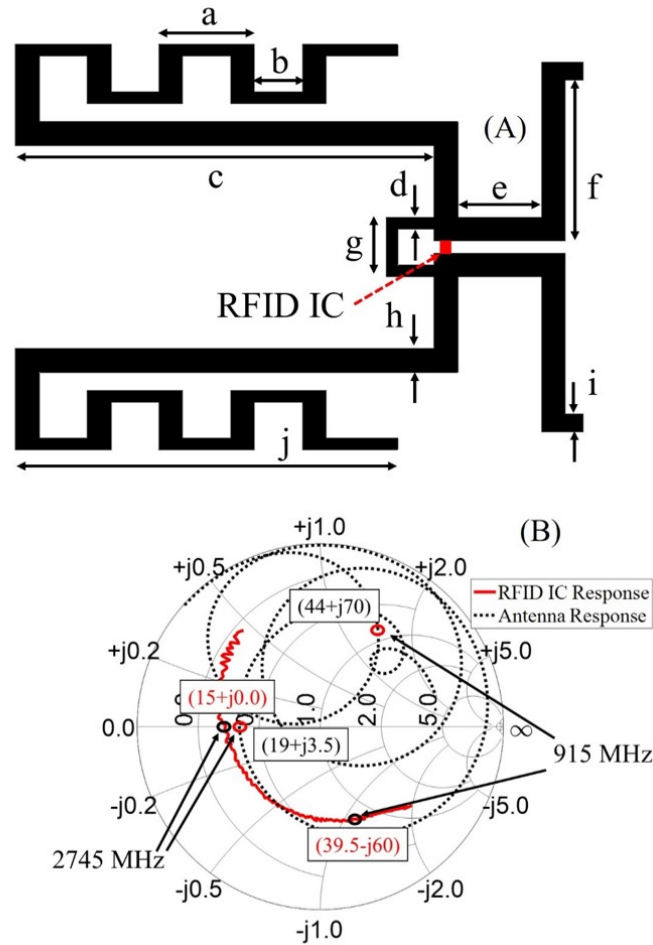


Figure 3.7: (A) Schematic of the designed hRFID antenna along with its dimensions, and (B) Measured frequency response of RFID IC and hRFID antenna with conjugate matching points

Table 3.3: Dimensions of the hRFID antenna

Parameter	a	b	c	d	e
Dimensions (mm)	8.0	4.0	35.0	1.0	7.0
Parameter	f	g	h	i	j
Dimensions (mm)	13.5	5.0	2.0	1.5	32.0

ANSYS HFSS[®] (2019, ANSYS, Inc., Canonsburg, PA, USA) were used to design the dual

band antenna. The schematic of the designed antenna along with its dimensions is shown in Fig.3.7A. The antenna is designed on Roger’s 4350 substrate and fabricated using conventional photolithography. The measured frequency response of the designed hRFID antenna with conjugate matching is shown in Fig.3.7B.

3.3 Results

For the demonstration of a harmonic RFID platform using the conventional UHF system, three sets of experiments are performed.

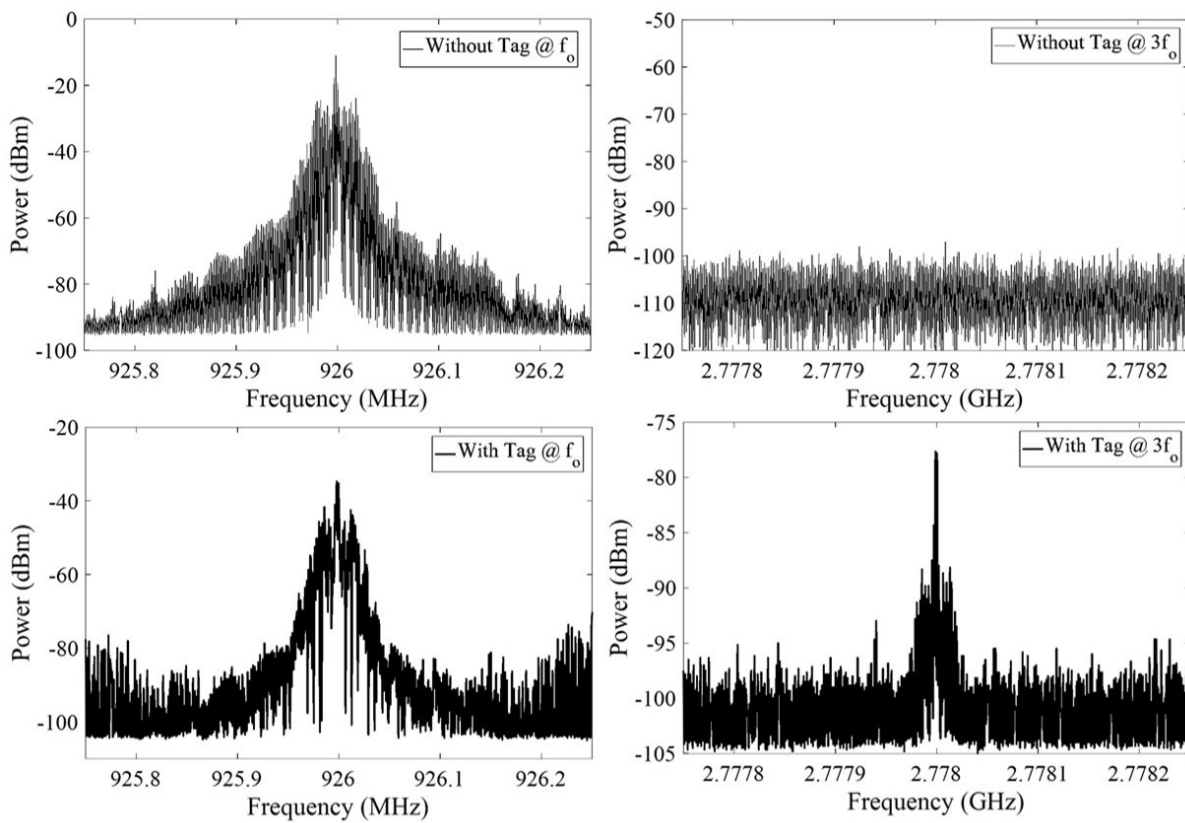


Figure 3.8: Measured backscattered signal visualized using a spectrum analyzer, with a transmitted power of +8 dBm and a read range of 0.35 m: Received signal at the fundamental and the third harmonic frequency with and without the RFID tag in the interrogator’s field of view

First set of experiments demonstrates the third harmonic generation by conventional RFID tag (on Higgs-3 chip), down conversion and detection. The second set demonstrates the efficient harmonic radiation from the designed hRFID tag. Third set of experiments demonstrates the

improved read range of the designed hRFID tag using harmonic communication. The hRFID interrogator platform explained in the previous section is assembled, and the return power from the RFID tag at the fundamental and third harmonic frequencies are measured via a circulator coupled to a patch antenna and a Vivaldi antenna, respectively. The reflected signal is acquired using a spectrum analyzer (HP8562A). The RFID interrogator is configured to transmit +8 dBm at a single UHF frequency (926 MHz) for analysis purposes. The spectrum analyzer is set at the fundamental (926 MHz) and at the harmonic (2778 MHz) frequencies with a span of 500 kHz and a bandwidth of 10 kHz. Fig.3.8 row 1 shows the received RF signal without any RFID tag. It can be inferred from the figure that at the fundamental frequency, the leaked interrogator signal with query information is received, showing the isolation limitation of any single band communication system. The leakage increases the noise level causing self-jamming of the fundamental reflected signal. Whereas, at the harmonic frequency, the noise level is dictated by the thermal factors and is below -100 dBm.

Next, the conventional RFID tag is placed at a distance of 0.35 m from the interrogating antennas, and the reflected signal is received with the same setup. Fig.3.8 row 2 shows the received backscattered signal at the fundamental and at the harmonic frequencies. The increase in power of the side bands at the fundamental frequency is clearly visible representing the RFID tag information in the frequency domain. The RFID tag also reflects back the information at the third harmonic with a lower strength in comparison to the fundamental frequency but with a higher SNR. The RFID modified interrogator with the harmonic RF layer receives the third harmonic signal and down converts it. The RF mixer requires a second harmonic RF signal for reference, which is generated by doubling the interrogator's fundamental frequency signal, shown in Fig.3.9 row 1. The mixing of the amplified third harmonic and reference signal gives an output at the fundamental frequency, which is the downconverted signal with information on the sidebands detected by the interrogator, as shown in Fig.3.9 row 2.

The conventional RFID tag is replaced with the designed hRFID tag. The designed hRFID tag generates the harmonic signal 7 dB higher than the conventional RFID tag with the same input

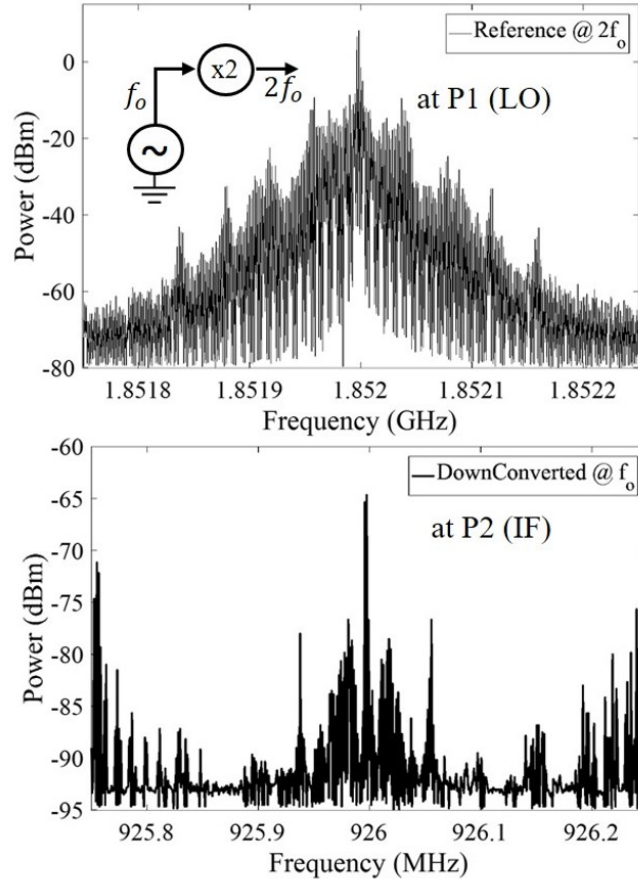


Figure 3.9: Measured backscattered signal visualized using a spectrum analyzer, with a transmitted power of +8 dBm and a read range of 0.35 m: Reference signal at the second harmonic frequency generated using a frequency doubler and the down converted signal at the fundamental frequency after mixing

power and interrogation distance as shown in Fig.3.10.

The designed hRFID tag is tested and a comparison between the fundamental and the harmonic communication for a range of up to 6.5 m is demonstrated. The interrogator is set to transmit +30 dBm of power using a 6 dBi gain patch antenna. The designed hRFID tag receives the query signal and reflects back the information at fundamental as well as at the harmonic frequency bands. The fundamental received signal measured using the conventional setup and the harmonic signal measured using the modified receiver are shown in Fig.3.11. The fundamental signal is probed using an Impinj interrogator without using the harmonic setup. The downconverted harmonic signal is the mixer's output at the fundamental frequency, generated from the received third harmonic

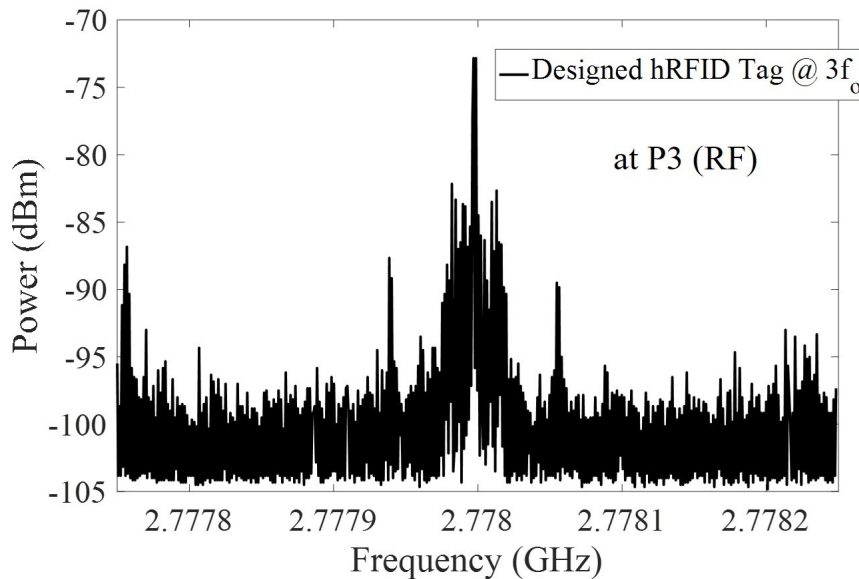


Figure 3.10: Received third harmonic signal from the designed hRFID tag.

signal. The interrogator's detection limit using the conventional RFID communication is at ~ 5 m, whereas using the harmonic communication is at ~ 6 m. The RFID chip stops responding to the query signal at a certain distance (~ 6.5 m) due to the limited IC sensitivity (-15 dBm) and it also poses the limit on the tag detection distance. As the read range approaches 5.5 m for operating the tag in the fundamental frequency, the received signal falls below the noise level due to self-leakage as well as interference and hence the tag is not detected by the interrogator.

The designed harmonic interrogator is tested with multiple (two) hRFID tags. They have different antenna designs, matched at both fundamental and third harmonic frequency bands. The Impinj interrogator's average read rate (total detected tags per sec) for a single tag is in the range of 60-65 and it changed to 71-75 when multiple tags are present in the field of view.

3.4 RF Analysis of Harmonic Communication

The harmonic communication platform is superior to the conventional UHF system due to the capability of eliminating self-jamming and limiting multipath interference. This improvement is due to the lower reference noise level at the harmonic frequency in comparison with the fundamental frequency. In a single frequency band operation, the power leakage from the RF coupler or the

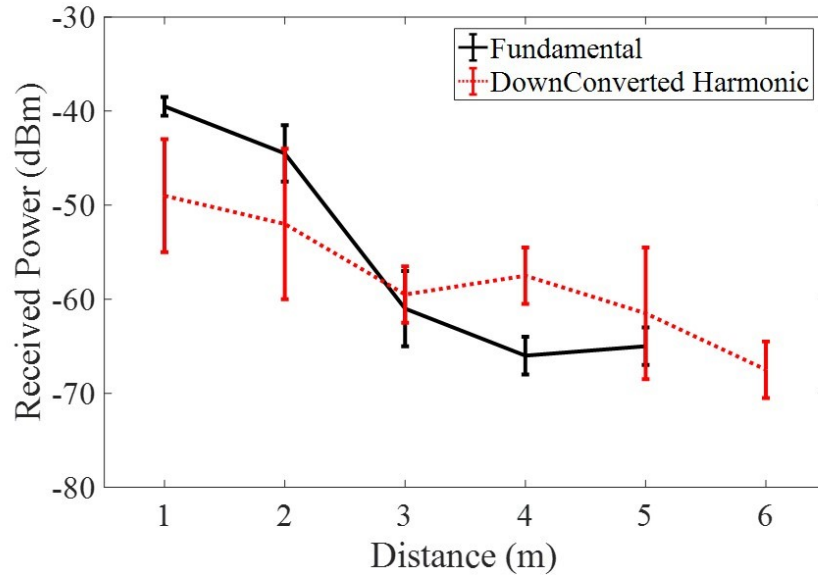


Figure 3.11: Received backscattered power at the interrogator, with transmitted EIRP of 36 dBm, from the designed hRFID tag for both the fundamental frequency and the harmonic frequency operation.

circulator increases the noise level significantly. In literature, the noise level for a conventional RFID system is reported anywhere between -80 dBm to -60 dBm, with varying bandwidth and data rates [105]. Whereas, the noise level at harmonic frequency is dictated by just the thermal factors and is observed to be below -100 dBm, as observed in Fig.3.7A. A system analysis study for harmonic RFID communication with -70 dBm and -100 dBm noise levels at the fundamental and harmonic frequencies, respectively, is presented. The study is primarily focused on the read range of the passive RFID systems. Two different factors are considered in estimating the maximum operating range of an RFID tag: 1) Backscattering efficiency and 2) the IC sensitivity.

The FCC allows to transmit a maximum of 4 W (+36 dBm) EIRP at the fundamental frequency in the ISM band. The received power at the tag located at a distance from 0 to 100 m spacing from the interrogator, and the backscattered signal strength at the interrogator can be calculated using Friis's transmission equation. The modified Friis's transmission is presented in Eq.3.1, which can calculate the maximum possible read range for a passive RFID tag operating with a single frequency or with a harmonic frequency for both the uplink and downlink communication.

$$\arg \min_d [NF - (P_{Tx} + G_{Rdr}^{fo} + G_{Rdr}^{nfo} + G_{Tag}^{fo} + G_{Tag}^{nfo} + 20\log_{10}(c/4\pi df_{TxRdr}) - \eta + 20\log_{10}(c/4\pi df_{TxTag}))] \quad (3.1)$$

where, d is the maximum distance between the interrogator and the tag (read range) that needs to be estimated. P_{Tx} is the transmitted power by the interrogator at the fundamental frequency, G_{Rdr}^{fo} is the gain of the interrogator's transmitting antenna, G_{Rdr}^{nfo} is the gain of the interrogator's receiving antenna, f_{TxRdr} is the frequency of the transmitting signal by interrogator, f_{TxTag} is the frequency of reflected signal by tag, G_{Tag}^{fo} is the gain of the tag's receiver antenna, G_{Tag}^{nfo} is the gain of the tag's transmitter antenna, c is the speed of light, η is the backscattering efficiency or losses due to modulation and reflection, NF is the noise level at the receiving frequency.

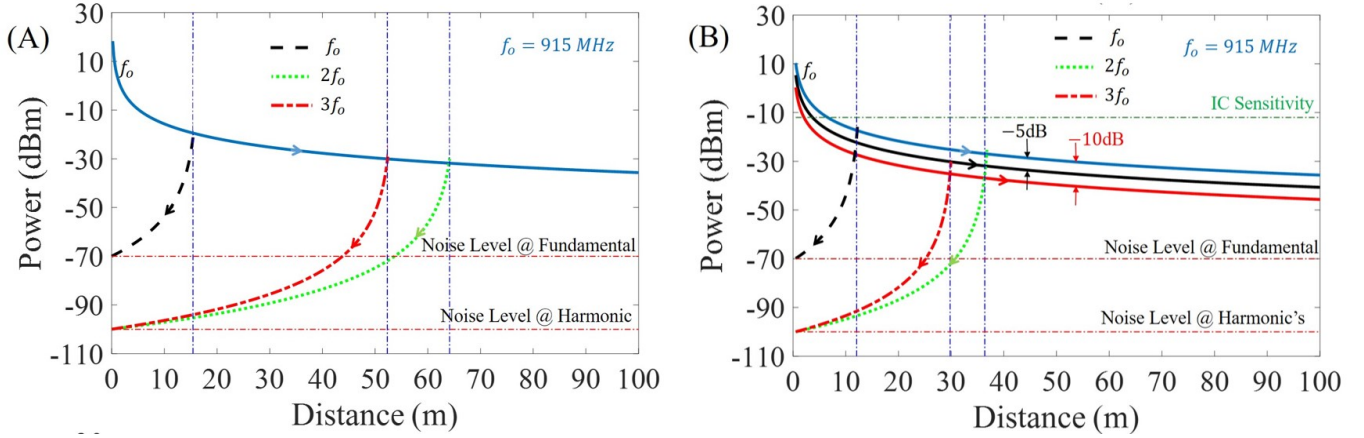


Figure 3.12: Power budget analysis of backscattering based communication system: (A) Detection range using fundamental and harmonic bands with no tag losses, and (B) Detection range using fundamental and harmonic bands with 5 and 10 dB losses, respectively.

Eq.3.1 is visualized in Fig.3.12 with +30 dBm P_{Tx} , 6 dBi G_{Rdr}^{fo} and G_{Rdr}^{nfo} , 0 dBi G_{Tag}^{fo} and G_{Tag}^{nfo} , f_o (f_{TxRdr}), and reflection (f_{TxTag}) at three different frequencies f_o , $2f_o$, and $3f_o$. NF for receiving at f_o is -70 dBm, and for receiving at $2f_o$ and $3f_o$ is -100 dBm. Fig.3.12A shows the maximum possible communication distance of 15.4m, 64.12m and 52.3m for the fundamental, second harmonic, and third harmonic frequencies, respectively, without any RFID tag losses ($\eta=0$). With the tag losses (η) of -5 dB [106] at fundamental and -10 dB [107] at both harmonic frequencies

gives a maximum communication distance of 11.4 m, 35.6 m, and 29.0 m for the fundamental, second harmonic and third harmonic frequencies, respectively, as shown in Fig.3.12B.

The study mentioned above assumes that the tag can be activated at any received power, but the RFID tags have a minimum power requirement that is defined by the IC sensitivity. The IC sensitivity plays an important role in determining the maximum communication distance. The commonly used RFID IC's can be activated with -12 to -15 dBm received power. Fig.3.13 shows that a minimum activation power (-12 dBm) can be received up to a distance of 6.5 m with above-mentioned transmitter and receiver parameters. The backscattered signal from 6.5 m with a lossy tag maintains the power level above the noise level at all receiving frequency configurations. The minimum IC sensitivity limit, for which the received signal stays above the noise level, can also be back-calculated for both the fundamental and harmonic frequencies using Eq.3.1. For a fundamental frequency of 915 MHz, -17 dBm is the calculated limit for IC sensitivity. Using the calculated limit, the maximum read range of the tag is estimated to be 11.6 m. The IC sensitivity limit defines the maximum read range for the respective frequency of operation. If the IC sensitivity goes below the defined limit, the read range will not increase further because the reflected signal will be below the noise level at the receiver end. For receiving at the second (1.830 GHz) or the third (2.745 GHz) harmonic frequency, the maximum read range can be further increased due to a lower noise level. For the second and third harmonic frequencies with a fixed tag loss of 10 dB, the maximum read range is 36 m with an IC sensitivity of -27 dBm, and 29 m with IC sensitivity of -25 dBm, respectively.

The RF analysis of the harmonic communication shows a path to achieve higher SNR with improved clutter rejection, and increased read range. The study reflects the importance of the choice of an RFID IC, and the parameters of the tag in terms of sensitivity, power loss, and noise level with their effects on the read range.

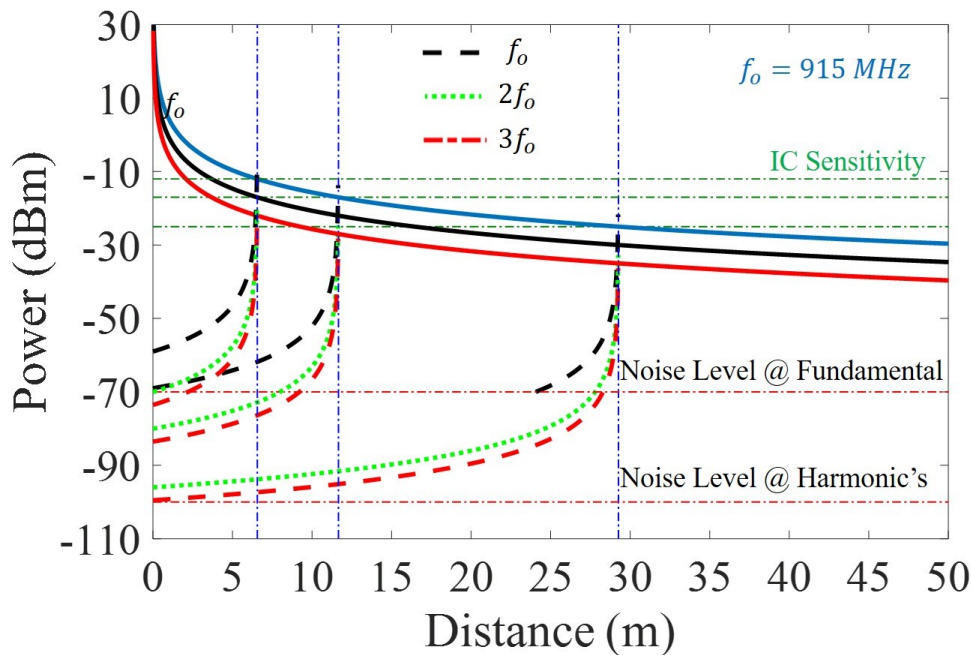


Figure 3.13: Effects of the IC sensitivity on the RFID read range with fundamental and harmonic communication.

3.5 Discussion, Challenges and Limitations

The designed hRFID platform performs better than the conventional RFID system as demonstrated in the previous sections. The key improvement of the hRFID system is the 30 dB reduction in noise level achieved by using the harmonic frequency for communication. Furthermore, the designed harmonic RF front-end for the interrogator can be miniaturized for an easy plug-in that can be directly plugged into the current RFID interrogators for realizing the hRFID platform making it an economical solution.

The harmonic generation efficiency of the RFID ICs changes with different manufacturers, which can be further studied. The harmonic radiation from the passive RFID tag comply with the FCC regulations, as harmonics are considered as spurious signals and allowed if it stays below a certain power level (hRFID radiates in the order of 10^{-11} W) [108]. The harmonic communication overcomes the bottleneck of a conventional RFID with lower noise level that allows an opportunity for further fine tuning the IC sensitivity. The demonstrated harmonic communication platform

using the conventional UHF RFID infrastructure shows the advantages of self-jamming cancellation leading to a higher SNR as well as the availability of three times the bandwidth for communication (2706-2784 MHz). In order to fully realize the potential of increased bandwidth, a change in RFID protocol is required that allows the RFID tags to use wider channels to transmit the information. Overall, the proposed platform is beneficial for any RFID applications that requires improved read range, especially in a cluttered environment.

3.6 Summary

In this work, a hRFID platform is demonstrated using a conventional UHF RFID system for transmitting the information using the inherently generated third harmonic from the RFID IC. An RF harmonic interface layer between the conventional RFID interrogator and the RFID tag is designed. This layer is used as a plug in to any conventional UHF interrogator to transmit the query signal at the fundamental frequency and receive the backscattered information at the third harmonic frequency. Harmonic communication is established using a conventional RFID tag that generates spurious harmonic signals. Moreover, the third harmonic radiation efficiency is increased by designing a new harmonic tag antenna coupled to a conventional RFID IC. An increased read range is achieved along with the elimination of self-jamming and limiting of multi-path interference without any internal design changes to the conventional interrogator. A harmonic analysis is performed showing the relationship between the RFID IC's sensitivity, tag losses, noise level of the interrogator, and the read range. The demonstrated system is best suited for any RFID applications that require increased data rate with improved read range.

CHAPTER 4

PASSIVE SENSOR INTEGRATION WITH ADC-FREE RFID TAG FOR ULTRA-LOW POWER OPERATION

4.1 Introduction

A low power long-range communication system is desired in rapidly modernizing society as it has a huge impact on human safety and economy in multiple sectors such as civil, environment, transportation, etc. [9, 10]. Real-time sensing of different parameters of any object provides timely feedback that ensures enhancing predictive maintenance strategies to minimize human interaction and promote safety and reliability. To make any system intelligent, a number of sensors are required to provide continuous and detailed information on the nature of the system starting from an autonomous vehicle to structural health monitoring [18, 109]. Moreover, the cluster of sensors should be efficient and be able to communicate the sensing information with each other or to the controller in order to perform a quick and accurate corrective action. Conventional wired communication approach towards collecting sensor data from a large number of nodes is neither compatible nor economical and hence a practical wireless approach such as Internet-of-Things (IoT) based platforms are preferred [110]. IoT has revolutionized the world by converting many applications into a "Smart" operation with integrated sensors and devices. Applying IoT to create a "Smart" monitoring system by enabling real-time and reliable wireless data communication among the cluster of sensor nodes enhances the visibility [42]. One of the recent challenges is to develop a low-cost, battery-free, long-range, and real-time IoT sensing system. The impact of the system will benefit areas such as structural health monitoring (SHM).

An example application of pipelines is selected for making the case for battery-free wireless sensor tags and demonstrating the working prototype. Pipelines are the safest and economically viable arterial networks for transporting natural gases and oils across the globe. The pipeline network expands at a faster rate due to the projected growth in population and increased rate of

urbanization, creating a demand of natural gas for domestic and industrial use [111]. The natural gases are gathered, transported, and distributed at various pressure levels via metals, composites, and plastic pipelines. Any material subjected to a high or low cyclic pressure over a prolonged period of time induces a stress on the material. This stress over time compromises the safety and reliability of the pipeline and may lead to a catastrophic failure [112–114]. In order to prevent such failures, there is a growing need for the development of an economical, real-time, scalable, structural integrity monitoring, and sensing system for the pipeline infrastructure implemented in refineries, chemical plants and manufacturing facilities.

In literature, a number of structural health monitoring (SHM) techniques exist to evaluate the integrity of pipes, aiding in improving the safety and lifespan of the pipeline infrastructure [115, 116]. The different indicators that are monitored for elucidating the pipeline health are cyclic pressure, surface temperature, humidity, and vibration [115, 116]. Among these indicators, pressure is the most important and found to be the primary cause of damage to the pipelines [117].

A number of techniques have been proposed to monitor the pipeline pressure; such as piezo-based resistive sensors, micro-electromechanical systems (MEMS)-based capacitive sensors, and fiber Bragg grating (FBG)-based negative pressure sensors [117–119]. The fabrication process of all the sensors is very complex, which either requires a hefty cleanroom process or costly tools for precision. For example, the MEMS-based capacitive sensors require expensive substrate material, chemical etching, wire bonding, and separate housing [119]. Additive manufacturing is a viable alternative of this process, which has been previously proven for electronic system and component design [120]. Three-dimensional printing technique was previously used for designing multiple components in a pressure sensor [121–123]. However, a fully 3D-printed pressure sensor is still a feat to achieve. Most of the published research is focused on various other applications and gas pipeline is not the primary focus, which leads to over complexity, limited communication range, and scalability issues.

One of the major limitations of these sensor units is that a direct wired connection is required for data acquisition. The direct probing or wired connection limits the application of sensors and

poses a problem for inaccessible environments, like under ground buried pipelines or large chemical plants with a requirement of thousands of sensing nodes.

A number of wireless sensing approaches have been proposed as an alternate solution to overcome the disadvantages of the wired sensing methods [124, 125]. The wireless methods monitor the pressure in the pipeline by deploying a large number of active sensor nodes. The integrated nodes on the surface of the pipes transmit the data wirelessly to the interrogator. The disadvantage of active sensors is the need for an on-board battery, charging and/or replacement requirements increase the implementation and maintenance cost of the system [124–126]. Battery-free, low-cost, real-time sensing is ideal to provide a robust and economical system with longer life span and lower maintenance [127, 128].

Inductor-capacitor (LC) resonator-based passive sensor tags have been proposed in the literature for monitoring the pressure based on capacitive loading, which in turn shifts the resonance frequency [129]. LC resonant sensors operate in near-field configuration and have a limited interrogation distance [5].

A number of other IoT based sensor systems are also proposed for SHM applications, majority of them operate using digital sensor nodes that require an external power source or battery for its operation, leading to a power hungry solution [38, 39]. The digital sensor nodes require an analog-to-digital converter (ADC) and a microcontroller for reading the digital data and transmitting it back to the interrogator. For large-scale deployment, these sensor nodes are not suited for continuous monitoring due to their limited life time, increased overall cost, and additional maintenance of the system. Similar problem arises for the cold food supply chain, where a low cost long lifetime sensing platform is required [41]. To overcome the limitations of current active systems, a number of battery free passive sensing solutions have been proposed in the literature [47, 130, 131]. One such system is the battery-free Radio Frequency Identification (RFID) with integrated sensors that are suited to monitor different parameters such as temperature, humidity, and moisture [47, 48]. To collect sufficient information to determine the nature of the problem with the structure being monitored, multiple parameter monitoring becomes essential. One significant challenge in IoT

based sensing systems is to design power efficient sensor nodes that can detect and transmit the information back to the interrogator without any battery. A table of commercially available RFID technologies with sensing capability and sensitivity data is shown in Table 4.1.

Table 4.1: Commercially available RFID ICs with sensitivity data

	RFID IC	Sensor Ports	Sensitivity (dBm)
1	SL900A [[49]]	2	0
2	PhaseIV Engr	1	-8
3	Andy100 [[132]]	1	-2
4	Magnus 3 [[133]]	1	-9.9
5	NXP UCODE	0	-21
6	Higgs 4 [[134]]	0	-20

Battery-free sensing RFID platforms reported earlier are either a single CMOS IC based or multiple discrete components integrated on PCB substrate [49–51]. CMOS-based RFID platform consists of a low power on-chip sensing capability that allows a compact RFID tag design with digital ID and sensing at a shorter read range [49]. Interestingly, CMOS based digital circuitry for identification and logic control is highly efficient and requires a very low operational power [134]. On the other hand, discrete component-based platforms are equipped with a microcontroller, ADC, external memory, and multiple sensors powered by energy harvested from the interrogation signal and reflect back the digital data by modulating backscattered signal [50, 51, 135]. Although both CMOS-based and discrete component-based platforms are battery-free, the integrated power hungry ADC limits the real-time monitoring as well as the read range of the RFID sensing system.

The discussed far-field sensing platforms operate at a single frequency (902-928 MHz), which are prone to clutter due to multi-path interference and have a lower signal-to-noise (SNR) due to self-jamming, as shown in the previous chapter and open literature [127]. To overcome these limitations, the harmonic communication approach is ideal, that eliminates self-jamming, reduces multi-path interference, lowers down phase noise, and increases the SNR. Harmonic-based sensors have been previously reported in the literature for sensing temperature, and pH [136, 137] for liquid monitoring.

4.2 Analog RF Sensing

A passive harmonic RF tag with an integrated pressure sensor is designed for the real-time monitoring of the pipeline infrastructure [138]. The harmonic RF system for gas pipeline infrastructure consists of an RF tag coupled with a pressure sensor and an RF interrogator.

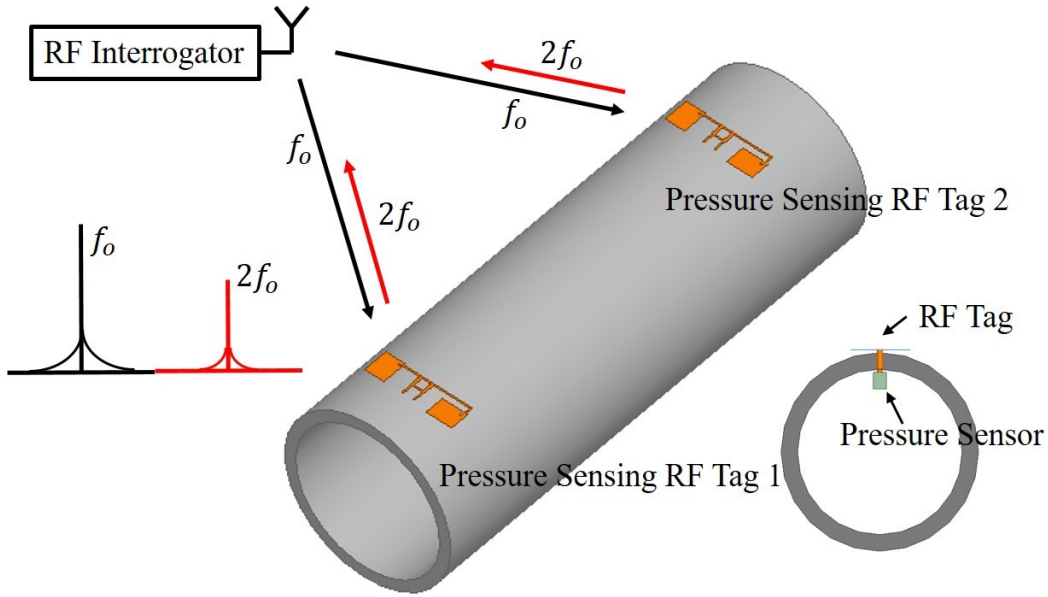


Figure 4.1: Example battery-free wireless sensing system architecture for the pipeline infrastructure

The harmonic RF sensor tag has a receiver (2 GHz) and transmitter (4 GHz) antenna, a harmonic doubler, and an integrated pressure sensor with the hybrid coupler. The integrated pressure sensor is designed with a cavity based parallel plate reactive impedance element/sensor that changes its reactance with the change in applied pressure from 0–20 psi. The designed sensor is fabricated using the additive manufacturing technique, which uses a thin liquid crystalline polymer (LCP) substrate as its diaphragm. The hybrid coupler translates the change in reactance to the change in the received 2 GHz signal's phase, with the power efficient modulation technique, which is backscattered at a harmonic frequency of 4 GHz. A schematic of the analog sensing system over the pipeline infrastructure is shown in Figure 4.1.

4.2.1 Design

The design of analog passive wireless sensing harmonic system includes: (A) 3D printed pressure sensor, (B) passive harmonic RF sensor tag, and (C) harmonic RF interrogator.

4.2.1.1 3D Printed Pressure Sensor

The designed pressure sensor is an air cavity based parallel plate capacitor, where one electrode has a fixed position and second electrode is deformable due to the pressure as shown in Figure 4.2. The air cavity in between the electrode acts as dielectric medium and holds a single atmospheric pressure or reference pressure. The external pressure is applied through the tunnel directly onto the diaphragm with copper electrode.

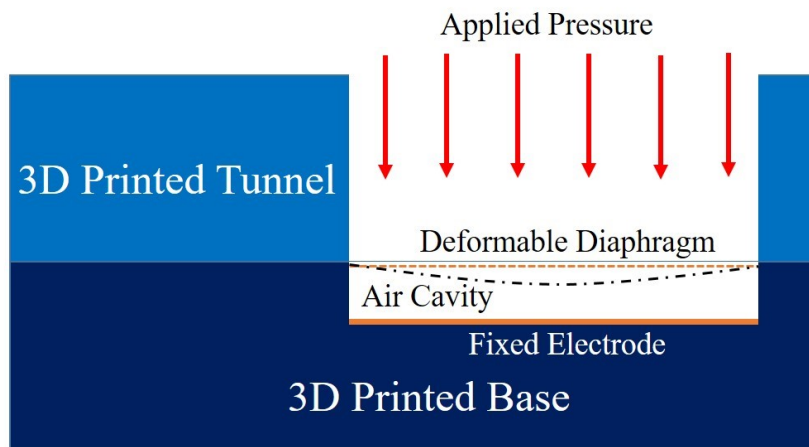


Figure 4.2: Air cavity-based fully 3D printed pressure sensor

The pressure sensor is fabricated in three parts, as shown in Figure 4.3. The first component has the air cavity with the fixed electrode and electrical access holes for rigid coaxial cable. The copper is plated into the cavity's bottom of the 3D printed part. The second component is the deformable electrode, which is realized using 18 μm -thick LCP film with copper plating. The LCP film is fixed on top of the cavity, such that it makes an electrical connection with the outer shell of the rigid coaxial cable. The third component is a pressure tunnel that directs the pressure onto the electrodes and holds the LCP film in its place. The top part has four alignment legs, which perfectly fits with the bottom component. An extra layer of polymer resin is coated on top of the fully assembled

pressure sensor and cured under ultraviolet (UV) light, for eliminating any pressure leaks into or from the air cavity and acts as a seal of the pressure sensor. The outer resin layer also holds the three separately fabricated components together and replace any use of extra adhesive.

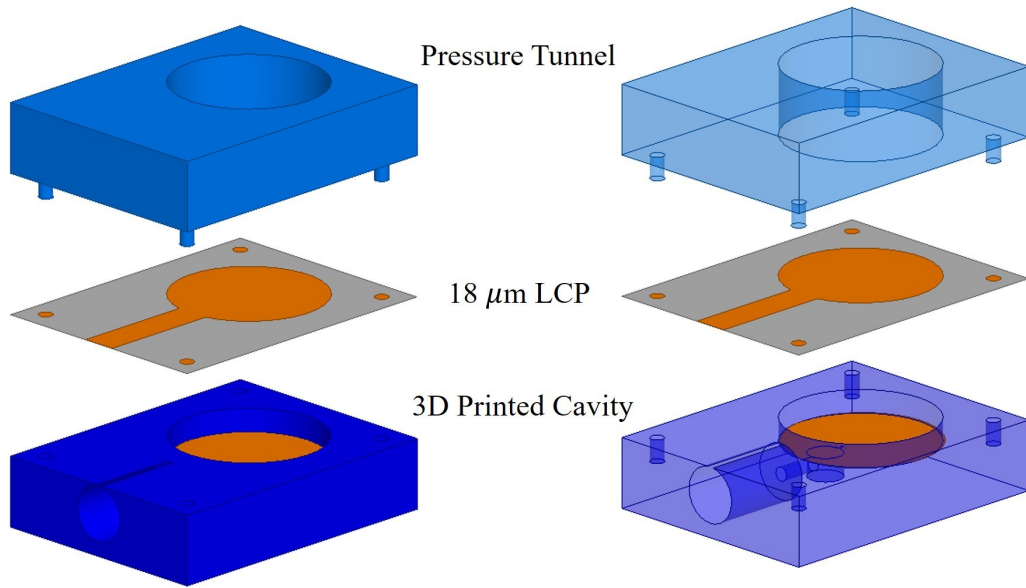


Figure 4.3: Exploded view of 3D printed pressure sensor with three main components

Figure 4.4 shows a fully assembled view of the fabricated pressure sensor, where the three pressure sensor parts fit perfectly and allow a coaxial cable to make an electrical connection to the electrodes for reactance measurement.

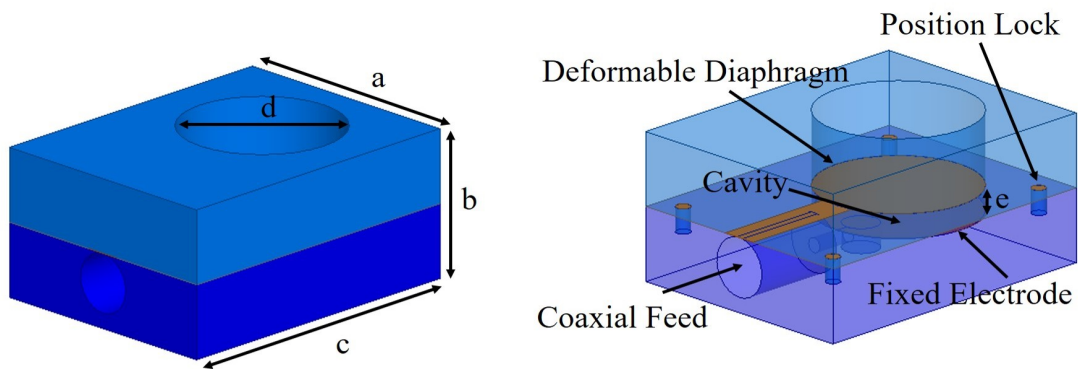


Figure 4.4: Fully assembled 3D printed pressure sensor with component annotation and dimensions

The total volume of the fabricated sensor is $10 \times 13 \times 6 \text{ mm}^3$. The diameter of the pressure tunnel is 6.6 mm and the depth of the pressure cavity is 1 mm. The change in pressure deforms

the LCP electrode and reduces the separation of the two electrodes, therefore a change in electrical response, which can be measured using an impedance analyzing equipment.

Table 4.2: Dimensions of the 3D-printed pressure sensor

Parameter	a	b	c	d	e
Dimensions (mm)	10.0	6.0	13.0	6.6	1.0

A sealed cavity-based sensor with a deformable diaphragm in a parallel plate configuration is used to measure the pressure, ranging from 0 to 20 psi. The pressure sensor is integrated inside a polypropylene plastic pipe and probed using an SMA connector from the outside, as shown in Figure 4.5A. A vector network analyzer (VNA) is used in a direct wired configuration to measure the impedance of the pressure sensor at 2 GHz, as shown in Figure 4.5B.

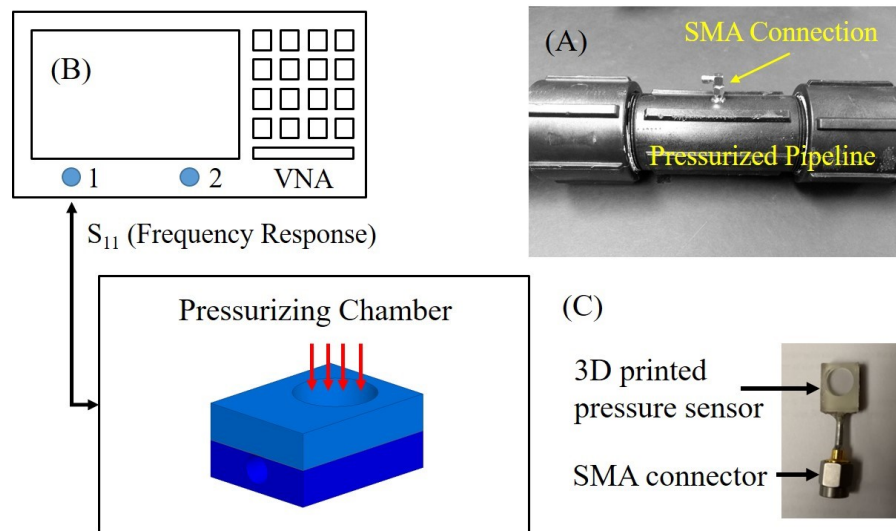


Figure 4.5: (A) Pressurizing chamber (pipe) with integrated pressure sensor, (B) Schematic of the measurement setup, and (C) Fabricated pressure sensor

The measured impedance is plotted on a normalized Smith chart for varying pressure, as shown in Figure 4.6. The reactive impedance changes from 10.23–17.80 Ω for the applied pressure. A small series resistance is observed in the acquired data, which is due to the parasitics associated with the high frequency and losses in the cable. The direct wired measurements support the hypothesis of significant change in reactive impedance due to the applied pressure difference between the sealed

cavity and pipeline pressure. Moreover, it provides an insight into the parasitic real impedance of the sensor and provide data for simulating the ideal phase shift for a given range of impedance.

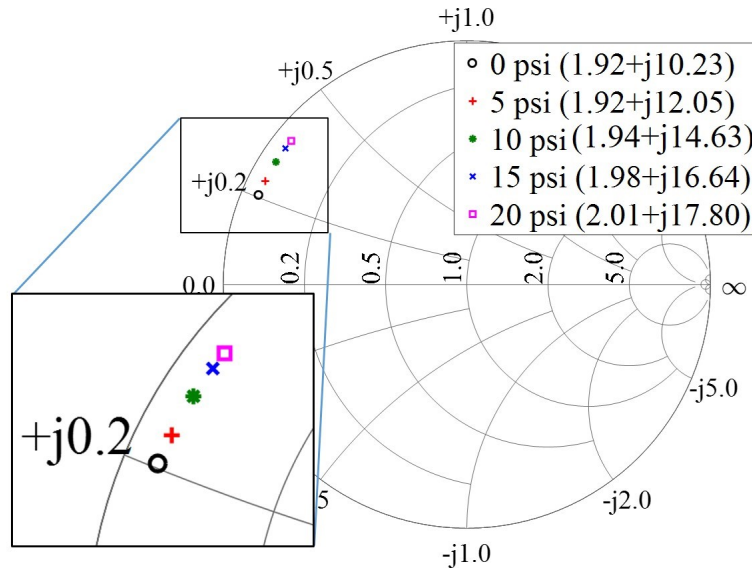


Figure 4.6: Measured impedance at 2 GHz for pressure range from 0 to 20 psi with a direct wired connection using vector network analyzer (VNA)

4.2.1.2 Harmonic RF Sensor Tag

The passive harmonic RF tag uses a reactance-based phase shifting mechanism for wirelessly measuring the change in the applied pressure. The hybrid coupler is used as a phase shifter, which is a four-port reciprocal device with input, output, isolation, and coupled ports. The phase shifter is designed and simulated using ANSYS HFSS[®] (2019, ANSYS, Inc., Canonsburg, PA, USA) on an FR-4 substrate with a dielectric constant (ϵ_r) of 4.4, thickness of 1.52 mm and a loss tangent ($\tan \delta$) of 0.02. The phase shifter operates at 2 GHz with a 3 dB coupling factor and a 20 dB isolation.

The phase shifter's input is connected to a 2 GHz patch antenna for receiving the continuous RF wave from the interrogator. The received RF signal is forwarded to the output and the coupled ports of the coupler, to which a reactive impedance pressure sensor is connected. The RF signal at the output and the coupled ports experience a total internal reflection due to the termination of a reactive sensor element. The internally reflected signal is received at the isolated port without

any internal power loss, but with a shifted phase according to the reactance. The isolated port is connected to a non-linear device (Schottky diode), which generates a second harmonic signal at 4 GHz. The Schottky diode (BAT 15-03) doubles the shifted phase along with a frequency. The phase modulated 4 GHz output of the frequency doubler is transmitted back using a patch antenna. The schematic of the designed harmonic RF tag is shown in Figure 4.7 along with the dimensions.

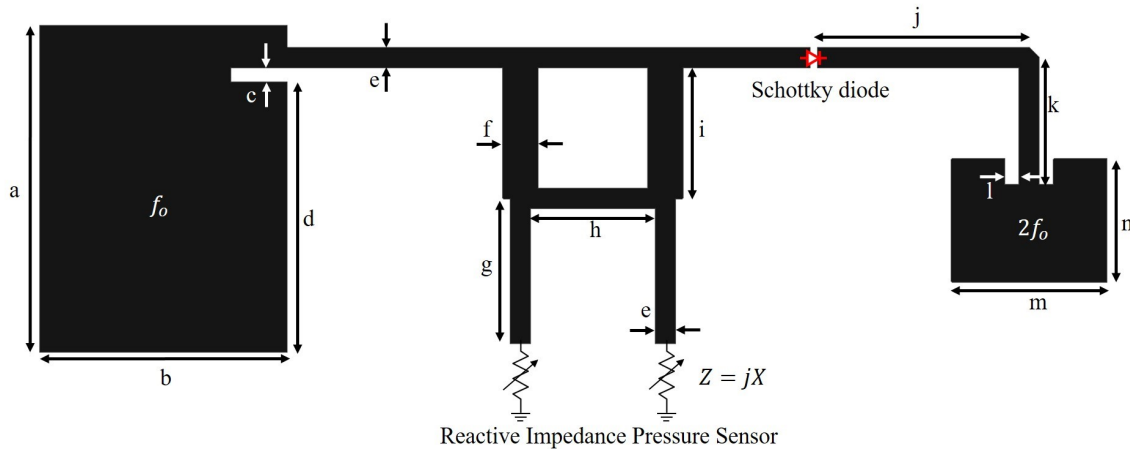


Figure 4.7: Schematic of the pressure sensing harmonic RF tag along with its dimensions. Signal received using 2 GHz antenna forwarded to the hybrid coupler for phase shift according to the integrated pressure sensor and the second harmonic signal with double shifted phase, generated using diode frequency doubler, is transmitted out using 4 GHz patch antenna

Table 4.3: Dimensions of the analog pressure sensor tag

Parameter	a	b	c	d	e	f	g
Dimensions (mm)	46.0	35.0	2.0	46.14	2.86	4.92	20.5
Parameter	h	i	j	k	l	m	n
Dimensions (mm)	17.64	18.47	30.0	18.0	2.0	22.0	17.32

The fundamental and harmonic antennae are placed in cross-polarization for increasing the SNR and minimizing the interference at the interrogator. The simulated and the measured frequency responses for both the fundamental and the harmonic patch antenna are shown in Figure 4.8. The measured response closely matches the simulated response, and the observed minimal differences are due to fabrication tolerances.

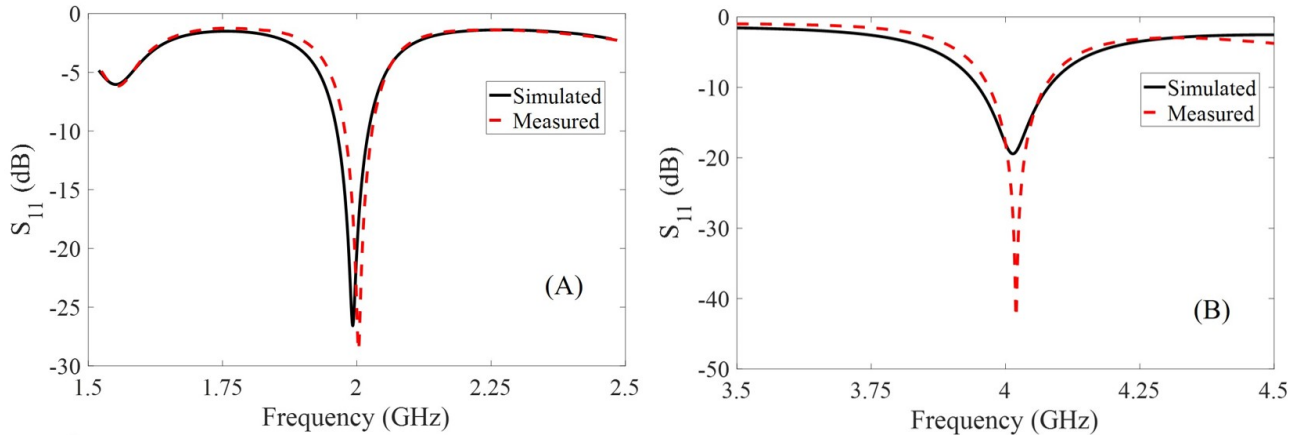


Figure 4.8: Simulated and measured frequency response; (A) Fundamental (2 GHz) and (B) Harmonic antenna (4 GHz)

4.2.1.3 Harmonic RF Interrogator

The harmonic RF interrogator is designed to communicate with the passive phase shifting-based RF tag. The interrogator generates an RF signal using a VNA with a signal strength of 13 dBm at 2 GHz and it is transmitted towards the harmonic RF tag using a Vivaldi antenna. The harmonic RF tag receives the fundamental frequency and backscatters the pressure sensor information modulated at 4 GHz harmonic signal. The harmonic interrogator receives the modulated signal using a Vivaldi antenna in a cross-polarized configuration.

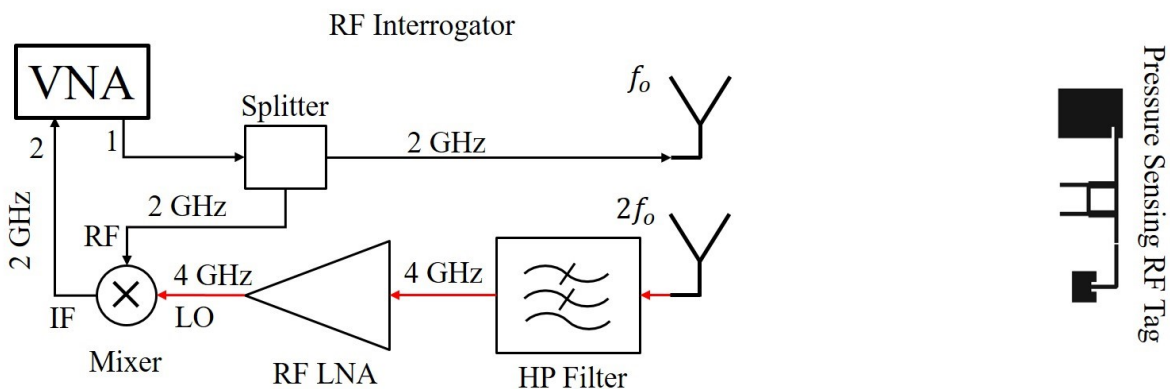


Figure 4.9: Schematic of the harmonic RF Interrogator consist of a VNA for RF source and phase measurement unit, transmitting and receiving antennas, and miscellaneous RF peripheral circuits for communicating with the harmonic RF sensor tag

The received harmonic signal is amplified using LNA's (ZX60-53LNB-S+ and ZX60-43-S+)

with a total amplification of 34 dB. The amplified 4 GHz signal is fed into the RF port of the mixer for down converting it to a 2 GHz signal. A reference signal is extracted from the 2 GHz transmission signal using an RF splitter and fed into the LO port of the mixer. The down converted output signal at 2 GHz with the modulated phase information is acquired using VNA at the IF Port of the mixer. The schematic of the harmonic RF interrogator communicating with the harmonic RF sensor tag is shown in Figure 4.9.

4.2.2 Results

Initially, a simulation-based validation study is performed in order to test the phase shifting mechanism using a reactive element. A four-port phase shifter is designed in Keysight's ADS RF simulation software (2017, Keysight Technologies, Santa Rosa, CA, USA) with a coupled reactive impedance element. The range of reactive impedance is referenced from the previous direct wired measurements shown in Figure 4.6.

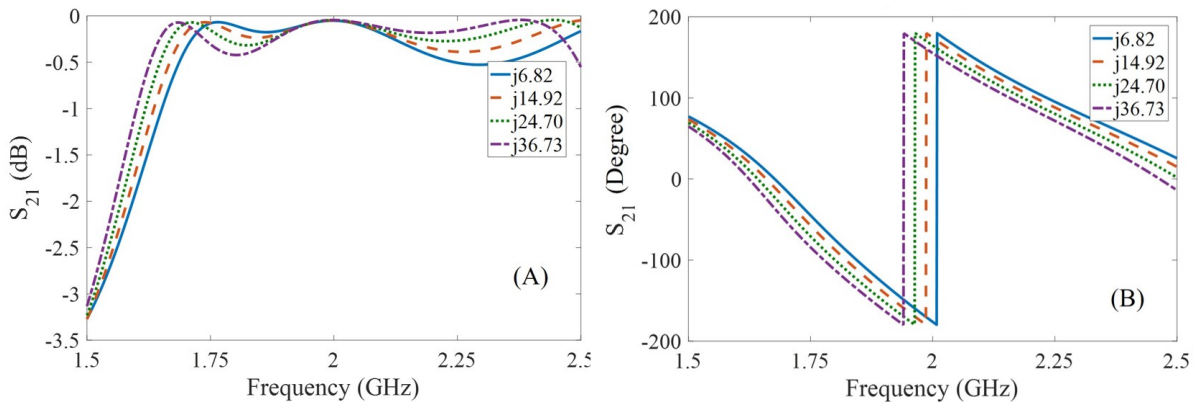


Figure 4.10: Simulated frequency response of the designed phase shifting hybrid coupler with a variable reactance from 6.82Ω to 36.73Ω : (A) No power loss is observed at 2 GHz due to changing reactance, (B) A total phase shift of 28.55° is observed at 2 GHz due to changing reactance

The reactive elements are connected to the two of the four ports of hybrid coupler, while using two leftover ports as input and output of 2 GHz signal. The S-parameter study is used in ADS for validating the phase shifting mechanism. The simulated transmission coefficient (S_{21}) of the phase shifter is shown in Figure 4.10. The phase of the transmitted signal at 2 GHz is changed from

-176.21° to 155.2° ($\Delta\Phi = 28.55^\circ$) with a change in coupled reactance from $6.82\text{--}36.73\ \Omega$. The simulated phase shift due to reactive impedance is significant for practical implementation and can be easily detected using a standard phase measurement device. Moreover, the transmitted power at 2 GHz remains unchanged, which shows no loss at the operating frequency for the entire range of the changing reactive impedance. Pressure information is modulated on the 2 GHz signal in the form of a phase with no power loss is a significant feat for passive RF tag technology, where a small amount of energy saving can lead to a huge improvement in range or signal-to-noise ratio. In this paper, the no power loss advantage is exploited for better harmonic generation using the Schottky diode, where the frequency conversion losses are inversely proportional to the input power of the signal [94].

The proposed technique is validated by performing two experiments. First, the phase shifter is designed in ANSYS HFSS[®] (2019, ANSYS, Inc., Canonsburg, PA, USA) for 2 GHz and fabricated on a FR-4 board for validating the simulation results. The fabricated phase shifter's response, without a transmitter or a receiver antenna, is measured using the VNA at 2 GHz. A power combiner is used to connect a single reactive element (Varactor diode) to the two ports of the phase shifter. The reactive impedance of the Varactor diode is varied by applying a bias voltage from 0 V to 1.5 V. The change in phase, due to the change in reactance of the transmission coefficient (S_{21}) at 2 GHz in direct wired configuration, is shown in Figure 4.11. The 1.5 V change in bias potential leads to a change of 18.28° in phase. The fabricated phase shifter performed in a similar way to the simulated results. Next, the receiver and transmitter patch antennae are connected to the phase shifter with a harmonic doubler and the wireless phase measurement experiment is performed. The harmonic RF sensor tag is placed at a separation of 8 inches from the interrogator antenna for wireless communication. The wirelessly acquired phase change due to the applied bias voltage is shown in Figure 4.11. A phase shift of 36.78° is observed for the wireless configuration, which is approximately double the single frequency wired configuration. In Figure 4.11, both responses are the average plots of three repetitions and error bars represent the standard deviation between all readings. A constant phase offset with reference to 0° is added in both the wired and wirelessly

acquired data.

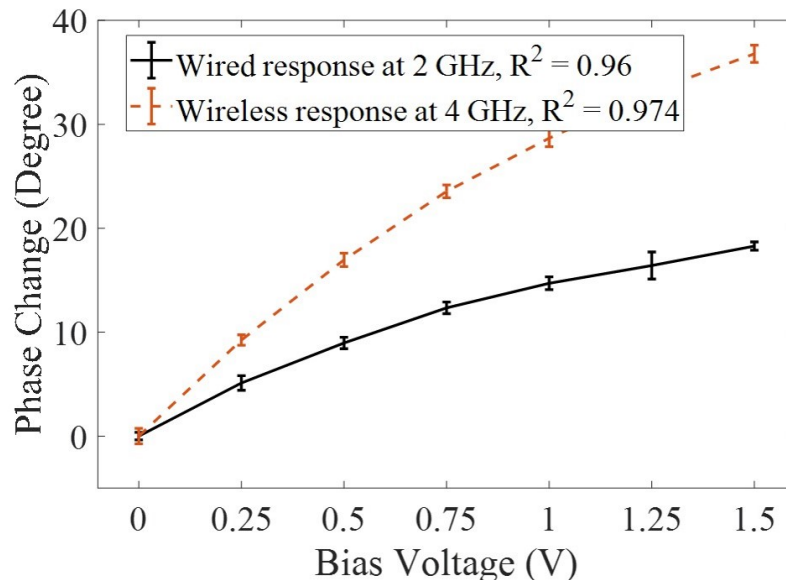


Figure 4.11: Measured phase change due to variable reactance introduced with direct current (DC) biasing the varactor diode in a wired configuration ($\Delta\Phi = 18.28^\circ$) using a single frequency approach and wireless configuration ($\Delta\Phi = 36.78^\circ$) using the harmonic frequency approach

Second, a pressurized pipeline setup is designed to test the harmonic RF tag with an integrated pressure sensor. A section of the polypropylene pipe, 24 inches in length and 2 inches in diameter, is sealed using threaded polypropylene caps.

An 1/8 inch precision flow valve is connected to both the ends of the pipe for controlling the pressure. A high pressure nitrogen cylinder is used to pressurize the pipe through a compressed yor-lok fitting coupled to a precision flow valve. Due to the safety of the research lab and personnel, natural gas pressure pipe application is demonstrated using nitrogen gas. A 20 psi safety valve is connected that sets the limit on the maximum applied pressure. The designed pressure sensor can also work at higher pressure ranges, but due to safety, the upper limit is set to 20 psi for this work. The working principle of the designed sensor is demonstrated for a limited pressure range from 0 to 20 psi. The integrated pressure sensor inside the pipeline is connected to the designed harmonic RF tag, as shown in Figure 4.12. The harmonic RF tag is capable of receiving RF signal at 2 GHz and modulate the phase of output signal according to the applied pressure.

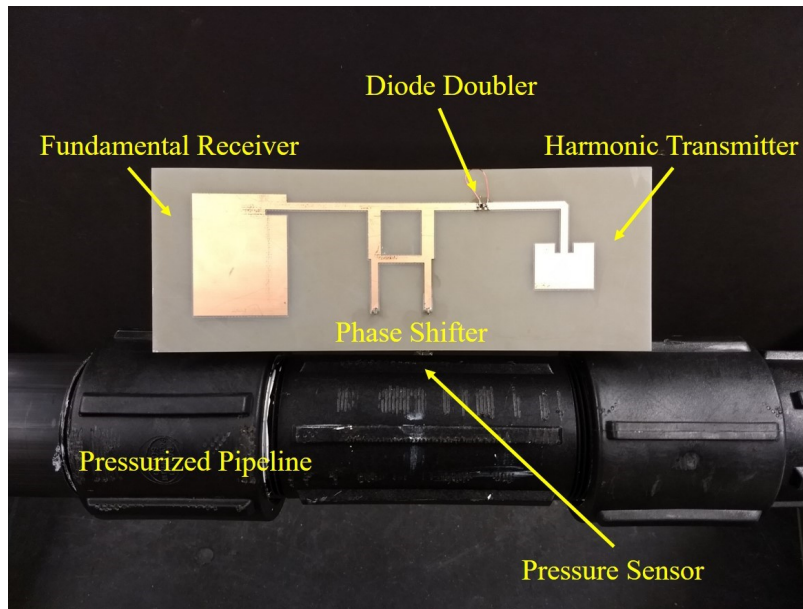


Figure 4.12: Pressurized polypropylene pipeline setup with the fabricated harmonic RF sensor tag for real-time wireless communication

In our experiment, the applied pressure range is from 0 to 20 psi. Due to applied pressure, the harmonic RF interrogator, placed at 18 inches' distance from the RF tag, measured a phase shift of 16.6° in the received signal at 4 GHz. The wirelessly measured phase is shown in Figure 4.13, where the measurements are acquired at an interval of 5 psi. All measurements are performed thrice for checking the repeatability and standard deviation at each acquisition point, as shown in Figure 4.13. The plotted average data of three repetitions show a linearity of 0.9915 (R^2), which is comparable to existing commercial pressure sensors [139].

The designed harmonic RF sensor tag has a sensitivity of detecting a minimum change of 1Ω in reactive impedance at 2 GHz and is compatible with other types of reactive impedance based sensors for measuring higher pressure or other physical parameters such as temperature, moisture, etc. The interrogation range of the system can be further enhanced by radiating the maximum allowable power of 4 W, whereas in this work, only 19 mW was used. A maximum communication range of 15 ft can be achieved with 36 dBm (4W) transmitted power at 2 GHz, 20 dB doubler diode conversion loss and -90 dBm receiver sensitivity at 4 GHz.

The 3D printed pressure sensor eliminated the complex fabrication requirement in cleanroom,

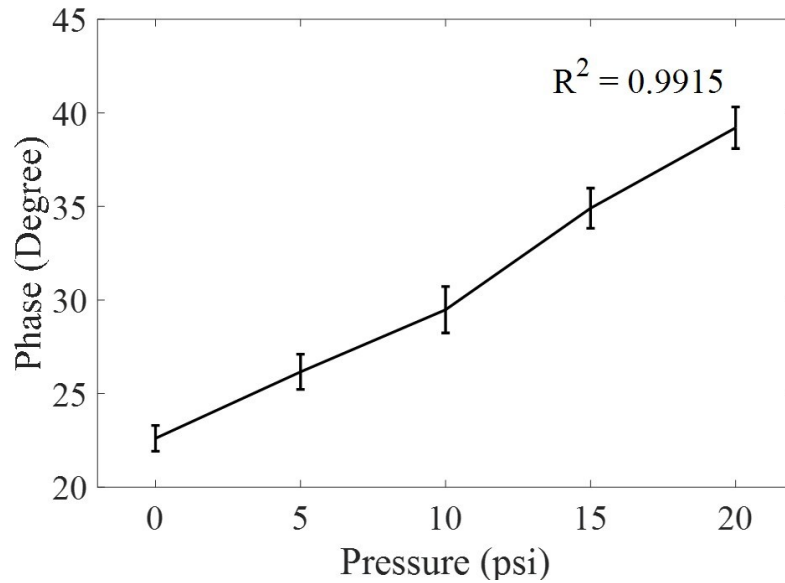


Figure 4.13: Phase change is wirelessly measured using harmonic RF interrogator due to applied pressure ranging from 0 to 20 psi. The linearity of change in phase due to pressure is represented using coefficient of determination ($R^2 = 0.9915$)

while providing similar capabilities, such as piezo-based resistive sensors, MEMS-based capacitive sensor, or FBG-based pressure sensors [117–119]. The passive wireless feature successfully communicates the pressure information from the pipe to interrogator, while eliminating the battery requirement and lowering down the maintenance cost [127].

4.2.3 Discussion and Limitations

To avoid the limitations of the power-hungry ADC, we used the alternative solution of analog modulation to send the sensor information directly over the backscattered signal. But the phase modulation techniques are affected by noise in the propagation environment. Furthermore, in case of direct phase modulation of the sensor information, the distance between the tag and the interrogator should be calibrated in order to avoid the ambiguities towards change in distance. An alternative approach to analog sensing for multisensor integration and detection is shown in Appendix A. The battery-free multisensor system uses frequency modulation technique to reflect back sensor data, which is immune to multipath effect or spatial placement. But it also suffers

from other limitations like only a single RF tag can be in the field of view for reliable information transfer.

Therefore, to avoid ambiguity issues with analog RF sensing and digitization issues with digital RF sensing, a new platform called **Hybrid RFID sensing** is proposed. The hybrid RFID platform use power efficient ID communication mechanism from conventional RFID infrastructure and combine with power efficient analog sensing to create a novel solution for sensor integration problem in battery free tags.

4.3 Hybrid RFID Sensing

The conventional single-frequency RFID tag IC's without sensing capabilities are very sensitive [134]. The minimum power required to activate the IC is only -20 dBm (10uW), which translates into longer communication range of about 50-ft. On the other hand, the digital RFID tags with sensor integration capabilities need at least -6 dBm [49, 132]. The higher power requirement reduces the range significantly to only few feet. The external digital sensor consumes more power due to operations like analog-to-digital conversion. The efficient ADC's inside ultra-low power microcontroller can take up to 0.6 mA of current at 2.2V input and requires additional energy for overhead computation like register update, calibration and readout [140]. The minimum power required to acquire data using inbuilt ADC is approximately 1.32mW, which is significant without even considering the additional power required to actuate sensor. To harvest enough power using a typical energy harvester circuit with 20-25% efficiency, a higher input power is required, which is -6 dBm in existing digital sensor integrated RFID tags. The alternative technologies of analog sensing do not put additional constraints over power requirement, therefore superior over ADC mechanism. But analog sensing has it's own limitations, which can be tackled in this section by integrating it with digital ID tags. Therefore the power requirements stay as low as ID only mechanism but the tag capabilities will include sensing as well.

The hybrid RFID sensing system is a combined solution using digital and analog signals. It utilize the power efficient digital ID mechanism from conventional systems and analog sensing

from latest work shown in previous section. It takes best parts from both digital and analog worlds. Hybrid RFID sensing system does not affect the communication range and reliably transmits the sensor's information. The analog sensor data can be received using an hybrid interrogator and digitized with high precision ADCs. The data frame for hybrid RFID tag is shown in Table.4.4.

Table 4.4: Data frame format for Digital ID with Analog Sensor Data Reply

P	EPC	ST	SP	CRC-16	ASD
---	-----	----	----	--------	-----

where, P is preamble, EPC is Electronic Product Code, ST is Sensor Type, SP is Sensing Parameter, CRC is Cyclic Redundancy Check, and ASD is Analog Sensor Data. The ASD is further divided into two components, as shown in Table.4.5. The data frame has both digital bit and analog sensor information, therefore, it is called an hybrid method for RFID sensing.

Table 4.5: Data frame format for Analog Sensor Data Reply

RAD	TG	SAD
-----	----	-----

where RAD is the reference analog sensor data, TG is the time gap, and SAD is the sensor analog data. RAD is used as a reference measurement for eliminating any ambiguity and precise detection of the change in phase of the RF signal. The design of hybrid RFID sensing is presented below, which use the digital RFID work shown in Appendix B as building block for providing logic and ID to the analog tag.

4.3.1 Design

The hybrid sensing system is designed for both single and harmonic frequency operation. The digital end with energy harvester, microcontroller, modulator, and non-linear transmission line stays the same as explained in Appendix B. The novel analog sensing hybrid coupler is integrated with digital tags in unique way for both frequency operations. The architecture of the designed RFID tags are shown below.

4.3.1.1 Hybrid Single-Frequency RFID Tag Architecture

The hybrid single-frequency RFID tag has three main components; a digital RFID system, a hybrid coupler, and a 915 MHz antenna. The digital RFID system is used as explained in section B.2.1. The schematic of the hybrid single-frequency RFID tag is shown in Fig.4.14.

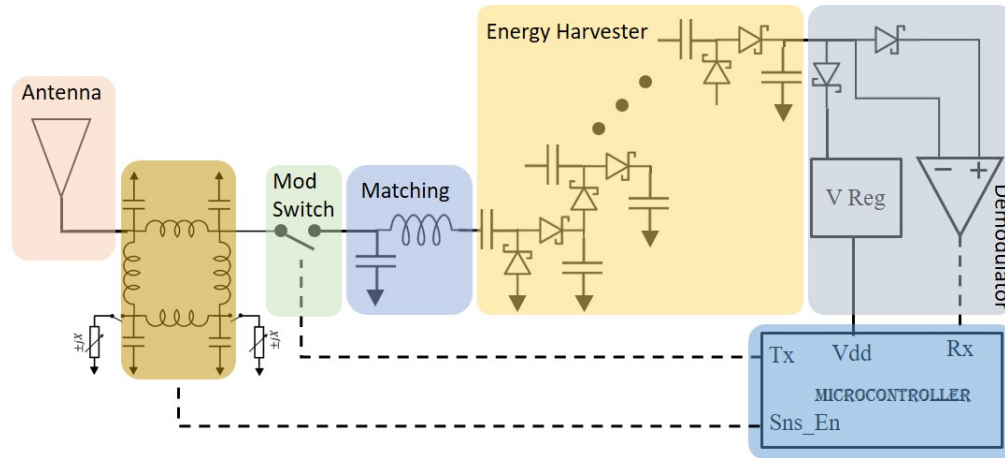


Figure 4.14: Schematic of the hybrid single-frequency RFID tag

A new *hybrid coupler* is designed to operate at 915 MHz using lumped components for sensing the change in impedance without any requirement of additional power.

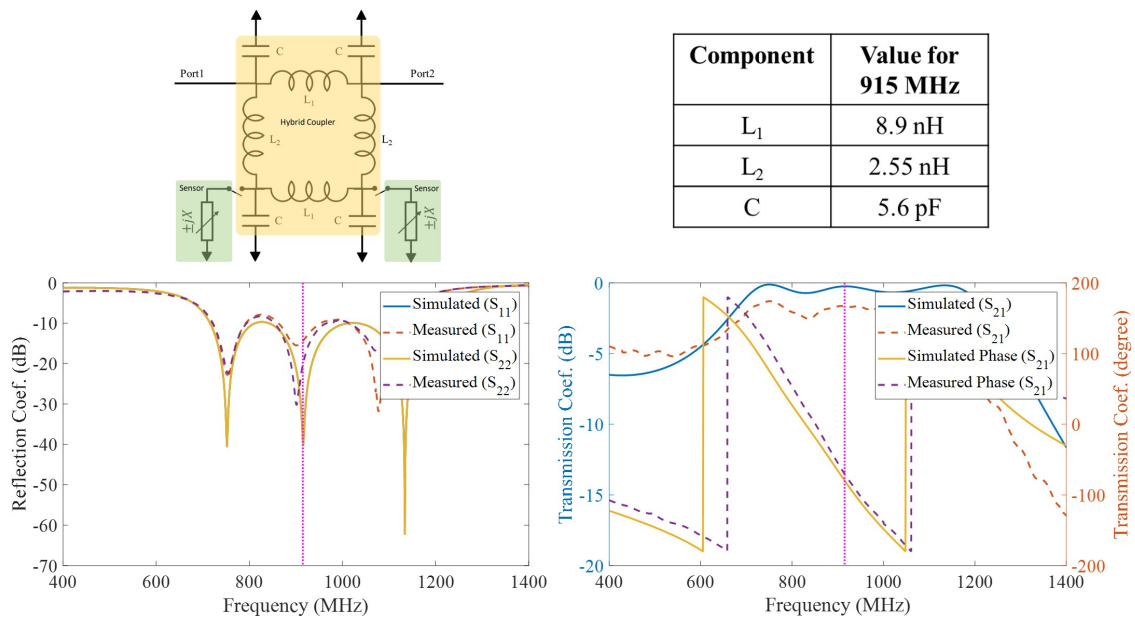


Figure 4.15: (A) Schematic of a lumped hybrid coupler with integrated reactance sensors for modulation, (B) Simulated and measured response of the coupler at 915 MHz

The high frequency (2 GHz) hybrid coupler for power efficient phase modulation was shown in previous section. Based on the same fundamental principles the miniaturized 915 MHz coupler is simulated in Keysight’s ADS RF simulation software (2017, Keysight Technologies, Santa Rosa, CA, USA) for the correct component values and modulation check. The designed coupler with schematic and frequency response is shown in Fig.4.15. The value of inductors ($L_1 = 8.9nH$ and $L_2 = 2.55nH$) and capacitors ($C = 5.6pF$) are tuned according to the additional PCB parasitics. An ultra-low power RF switch is used to connect and disconnect in between the reference impedance and sensor impedance elements.

A Varactor diode is attached as an impedance sensor, which changes its capacitance due to the applied voltage across its terminals. The change in capacitance will shift the phase of the input signal accordingly. The change in phase due to the applied voltage is measured using VNA. The acquired phase data is shown in Fig.4.16.

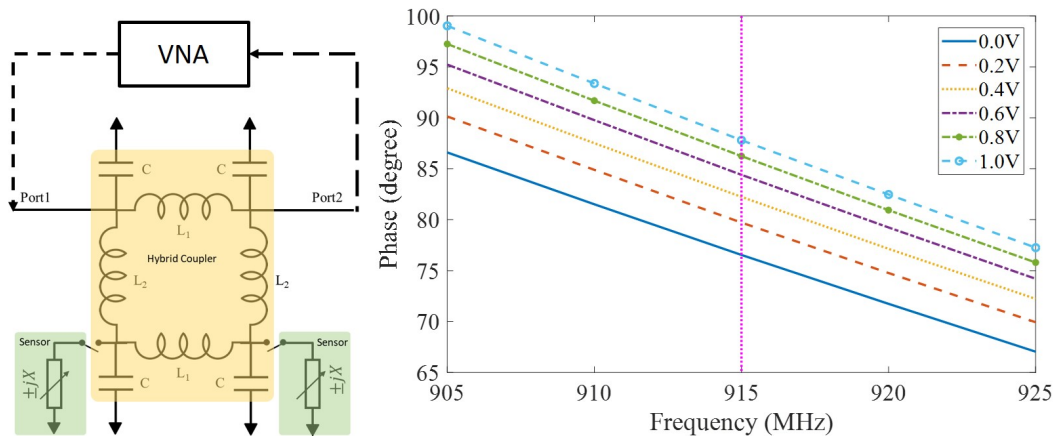


Figure 4.16: Measured change in phase due to shift in capacitance of the varactor diode using VNA, at 915 MHz

The phase-shifting hybrid coupler changed its phase from 76.53° to 87.80° for applied voltage of $0.0V$ and $1.0V$, respectively. The coupler can be integrated with the tag as shown in its architecture schematic. An antenna will be connected at port 1 and a impedance mismatching modulation switch at port 2, which will reflect back the input signal with shifted phase in 'OFF' state. The phase will shift twice due to forward and backward propagation via the coupler.

A hybrid single-frequency RFID tag is tested with antenna using direct wired connections as shown in Fig.4.17A. The measured reflected signal is acquired using an oscilloscope and the plot is shown in Fig.4.17B. The sensor's capacitance information is hidden in phase of the sensor analog data (SAD), which can be extracted by demodulation using heterodyne mixer. The reference analog data (RAD) can be used to compare the phase shift of the SAD, which eliminates the effects of any multipath reflection and tag movement.

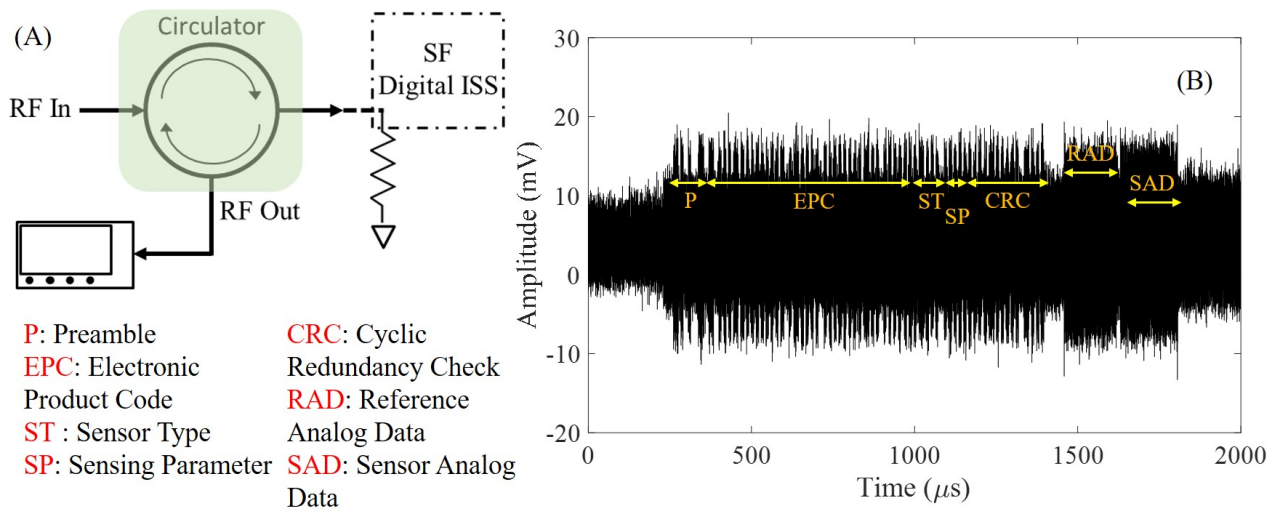


Figure 4.17: (A) Measurement setup for testing backreflection at 915 MHz, (B) Measured backreflected signal with digital ID and analog sensor data.

A **915 MHz meandered dipole antenna** is designed in ANSYS HFSS[®] (2019, ANSYS, Inc., Canonsburg, PA, USA) to receive and transmit the information from the ISS tag. The designed antenna is shown in Fig.4.18 with dimensions in Table.4.6 and frequency response is shown in Fig.4.19. The simulated parameters match closely with the measurement, while the simulated gain is 0 dBi.

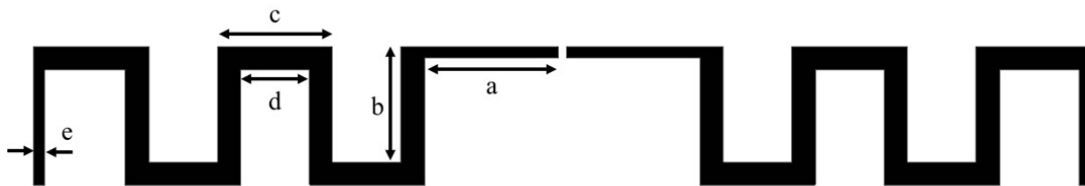


Figure 4.18: Meandered Dipole antenna for 915 MHz

Table 4.6: Dimensions of the designed 915 MHz antenna

Parameter	a	b	c	d	e
Dimensions (mm)	11.6	10.0	10.0	6.0	1.0

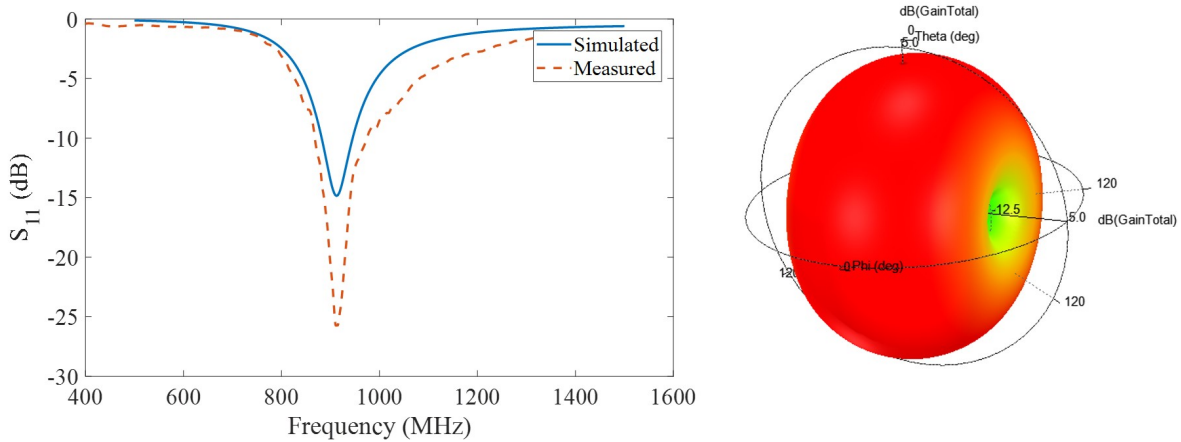


Figure 4.19: (A) Simulated and Measured frequency response of the 915 MHz antenna, (B) Simulated radiation pattern of the antenna

4.3.1.2 Hybrid Harmonic-Frequency RFID Tag Architecture

The hybrid harmonic-frequency RFID tag also has three main components; a digital RFID system, a hybrid coupler operating at 434 MHz, and a 434 & 868 MHz antenna pair. The digital RFID system is used as explained in section B.2.2. The schematic of the hybrid harmonic-frequency RFID tag is shown in Fig.4.20.

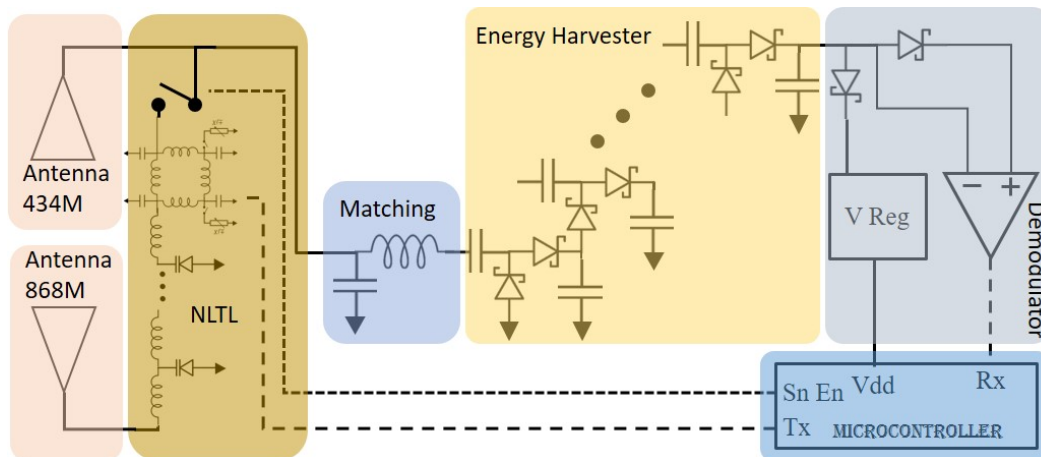


Figure 4.20: Schematic of the hybrid harmonic-frequency RFID tag

A new **hybrid coupler** is designed to operate at 434 MHz using lumped components for sensing the change in impedance without any requirement of additional power. The miniaturized 434 MHz coupler is simulated in Keysight’s ADS RF simulation software (2017, Keysight Technologies, Santa Rosa, CA, USA) for the correct component values and modulation check. The designed coupler with schematic and frequency response is shown in Fig.4.21. The value of inductors ($L_1 = 18.5nH$ and $L_2 = 13nH$) and capacitors ($C = 10.5pF$) are also tuned according to the additional PCB parasitics due to the trace lines and connectors. An ultra-low power RF switch is used to connect and disconnect in between the reference impedance and sensor impedance elements as in previous section.

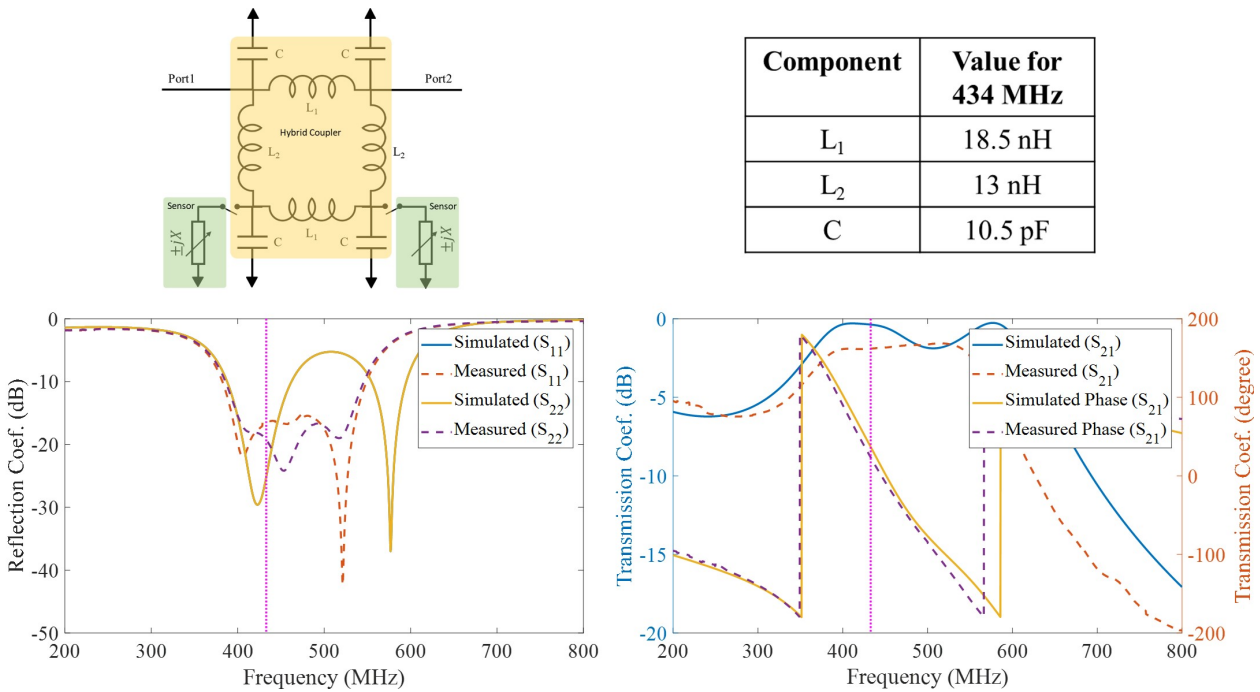


Figure 4.21: (A) Schematic of a lumped hybrid coupler with integrated reactance sensors for modulation, (B) Simulated and measured response of the coupler at 434 MHz

A Varactor diode is attached as an impedance sensor, which changes its capacitance due to the applied voltage across its terminals. The change in capacitance will shift the phase of the input signal accordingly. The change in phase due to the applied voltage is measured using VNA. The acquired phase data is shown in Fig.4.22.

The phase-shifting hybrid coupler changed its phase from -86.34° to -75.25° for applied

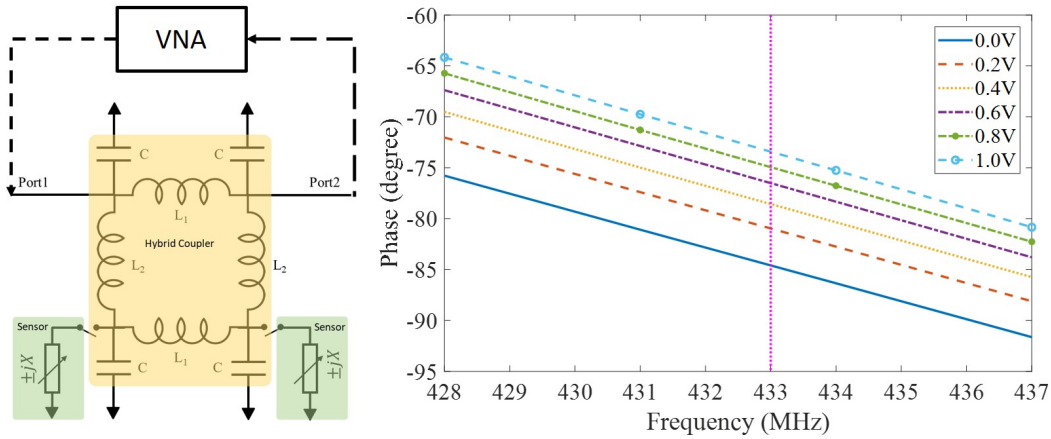


Figure 4.22: Measured change in phase due to shift in capacitance of the varactor diode using VNA, at 434 MHz

voltage of 0.0V and 1.0V, respectively. The coupler can be integrated with the tag as shown in its architecture schematic. An antenna will be connected at port 1 and a harmonic generating NLTL at port 2, which will transmit back the 868 MHz signal with shifted phase. The phase will shift twice due to frequency doubling with harmonic generation.

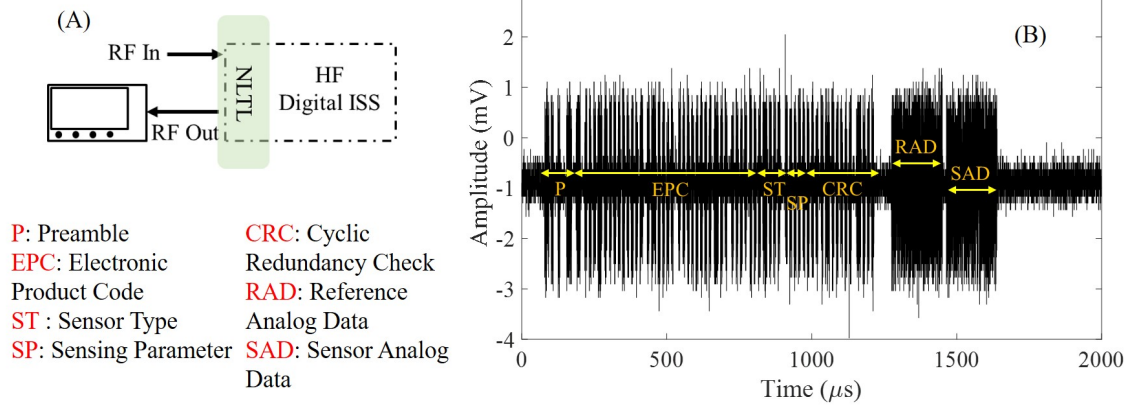


Figure 4.23: (A) Measurement setup for testing backreflection at 868 MHz, (B) Measured backreflected signal with digital ID and analog sensor data.

A hybrid harmonic-frequency RFID tag is tested without antenna using direct wired connections as shown in Fig.4.23A. The measured reflected signal was acquired using oscilloscope and plotted in Fig.4.23B. The modulation depth (>90%) of the backreflected signal is greater than the single frequency operation, which corresponds to better SNR and higher detection probability. The

digital part can be demodulated and decoded as it is shown in section B.3. The analog data is read separately with additional elements using a hybrid multi-frequency interrogator. The phase information from RAD and SAD region can be compared for finding a reference change in phase due to the sensor's impedance change.

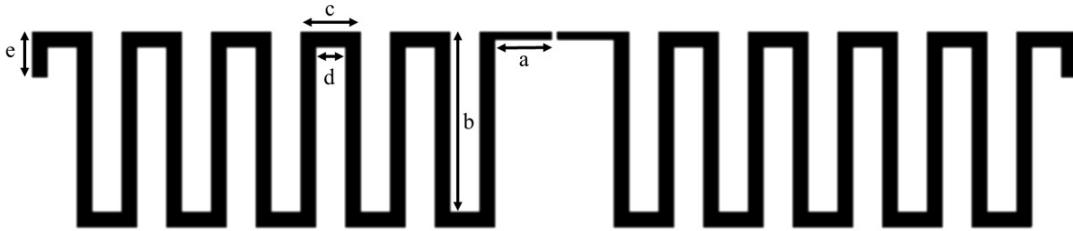


Figure 4.24: Meandered Dipole antenna for 434 MHz

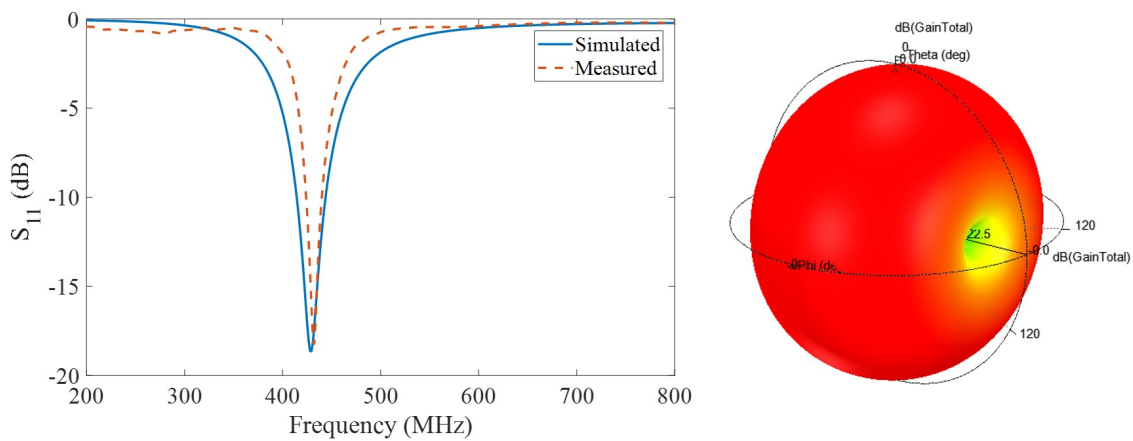


Figure 4.25: (A) Simulated and Measured frequency response of the 434 MHz antenna, (B) Simulated radiation pattern of the antenna

Table 4.7: Dimensions of the designed 434 MHz antenna

Parameter	a	b	c	d	e
Dimensions (mm)	7.6	24.0	8.0	4.0	6.0

A **434 MHz meandered dipole antenna** is designed in ANSYS HFSS[®] (2019, ANSYS, Inc., Canonsburg, PA, USA) to receive the information from the interrogator. The designed antenna is shown in Fig.4.24 with dimensions in Table.4.7 and frequency response is shown in Fig.4.25. The simulated parameters match closely with the measurements.

A *868 MHz meandered dipole antenna* is designed in ANSYS HFSS[®] (2019, ANSYS, Inc., Canonsburg, PA, USA) to transmit the information to the interrogator. The designed antenna is shown in Fig.4.26 with dimensions in Table.4.8 and frequency response is shown in Fig.4.27. The simulated parameters match closely with the measurement.

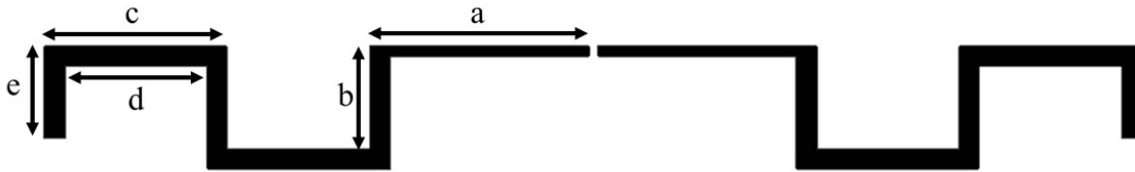


Figure 4.26: Meandered Dipole antenna for 868 MHz

Table 4.8: Dimensions of the designed 868 MHz antenna

Parameter	a	b	c	d	e
Dimensions (mm)	21.6	10.0	18.0	14.0	9.0

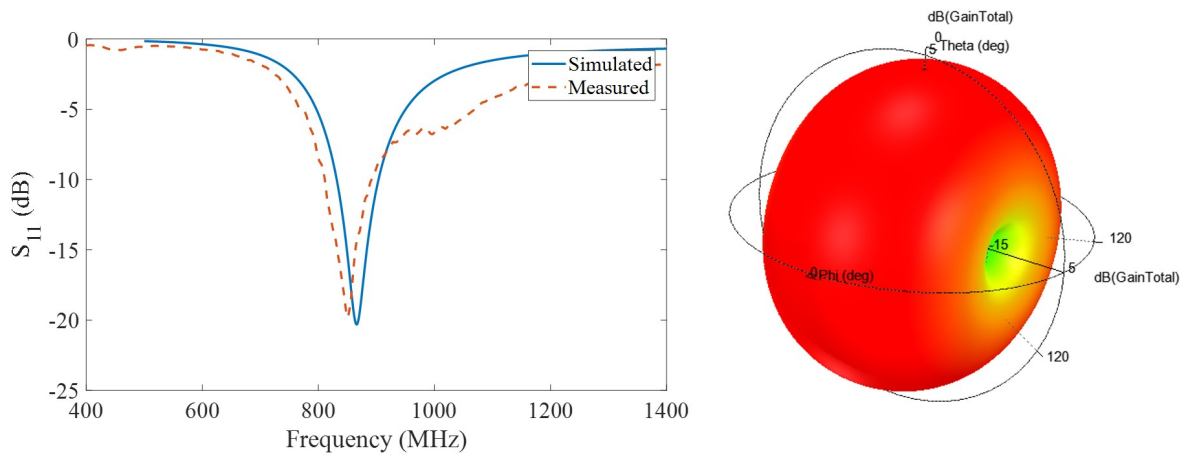


Figure 4.27: (A) Simulated and Measured frequency response of the 868 MHz antenna, (B) Simulated radiation pattern of the antenna

4.3.1.3 Hybrid Multi-Frequency Interrogator

A new custom interrogator is designed to communicate with the hybrid tags operating at a single or harmonic frequency. The basic functionality of an interrogator is to transmit and receive RF signals,

which needs to be modulated on the way-out and demodulated on the way-in. Both the modulator and demodulator are part of the RF front-end, with additional peripherals like power amplifier, LNA, filters, heterodyning mixer, etc. The block diagram of the designed interrogator with multi-frequency operation and hybrid reception is shown in Fig.4.28. The fundamental functionalities are similar to ISS interrogator explained in section B.2.3. A few changes are made to accommodate the analog sensor data reception. A SPDT switch is added at the IF PORT of the heterodyning mixer to select in the path in for digital and analog data. The communication starts with the digital data that is decoded by a microprocessor. After receiving all digital bits, the microprocessor will switch the read port towards an oscilloscope for analog data acquisition. An additional low pass filter is added for eliminating high frequency components and the final signal will have the residual DC bias, which corresponds to the in-phase component of the received signal. The change in phase or amplitude of the back-reflected signal from the tag will change the DC output of heterodyne receiver.

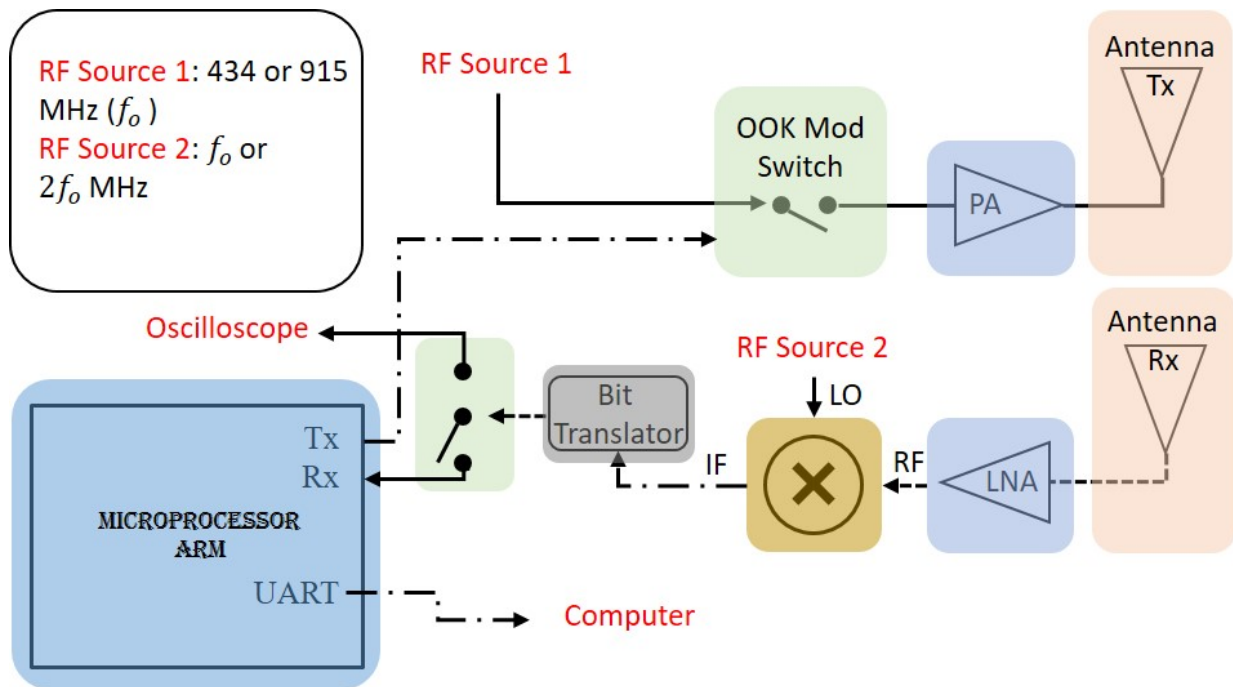


Figure 4.28: Block diagram of the hybrid multi-frequency interrogator

4.3.2 Results

4.3.2.1 Wireless Demonstration

Hybrid Single frequency RFID Tag

A wireless communication setup is created for detecting a hybrid RFID tag operating at 915 MHz. The interrogator at 915 MHz is turned on with an output power of +7 dBm, which can be received by the tag placed at 10 inches distance. The block diagram of the setup and the picture of setup is shown in Fig.4.29.

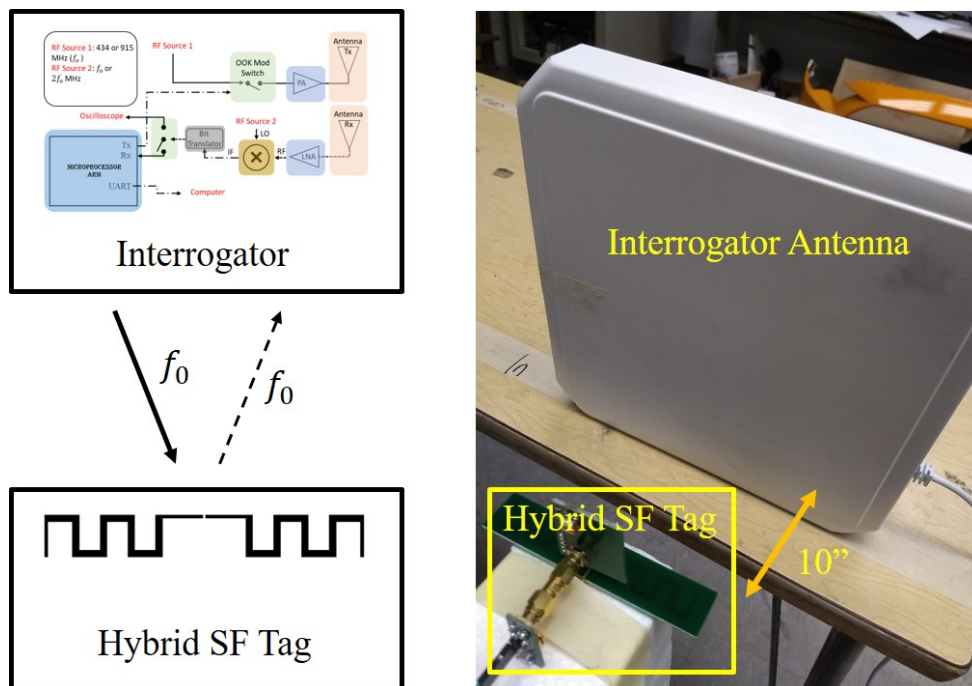


Figure 4.29: Wireless setup for hybrid single-frequency RFID communication

The transmitted signal from interrogator is received by the hybrid RFID tag, which harvests the RF energy and turn on the microcontroller. The logic inside the microcontroller decodes the commands and respond by modulating the backreflected RF signal with a digital ID, followed with the analog data packet by simply turning on the switch of the sensor integrated coupler to introduce an additional phase shift. The backreflected signal with digital ID and analog sensor data is received by the interrogator and demodulated using mixer. The output of the mixer is shown in Fig.4.30. The digital bits are clearly visible with preamble, EPC, sensor type, sensing parameter, and CRC.

The continuous wave for RAD (175 μ s) and SAD(175 μ s) can also be distinguished easily with a 15 μ s time gap in between.

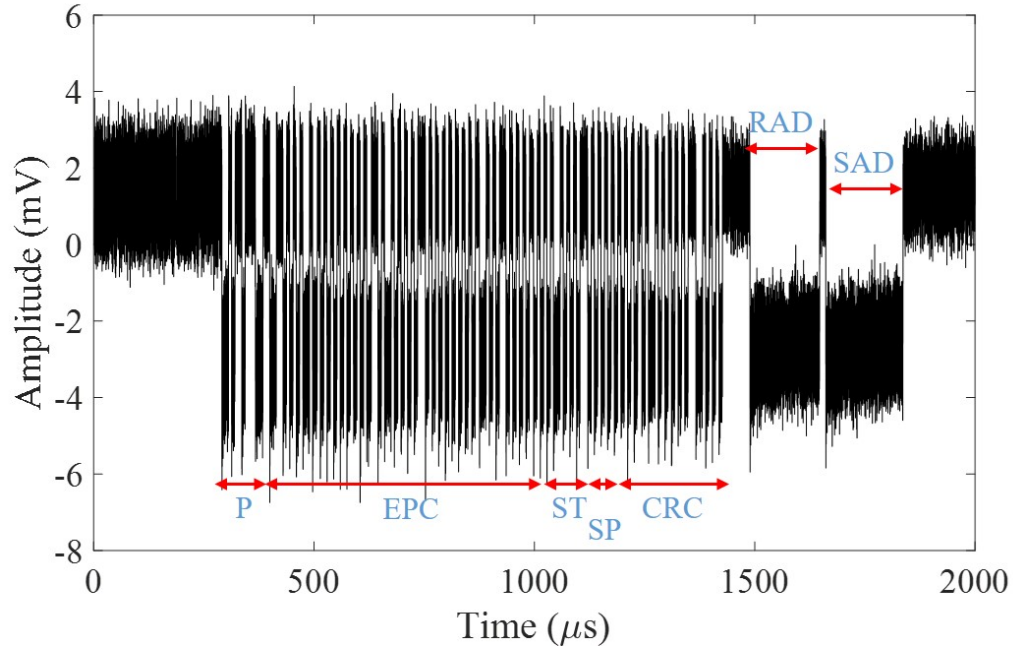


Figure 4.30: Demodulated hybrid data received at 915 MHz wirelessly from designed RFID tag

```

Enter comport number: 5
Port opened successfully!
Starting Interrogator...
Interrogator Initialized to Default:
Mode: DIGITAL,          Format to Change-> CONFIG:MODE:?
Frequency of operation: 915 MHz,    Format to Change-> CONFIG:FREQBAND:?
Type 'START' for issuing First Query @ 915 MHz

:CONFIG:MODE:HYBRID    Step 1: Change Mode
Mode: HYBRID,          Format to Change-> CONFIG:MODE:?
Type 'START' for issuing First Query @ 915 MHz

:START    Step 2: Send Start

:    Step 3: Send Acknowledgement
EPC      ST      SP      CRC
-----  -
e200a10093  01      1  0B82    Step 4: Receive and print Digital Data

```

Figure 4.31: Snapshot of the hybrid single-frequency communication with digital information

The received data contains both digital and analog information. The interrogator decoded the digital data using microprocessor and switched the receiver to oscilloscope for recording the analog

data. The digital information is sent to the computer and a snapshot of the received data is shown in Fig.4.31. While the recorded analog data is shown in Fig.4.32. A Varactor diode is connected with the coupler for imitating a capacitive sensor. An external 0V is applied across the Varactor, which represents the sensor analog data. Due to 0V as input, no change is observed in the RAD and SAD level that represents different phases of the received signal. Therefore, no capacitance change is represented by the difference of RAD's and SAD's average voltage level, which is approximately zero in this case.

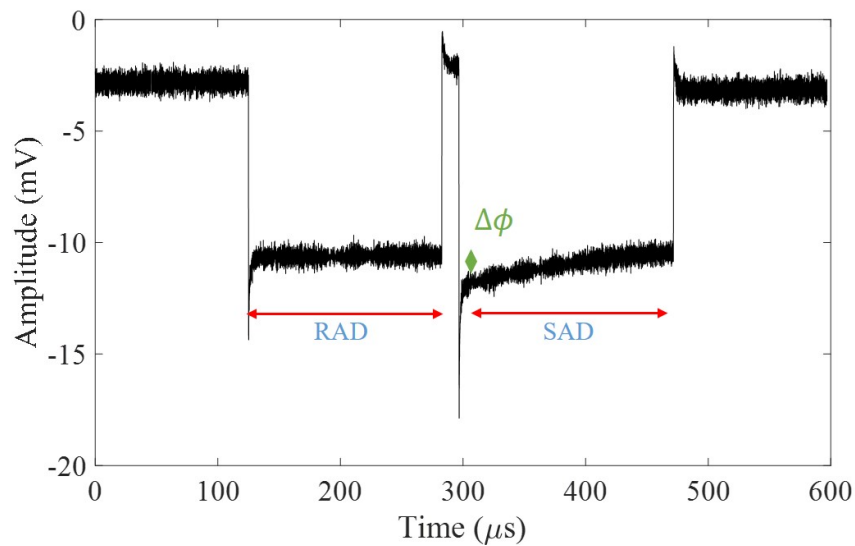


Figure 4.32: Analog sensor data recorded using oscilloscope from 915 MHz hybrid RFID tag

A second measurement is made with 1.0V applied across varactor. The received digital data is same for the same tag but the received analog data is changed due to the change in capacitance (or phase). Both analog received data with 0.0V and 1.0V input are shown in Fig.4.33. Both plots are shown together for observing the 3.3mV change in the received signal.

The explained process is repeated for a range of input voltages from 0.0V to 1.0V with a step size of 0.2V. The digital information is same for the different sensing values. The received analog data for all other four sensor values is shown in Fig.4.34.

The average voltage potential for 175μs data is calculated for both RAD and SAD. The procedure for all 6 different voltage potential is recorded and the difference in reference (RAD) and sensor

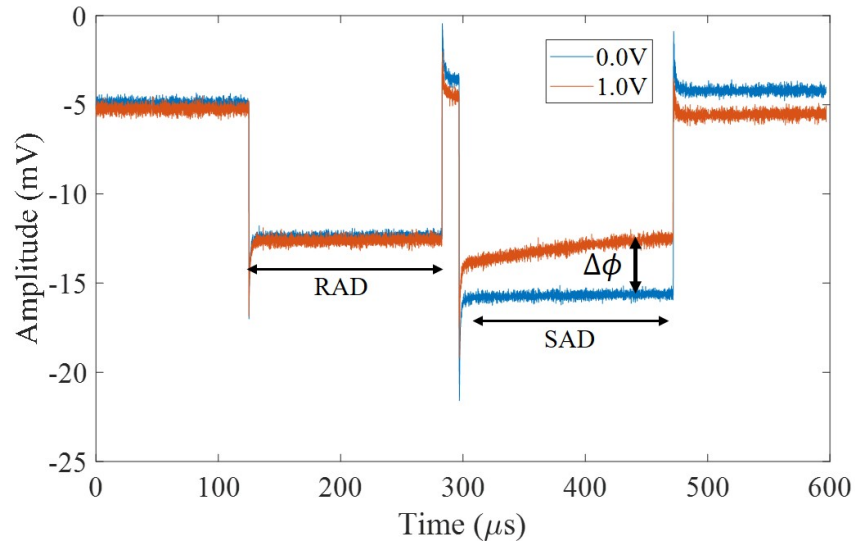


Figure 4.33: Analog sensor data recorded using oscilloscope from 915 MHz hybrid RFID tag; 0.0V input (Red) and 1.0V input (Blue)

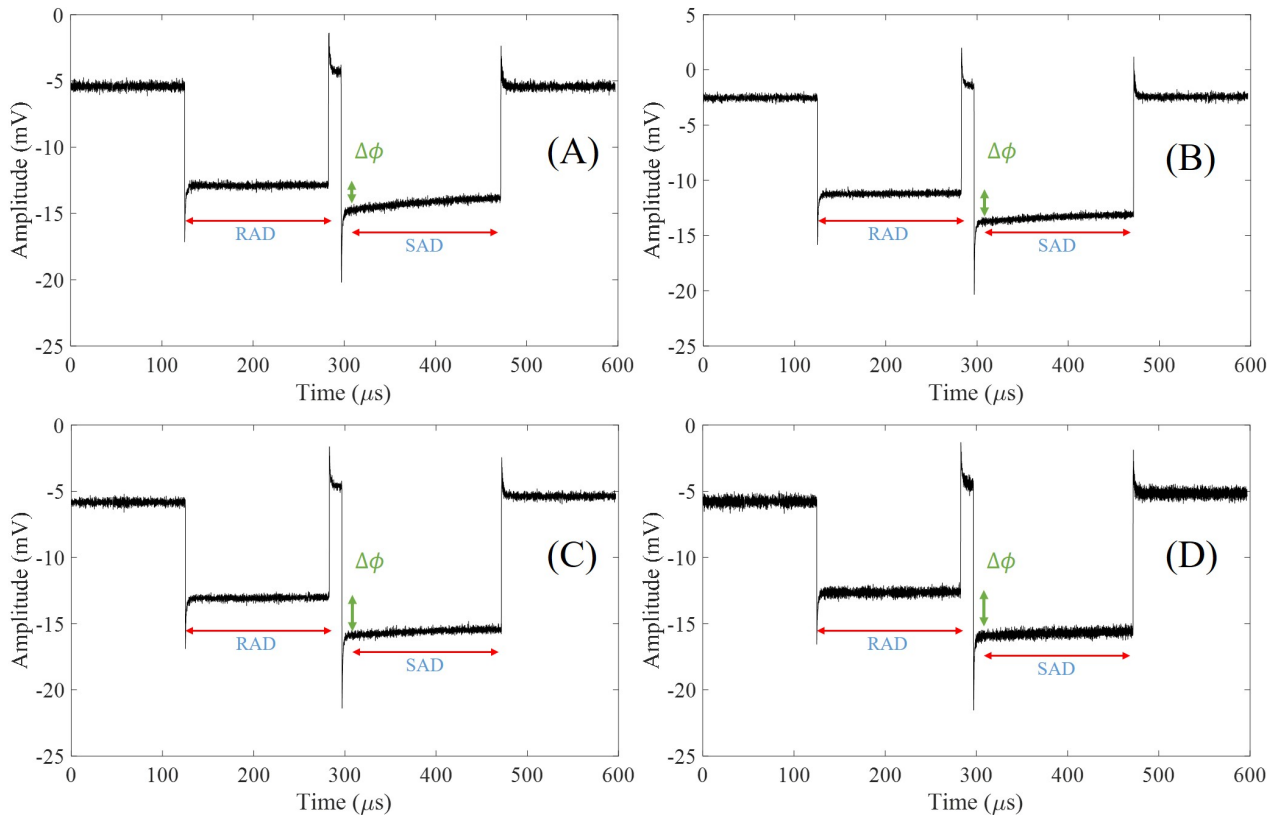


Figure 4.34: Analog sensor data recorded using oscilloscope from 915 MHz hybrid RFID tag; (A) 0.2V, (B) 0.4V, (C) 0.6V, (D) 0.8V

potential (SAD) is shown in Fig.4.35.

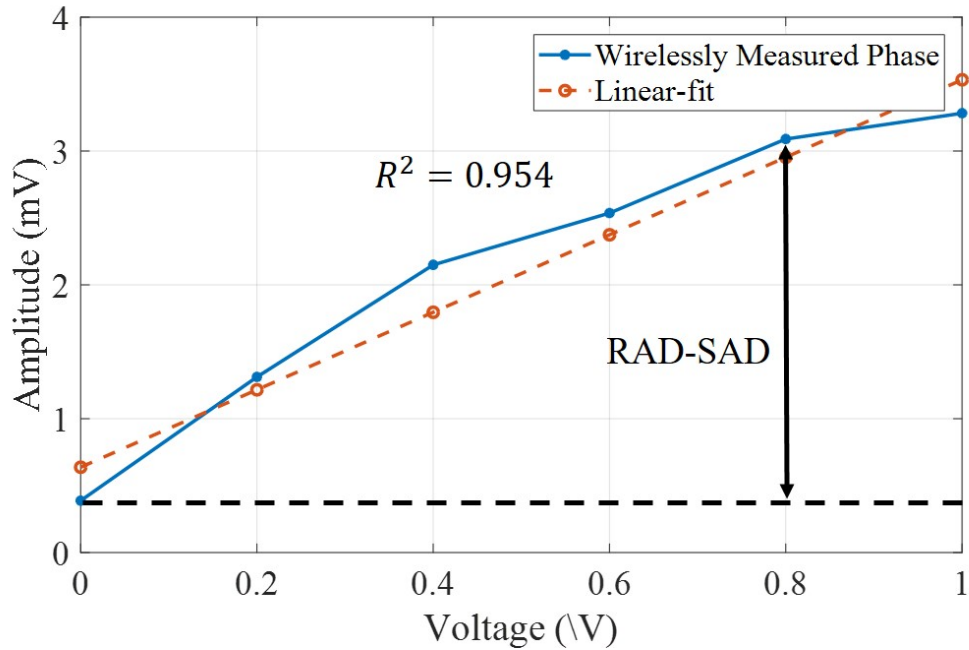


Figure 4.35: Difference in reference (RAD) and sensor (SAD) data for different sensor voltage across Varactor

A interrogator successfully decoded the 915 MHz hybrid RFID tag's data. The small change in phase due to the small voltage potential can be detected. The acquired data is linear and show good correlation with the wired acquisition using VNA.

Hybrid Harmonic RFID Tag

A wireless communication setup is created for detecting a hybrid RFID tag operating at 434 MHz for downlink and 868 MHz for uplink. The interrogator with two harmonic antenna's is turned on with 434 MHz output frequency and +7 dBm output power, which can be received by the tag placed at 10 inches distance. The block diagram and the picture of setup are shown in Fig.4.36.

The transmitted signal at 434 MHz from interrogator is received by a hybrid harmonic RFID tag, which harvests the RF energy and turn on the microcontroller. The microcontroller holds the digital logic to operate according to the received commands from the interrogator and respond by modulating the backreflected harmonic RF signal at 868 MHz with digital ID and analog sensor data. The backreflected signal with hybrid data packet is received by the interrogator and

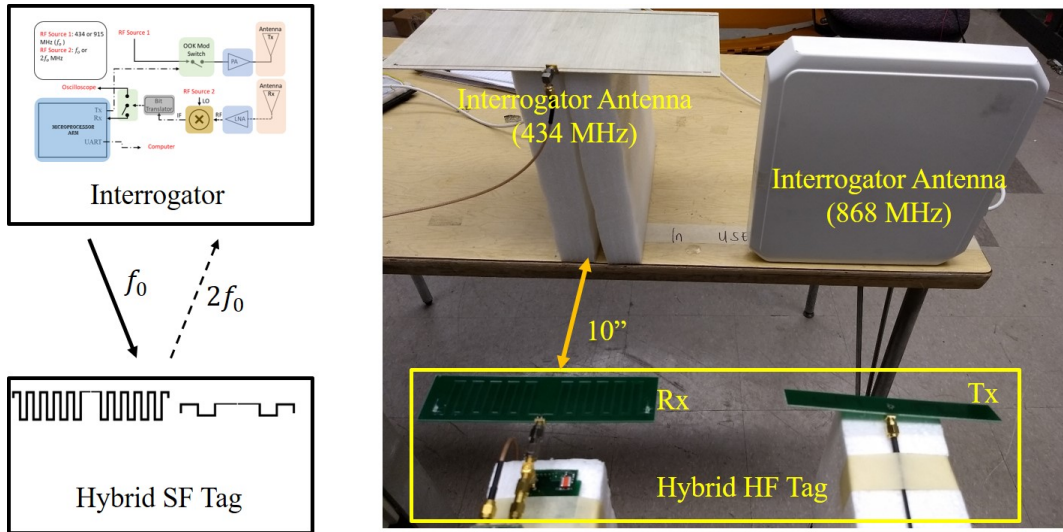


Figure 4.36: Wireless setup for hybrid harmonic-frequency RFID communication

demodulated using an RF mixer. The output of the mixer is shown in Fig.4.37. The digital bits are distinctly visible with preamble, EPC, sensor type, sensing parameter, and CRC. The continuous wave for RAD (175 μ s) and SAD (175 μ s) is also successfully received with a 15 μ s time gap in between.

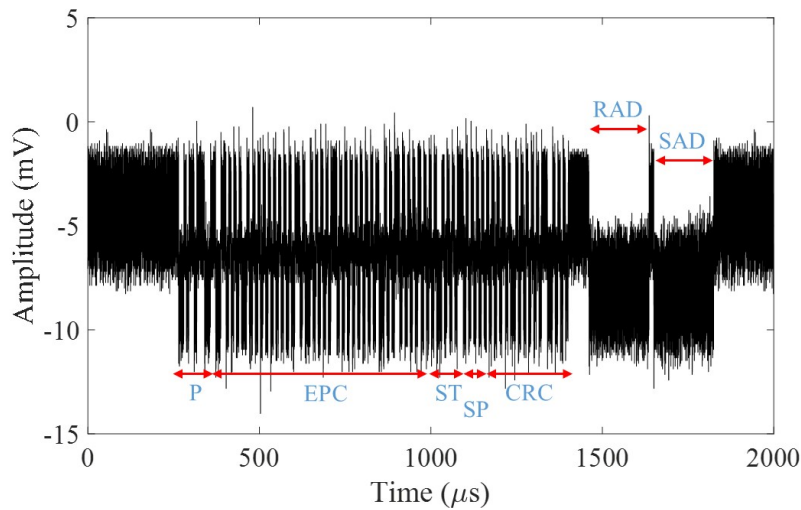


Figure 4.37: Demodulated hybrid data received at 868 MHz wirelessly from designed RFID tag

The received data contains both digital and analog information. The interrogator decoded the digital data using microprocessor and switched the receiver to the oscilloscope for recording the analog data. The digital information is sent to the computer and a snapshot of the received data is

shown in Fig.4.38. While the recorded analog data is shown in Fig.4.39.

```

Enter comport number: 5
Port opened successfully!
Starting Interrogator...
Interrogator Initialized to Default:
Mode: DIGITAL,          Format to Change-> CONFIG:MODE:?
Frequency of operation: 915 MHz,    Format to Change-> CONFIG:FREQBAND:?
Type 'START' for issuing First Query @ 915 MHz

:CONFIG:MODE:HYBRID      Step 1: Change Mode
Mode: HYBRID,          Format to Change-> CONFIG:MODE:?
Type 'START' for issuing First Query @ 915 MHz

:CONFIG:FREQBAND:433M   Step 2: Change Frequency Band
Frequency of operation: 433 MHz,    Format to Change-> CONFIG:FREQBAND:?
Type 'START' for issuing First Query @ 433 MHz

:START                  Step 3: Send Start

:                        Step 4: Send Acknowledgement
EPC      ST   SP   CRC
-----
e200a10094 01   1   8e+12      Step 5: Receive and print Digital Data

```

Figure 4.38: Snapshot of the hybrid harmonic-frequency communication with digital information

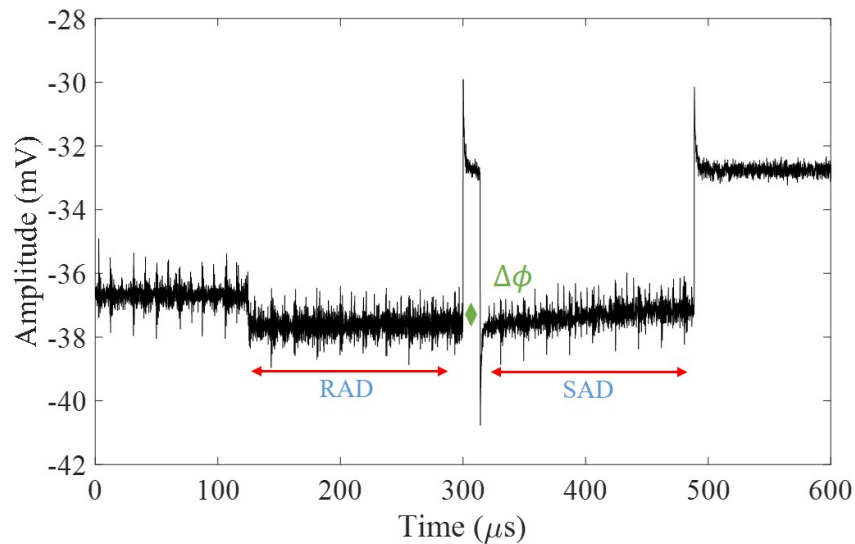


Figure 4.39: Analog sensor data at harmonic signal recorded using oscilloscope

A Varactor diode is connected to the hybrid coupler as a capacitive sensor. An external 0V is applied across the Varactor, which represents the sensor analog data. Due to 0V as input, a very small change is observed in the RAD and SAD level that represents different phases of the received signal. Therefore, minimal capacitance change is represented by the difference of RAD's and SAD's average voltage level, which is approximately zero in this case.

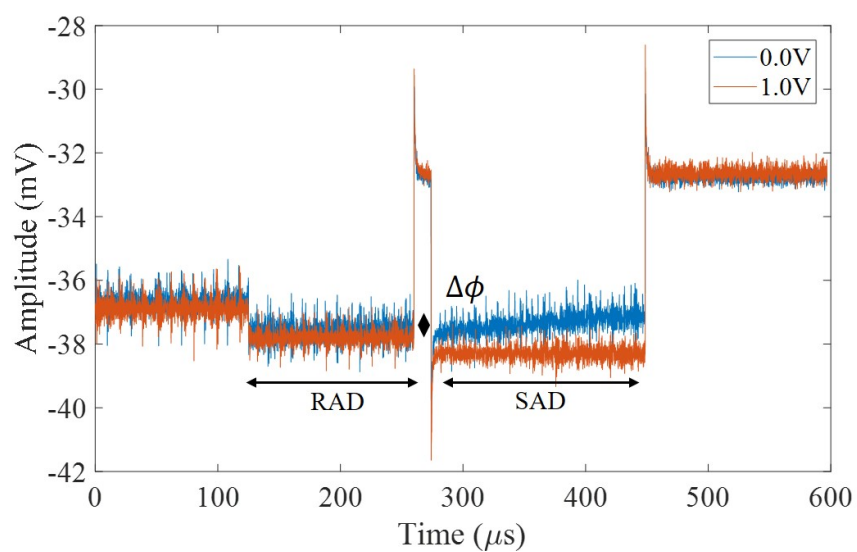


Figure 4.40: Analog sensor data at harmonic signal recorded using oscilloscope; 0.0V input (Red and 1.0V input (Blue))

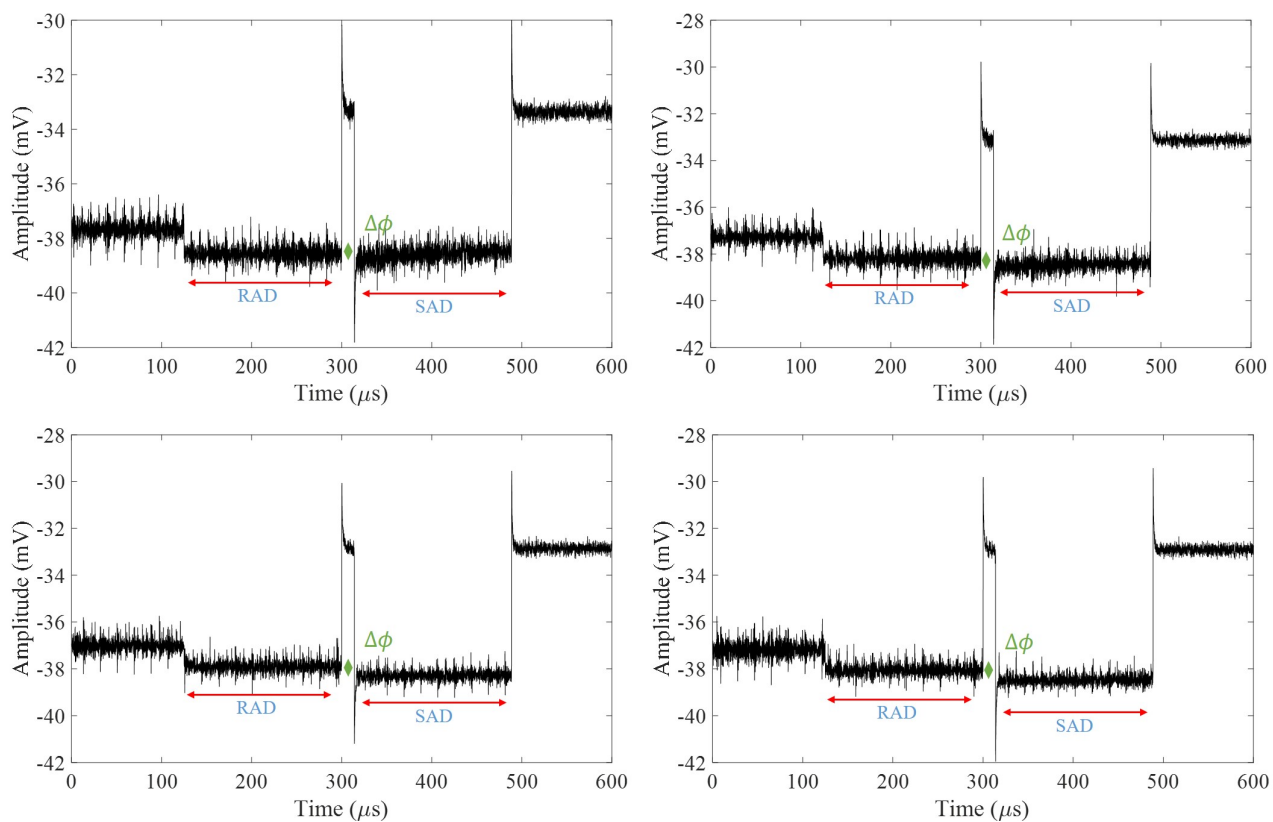


Figure 4.41: Analog sensor data recorded at 868 MHz using oscilloscope; (A) 0.2V, (B) 0.4V, (C) 0.6V, (D) 0.8V

A second measurement is made with 1.0V applied across Varactor. The received digital data is same for the same tag but the received analog data is changed due to the change in capacitance (or phase). Both analog received data with 0.0V and 1.0V input are shown in Fig.4.40. Both plots are shown together for observing the change in the received signal.

The explained process is repeated for a range of input voltages from 0.0V to 1.0V with a step size of 0.2V. The digital information is same for the different sensing values. The received analog data for all other four sensor values is shown in Fig.4.41.

The average voltage potential for 175μs data is calculated for both RAD and SAD. The difference in RAD and SAD of acquired data is shown in Fig.4.42.

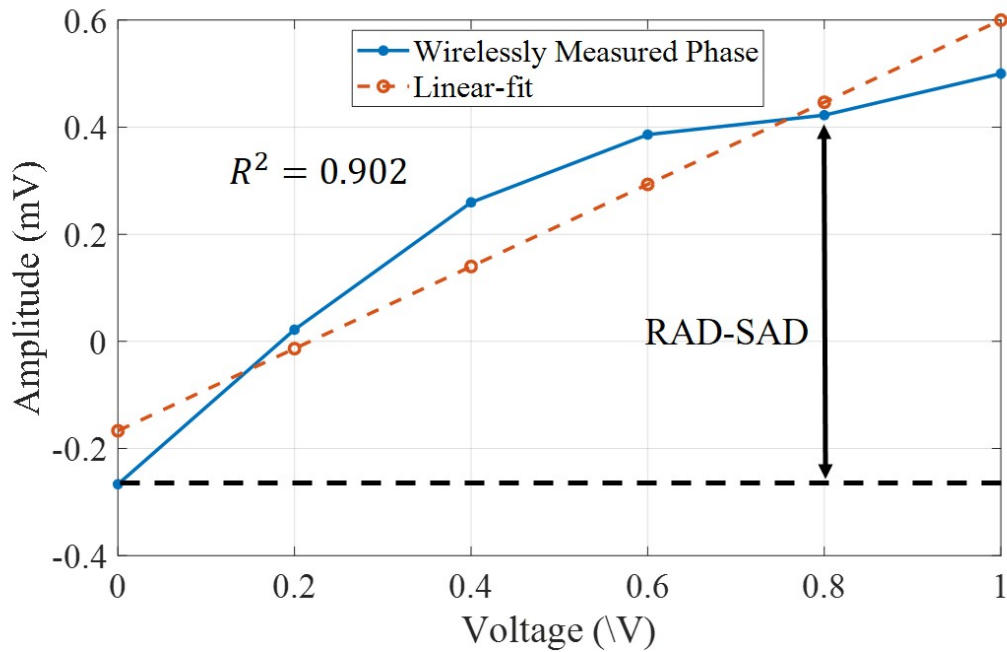


Figure 4.42: Difference in RAD and SAD of 868 MHz signal for different sensor voltage across varactor

A interrogator successfully decoded the harmonic-frequency tag's data. The small change in phase due to the small voltage potential can be detected.

4.4 Summary

The hybrid RFID system is implemented to reduce power requirement for battery-free sensing. A hybrid coupler based sensing mechanism is demonstrated that can shift the phase of the RF signal according to the reactance of the sensor. An additively manufactured capacitive pressure sensor is designed and used to show the capabilities of the power efficient phase modulation system and wirelessly transmit the data. The elimination of ADC using hybrid coupler based solution is optimal for power efficiency, but introduce other problems like; incompatibility with multiple tag communication, sensitive to movement, etc. Therefore, the analog data is combined with a digital data frame to allow multiple tags detection and data acquisition. The hybrid data frame requires less power than its ADC based alternatives and also work with single or harmonic frequency operation mode. The hybrid harmonic has better SNR than its single frequency counterpart, which allows reliable phase extraction. Moreover, the differential reading between RAD and SAD makes the data acquisition more robust against noise prone environment and multiple path reflections.

CHAPTER 5

ACTIVE SENSOR INTEGRATION WITH ADC-FREE RFID TAG FOR ULTRA-LOW POWER OPERATION

5.1 Introduction

Lack of maintenance and proper protection were found to be the major cause of mechanical failure. In order to continue a safe and reliable operation, some proactive measures are required that can detect the failure before it occurs and sound an alarm for maintenance. Ultrasonic technique is one such method for evaluating the mechanical properties of materials by analyzing the vibration response.

Researchers are developing the vibration sensing technology for years that sets a standard for measurement techniques that are best performed in lab settings or field environment. The ultrasonic pulser-receiver systems are very popular for detecting time-of-flight and tracking amplitude changes of received signal, which has traveled through the material under test. The vibrations are actuated and detected by mounting a transducer, which change or acquires the lateral displacement, velocity, and acceleration [141, 142]. It include elements like PZT, PVDF, etc., which can be considered active sensors because it requires an external energy source for generating signals.

In NDE, the acoustic system plays a vital role for evaluating various materials from metals to composites and polymers. The acoustic equipment's used for NDE are very standard table-top, bulky, and high power systems, which is easy to handle only in lab conditions and ideal for precise measurements. On the other hand, the acoustic system used for SHM purpose has a very different application area. The SHM requires both bulky equipment's for long range and deep penetration applications and a small IoT based system for monitoring tiny cracks, material loss, permeation, etc. The current SHM system in place is required to avoid any potential down time by acquiring continuous data and performing predictive maintenance.

Our focus for this research is specifically on small IoT based platforms. The small sensing

devices for SHM in large facilities like refineries and chemical plants are gaining momentum due to their 24x7 monitoring capabilities while providing more data around the plant for multiple systems simultaneously. The profound application and large market size has pushed a few key companies like Texas Instruments to make specially designed integrated circuits for acoustic pulser and receivers to combine it with the IoT based communication platform to acquire real-time data [143, 144]. However, these current IoT based maintenance systems in place are battery powered and consume more than $4mW$ of power due to high speed ADC, which also requires additional maintenance and has a very limited life cycle of a few years.

In this work, we propose a battery-free RFID tag based platform for actuating and detecting acoustic signals without any ADC requirement. The primary advantage of such system is its multidecade life time with no maintenance. Moreover, the costs for battery-free RFID tags are significantly lower than battery-based counter parts. The lower sensor tag cost pave an economical path to deployment at large scale and collect high resolution data around any facility.

The design of the proposed solution is discussed first with the active-sensing architecture and its main components and finally a wireless demonstration is presented to show a working prototype.

5.2 Design

The active sensors like PZT's are conventionally used to actuate and detect acoustic waves. The PZT transducer simply needs to be connected to a continuous wave or pulse source for actuation and either an ADC or an oscilloscope for detection. In cases when the received signal strength is too low for the oscilloscope, an amplifier can be used to boost the signal. For battery-free RFID tags, a waveform source for actuation and an amplifier for detection are not among the viable options. Therefore, a new technique is required to feed and read the transducer while reducing all power requirements. The architecture of proposed battery-free sensor tag with integrated PZT is explained below.

5.2.1 Active Sensing Architecture

The fundamental architecture for the PZT integration is inspired from the hybrid harmonic-frequency RFID tag, explained in the previous chapter. The primary reason for selecting the harmonic frequency is due to its superior SNR performance and on-board nonlinear frequency mixing element (NLTL). The basic functionality of the tag remains the same, where it receives a continuous wave at 434 MHz and turn on the microcontroller. The microcontroller reflects back the digital ID by switching the modulator with a GPIO pin. Similarly, another GPIO is used to generate a square pulse of $2.5\mu s$, which is connected to a PZT. The PZT actuates according to the input pulse and couples the mechanical vibrations into the attached steel material. The acoustic waves travel down in the material and can be picked-up using a second PZT. The received signal at PZT is mixed with the wirelessly received 434 MHz RF signal using NLTL, which also generates the 2nd harmonic signal at 868 MHz. The output of NLTL will have the second harmonic signal with modulated PZT data that can be transmitted back to the interrogator for demodulation and detection. The schematic of the designed active sensor integrated hybrid harmonic RFID tag is shown in Fig.5.1. The data frame for acoustic actuation and detection with RFID communication is shown in Table.5.1.

Table 5.1: Data frame format for Digital ID with Acoustic Transducer Data Reply

P	EPC	ST	SP	CRC-16	AP	DP
---	-----	----	----	--------	----	----

where AP is actuation pulse and DP is detected pulse. The digital part in the hybrid acoustic frame is same as explained in hybrid harmonic RFID tag.

5.2.2 Integrating Acoustic Actuation Transducer

The battery-free RFID tag do not have a specific waveform generator for acoustic actuation, therefore, a microcontroller is used to generate a short pulse of $1.8V$ that can have a minimum width of $2.5\mu s$ or $400kHz$. Generating a short pulse is not a power hungry operation, the microcontroller uses the same GPIOs to generate the backreflected signal at a similar data rate. A PZT (Piezo

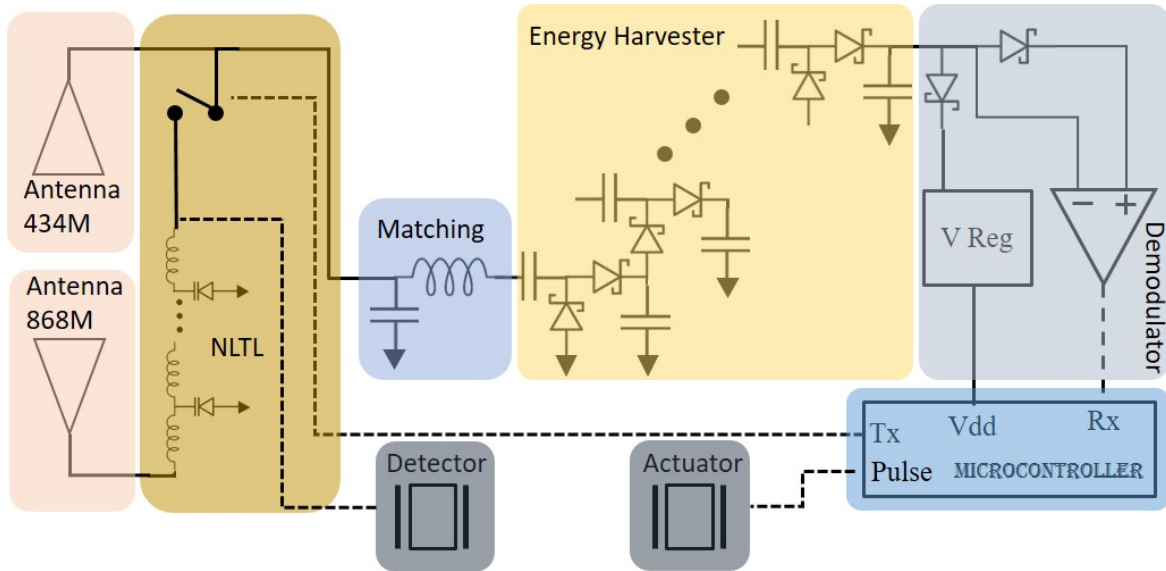


Figure 5.1: Schematic of active sensor integrated hybrid harmonic RFID tag

Ceramic Plate 7x8x0.2mm) from Steminc were used to test the acoustic generation in steel plate. The square pulse profile generated by microcontroller is shown in Fig.5.2B. The signal is launched into a steel sample plate and detected by a second PZT placed 70mm away, the setup is shown in Fig.5.2A. The signal received by second PZT is recorded using an oscilloscope, shown in Fig.5.2B.

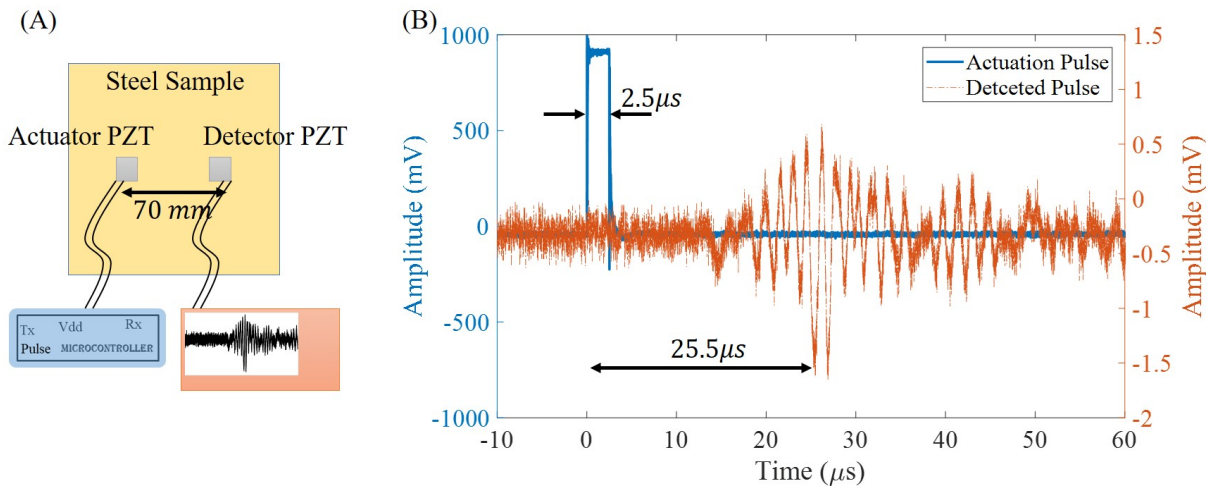


Figure 5.2: (A) Acoustic actuation and detection wired setup, (B) PZT actuation pulse signal generated by microcontroller and detected signal profile with averaging

The microcontroller was used as a pulse source for PZT and the actuated pulse successfully coupled to the steel plate. The PZT will only be actuated when the RFID tag responds to the

interrogator with a digital ID, therefore each pulse actuation and detection can be specified to a predefined target. For the current wired experiment, the observed time of flight to travel 70mm in steel is 25.5 μ s.

5.2.3 Integrating Acoustic Detection Transducer

The wired detection shown in the previous section for testing purpose needs to be made wireless as well. However, the battery-free RFID tag cannot afford any high data acquisition rate ADC. Therefore, the acoustic signal needs to be analog modulated with backreflected signal for decoding at the interrogator's end. The signal generated by the PZT has very low strength, so biasing a Varactor diode connected to a hybrid coupler will not be effective due to the low sensitivity. An alternative method for modulating low power signals is using a mixing component, which is present on-board in the form of NLTL. The PZT is connected at the input port of the NLTL to the 434 MHz receiving antenna, as shown in Fig.5.3.

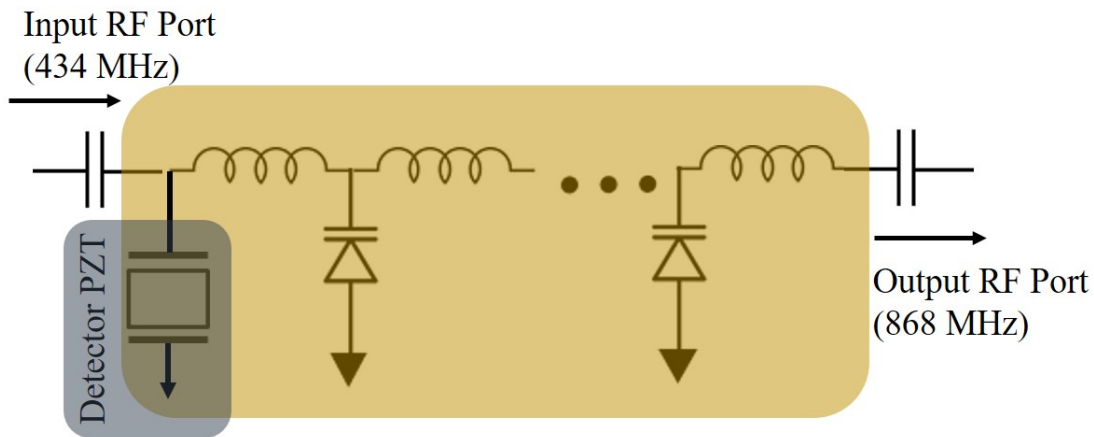


Figure 5.3: Schematic of the PZT integration with non-linear transmission line

A wired setup is created for testing the analog modulation of PZT signal on the harmonic signal generated by the NLTL. The PZT transducer integration is tested with two types of actuation signals; continuous wave and pulses.

5.2.3.1 Acoustic continuous wave detection

A continuous wave of 200 kHz with 1.8 Vpp amplitude is applied at the actuation transducer, which travels through the steel plate and can be detected at the second receiving transducer. The block diagram of the test setup is shown in Fig.5.4A. The acoustic signal received by the PZT is modulated on the harmonic signal, which can be transmitted back to the interrogator. The analog modulation of the harmonic signal is shown in Fig.5.4B. The modulated side bands are clearly visible at 200 kHz offset, with very low mixing losses.

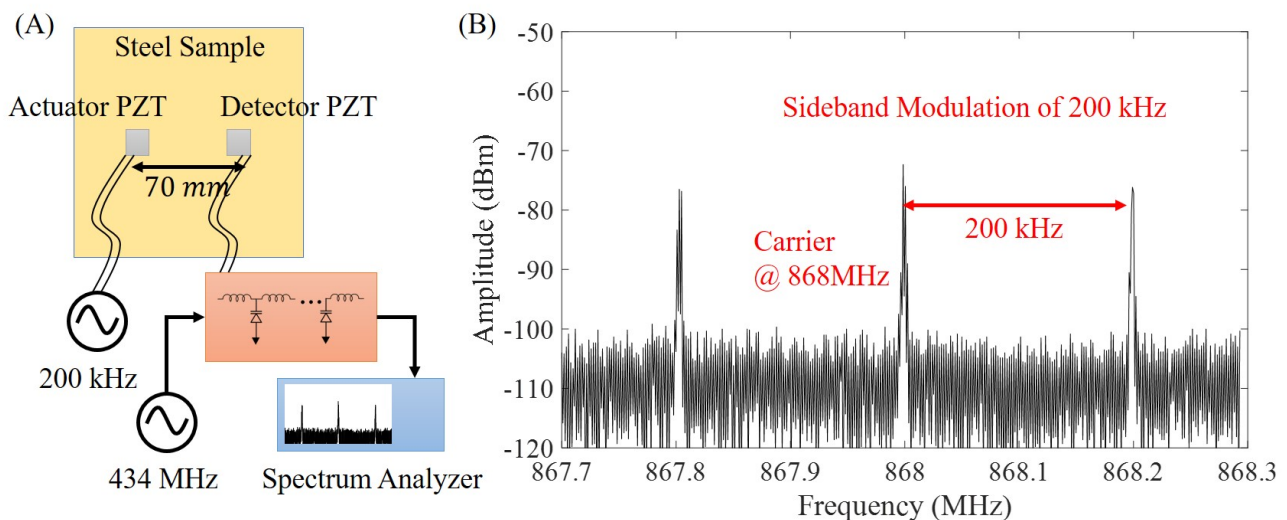


Figure 5.4: (A) Test setup to check the analog modulation capabilities of RFID tag, (B) Harmonic output of the NLTL is modulated with 200 kHz acoustic signal detected by PZT

5.2.3.2 Acoustic pulse detection

The continuous wave detection setup was created for sanity check, but it does not represent the practical scenario for acoustic-based NDE and SHM. The practical applications use pulse for evaluating materials and structures. Therefore, a second test setup is created for modulating and detecting the pulse signal. A $2.5\mu\text{s}$ wide pulse of 1.8 Vpp is generated using a waveform generator that is picked up by the receiving PZT and modulated on the 868 MHz harmonic signal. The harmonic signal with acoustic signal pulses as side bands cannot be captured using a spectrum analyzer, therefore, an additional setup for demodulation using RF mixer is used. The designed

test setup is shown in Fig.5.5A. The output of the NLTL is amplified by 25 dB and fed into the mixer for demodulation, with an external RF source of 868 MHz. The demodulated acoustic pulse is shown in Fig.5.5B with same ToF as previously measured by the oscilloscope.

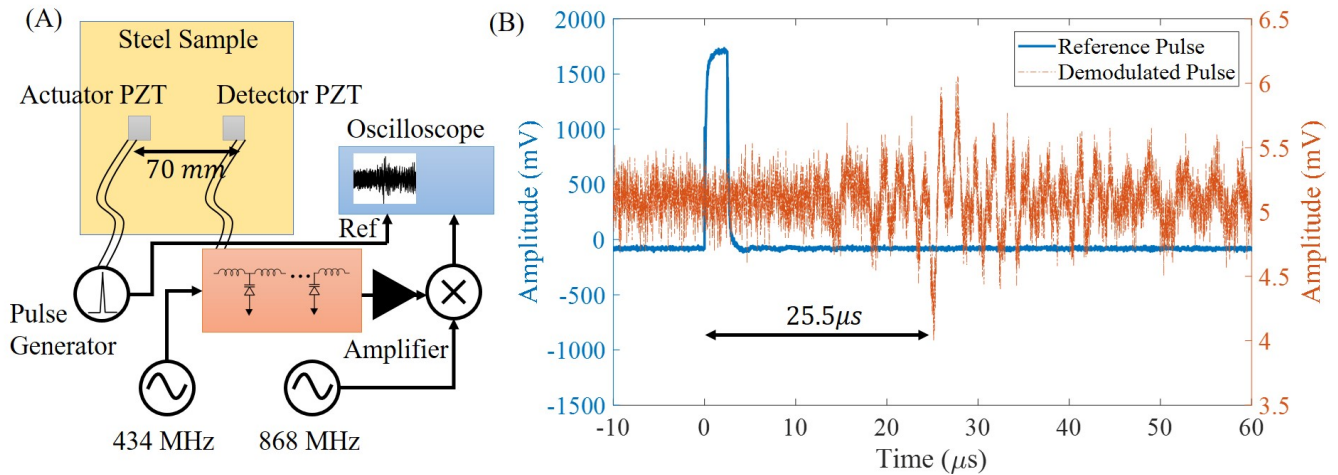


Figure 5.5: (A) Test setup to check the acoustic pulse modulation capabilities of RFID tag, (B) Demodulated acoustic signal detected by PZT

The NLTL shows the capabilities of detecting small acoustic signals and modulating back on the harmonic signals. The next step is to combine the acoustic actuation and detection setup with the wireless antennas for demonstrating a complete battery-free solution for the first time.

5.3 Results

5.3.1 Wireless Acoustic Actuation and Detection Demonstration

The wireless RFID tag as shown in Fig.5.1 is assembled with necessary tag software changes to accommodate acoustic pulse generation and data transmission. The wireless setup with battery-free RFID tag, sample steel plate and interrogator is shown in Fig.5.6.

5.3.1.1 Detection of Acoustic Time-of-Flight in Steel

The interrogator is started at 434 MHz output signal with an amplitude of +7 dBm. The 434 MHz signal wirelessly charge the battery-free RFID tag in field-of-view, which can also respond to

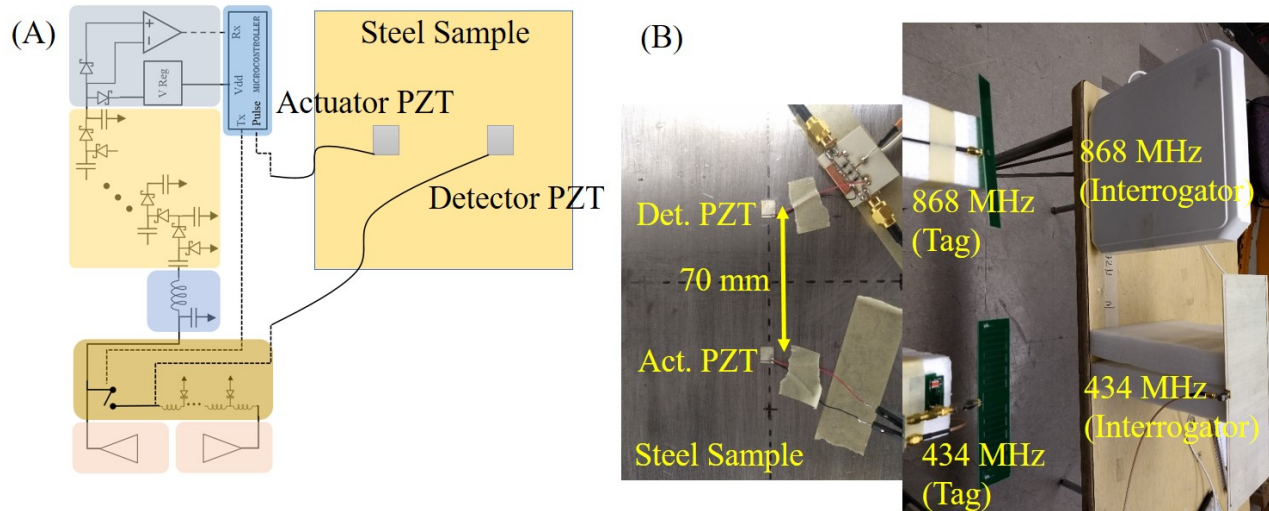


Figure 5.6: (A) Wireless hybrid harmonic RFID tag with integrated PZT setup for acoustic actuation and detection, (B) Picture of the practical setup

interrogator's commands accordingly. After the tag gets acknowledged, it backreflects the digital ID information as we have seen previously for hybrid harmonic-frequency communication. Moreover, for the PZT transducers, the microcontroller generates an actuation pulse of $2.5\mu s$ at the end of digital ID transmission and switch on the backreflection for additional $175\mu s$ for the PZT to receive and modulate the acoustic signal. The interrogator's 868 MHz harmonic antenna receives the harmonic modulated signal with digital ID and analog acoustic data. The digital information is extracted by the interrogator's microprocessor and acoustic data is directed towards the oscilloscope as shown in the previous chapter. The wirelessly received and demodulated acoustic signal is shown in Fig.5.7.

The wirelessly measured time-of-flight for acoustic signal is $25.5\mu s$ as measured before in the wired configuration. The detection results also proves the viability of such a system that can operate without battery and able to perform such complex tasks of detecting vibrations.

5.4 Summary

The acoustic actuation and detection demonstrates the capability of battery-free hybrid harmonic RFID tag and multifrequency interrogation system. The PZT integrated hybrid RFID tag can

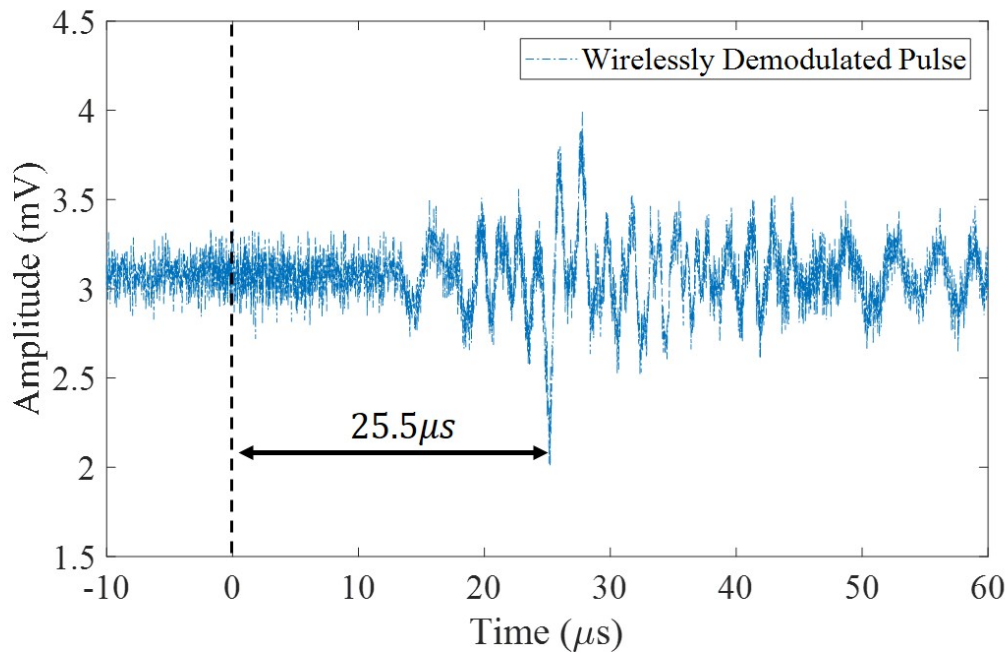


Figure 5.7: Wireless acquired and demodulated harmonic signal for acoustic signal

generate the actuation pulse without any heavy power requirements. The receiving PZT and modulating NLTL are very sensitive towards very small amplitude of vibrations. The 434 MHz and 868 MHz operation allows real-time battery free communication and avails enough bandwidth for detecting acoustic pulses. Additionally, the harmonic operation offers a high SNR that increases the reliability of the communication system.

CHAPTER 6

CONCLUSION AND FUTURE WORK

6.1 Summary

The primary challenges of current NDE and SHM methods are identified, which includes lower sensitivity towards dielectric evaluation, limited range due to RF clutter, lack of versatility in sensor integration, scalability and maintenance issues for monitoring applications. Each challenge is discussed in detail for various applications with multiple available techniques. Alternative solutions are proposed to overcome each challenge by using (a) wireless high-Q resonator sensing for dielectric evaluation, (b) battery-free RFID system for eliminating maintenance requirements and harmonic communication for enhanced range, (c) hybrid data packet for sensor versatility while achieving power efficiency and eliminating ADC.

The high-Q resonator is achieved by wireless coupling in near-field. The capacitive sensor in LC resonator is an unshielded parallel plate configuration that change its capacitance according to the near by dielectric properties. The designed probe was tested on both composite and polymer samples that detected surface and subsurface defects at sub-mm resolution. A 1×4 array probe is designed with the same fundamentals concept to resonate at 4 different frequencies for simultaneous actuation and data read.

A harmonic-based RFID system is designed to extend the communication range of conventional RFID by eliminating the RF clutter/self-jamming issues. The harmonic system provides better SNR and opens a window of opportunity to make more sensitive RFID ICs.

A pressure sensor is designed using additive manufacturing techniques to demonstrate the power efficient wireless sensing capability. The power efficient analog sensing is merged with digital ID for eliminating high power requirements. The analog data is successfully extracted from the hybrid data packet with good linearity.

Ultrasonic methods are very popular and effective as NDE and SHM technologies. But it has

never been considered as a power efficient technique. This work demonstrated a PZT actuation using a battery-free RFID tag and acoustic detection without the use of an ADC by wirelessly transmitting the information to the interrogator. The hybrid harmonic RFID tag with digital ID and analog PZT data has opened new possibilities for embedded sensing.

The wireless sensing for both NDE and SHM can take on the current challenges. The hybrid harmonic RFID with passive and active sensor integration can all together solve the excessive maintenance problem of battery-based IoT infrastructure. Moreover, the lower cost of a battery-free system allows large-scale deployment for high-resolution data acquisition to allow AI based predictive maintenance.

6.2 Future Work

In this thesis, various novel sensing and acquisition concepts have been presented that can be extended further for increasing the technology readiness level. The key areas that require focus are (a) imaging using an array, (b) miniaturization, and (c) ultrasonic material characterization.

6.2.1 Imaging using an array

A novel concept of resonant array design is shown, where all elements can be simultaneously excited and recorded. This work shows the response of array probe, but lacks the imaging results. Therefore, a faster imaging scan using the designed array is the logical next step. The commercially available systems like Eddyfi Ectane can be used for actuation and detection as it has an inbuilt capability of exciting at multiple frequencies at the same time.

6.2.2 Miniaturization

The battery-free RFID sensing technology using hybrid data packet is fundamentally power efficient and range enhancing. However, the current implementation using distributed components is big and limits its application. The miniaturization can be started with antennas, which takes most of the area. Antennas can also be printed on flexible substrate for easy handling, embedding process, and

light weight. Second, the energy harvester and microcontroller section can be significantly reduced using a more efficient single chip RF harvester and low pin count, extremely low power logic controller. Overall reduction in tag size and component count will also reduce power requirement and make the hybrid RFID tag more sensitive.

Miniaturization of the interrogator can also help with the portability of the whole system. Integrated RF sources, super-heterodyne mixing, and onboard high precision ADC can take this technology to a whole new level.

6.2.3 Ultrasonic Material Characterization

The battery-free technology for wireless actuation and detection of ultrasonic signals via steel has a lot of potential for industrial and academic applications. The time-of-flight data can be used to calculate the velocity of an ultrasonic wave through the medium, which has a relation with mechanical properties like young's modulus and density. Moreover, the recovered pulse also holds the harmonic information and can be extended towards non-linear ultrasonic.

APPENDICES

APPENDIX A

AN RF BACKSCATTERER SYSTEM FOR REAL-TIME MULTI-SENSING APPLICATIONS

A.1 Introduction

Both amplitude and phase modulation techniques are affected by noise in the propagation environment. Furthermore, in case of direct phase modulation of the sensor information, the distance between the tag and the interrogator should be calibrated in order to avoid the ambiguity towards the change in received signal strength. The best suited energy efficient technique for analog modulation with higher immunity to noise is the frequency modulation technique. In literature, only one work has been demonstrated using the analog frequency modulation for representing RFID sensor data [145]. In this work, a Colpitts oscillator is used to generate different single tone low frequency signals that are modulated onto the backscattered signal based on the change in capacitance of the resonator. Additionally, the work shows that the rectification circuit using two zero-bias Schottky diodes was able to generate enough DC power to drive a 150 kHz oscillator with a received power of -22 dBm, whereas, the state-of-the-art CMOS based rectifiers requires at least 10 stages of rectification to generate DC power ($10 \mu\text{W}$) from -16 dBm received power [146]. Furthermore, a linear relationship is shown between RF power in log scale and output DC voltage in linear scale but the relationship stands valid only in log-log scale [147]. Hence, there is a need for developing an efficient high-performing passive RFID multi-sensing system with improved read range for IoT based sensing platforms.

In this chapter, a passive wireless multisensing system is presented with a power efficient analog frequency modulation scheme for long-range real-time communication. The proposed design exploits the available 300 kHz bandwidth of a single UHF RFID channel to modulate the multiple sensing information for efficiently transmitting the sensor data, eliminating the need for power hungry analog-to-digital conversion. The query signal from the interrogator activates the

tag and the sensor information is backscattered as a function of frequency. As an example, a multisensing tag with integrated temperature and luminescence sensors are shown with a read range of 10 feet and a sensitivity of -6 dBm. Additionally, a study for integrating the digital ID along with the analog sensor information is presented, in which the digital identification bits and analog sensor information are confluenced into a single hybrid data packet. The presented system is compatible for communicating multiple sensor information passively over a long range for IoT based applications.

A.2 Principle of Operation

The passive multisensor system consists of a custom designed UHF RFID interrogator and a multisensor tag. The communication between the reader and the multisensor tag is initiated by the interrogator by sending a continuous single frequency RF query signal within the range of 902-928 MHz. The multisensing tag consists of four units, a receiving antenna, a rectifying unit, a multisensing module with an oscillator, and a modulation unit. The multisensor tag antenna receives the RF query signal and feeds it to the rectifier through a matching circuitry that generates the required DC bias to activate the frequency oscillator.

The oscillator generates specific single tone frequency signals to represent each of the sensing parameters (for example, temperature, luminescence, humidity, etc) and a switch is used to select between different sensors with a specific periodicity. A low frequency source or an oscillator is used to generate a unique low frequency signal within a limited RFID channel bandwidth, corresponding to each sensing parameter value for a single sensor element. A number of sensors can be integrated to the same RF tag based on the total available bandwidth. Two example sensors are integrated with the proposed platform to demonstrate a test prototype. Two sensors, a temperature sensor and a light sensor, the first sensor; temperature (-25°C to +25°C) is assigned a bandwidth of 25 kHz within the frequency range of 75-100 kHz, with every 0.5 kHz representing a degree in temperature change. The second sensor, luminescence (0 fc to 20 fc) is assigned a similar 25 kHz bandwidth within the frequency range of 125-150 kHz. The available single channel bandwidth for UHF RFID

communication is 300 kHz, and with an example bandwidth requirement of 25 kHz per sensor, up to 6 different sensors can be integrated with the RF tag simultaneously. The low frequency signal generated by the oscillator is modulated on to a high frequency carrier backscattered by the tag. The backscattering modulation is performed using a MOSFET switch and the interrogator receives the modulated back-scattered signal and demodulates the information to extract the sensing data. Now, another switch is required to select one sensor at a time as the sensor information is transmitted sequentially. The period of sensor switching is fixed at 6 kHz ($\sim 160 \mu s$). The received signal at the interrogator will contain the sensor information from the first sensor within the first time period, followed by the second sensor within the second period, and the sequence repeats periodically. The schematic of the designed tag with multisensing module, modulator, tag antenna is shown in Fig.A.1.

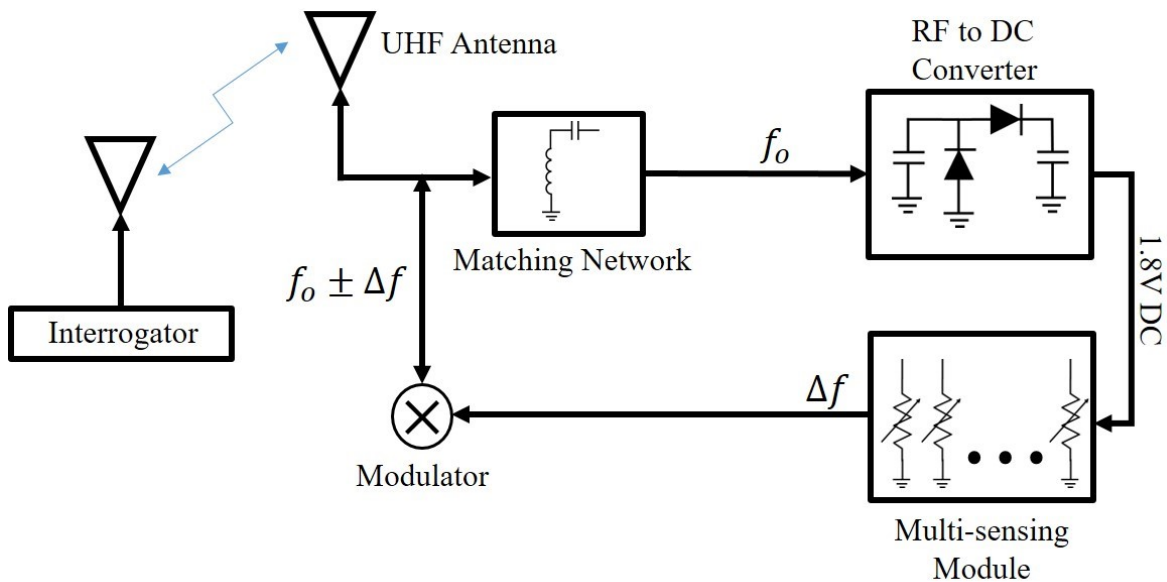


Figure A.1: Schematic of a passive wireless system with multi-sensing RF tag and Interrogator

A.3 Design

The passive wireless multiple sensing system is composed of an RF tag and an RF interrogator as shown in Fig.A.1. The design details of each fundamental block of the multisensor RF tag and RF interrogator are discussed in this section.

A.3.1 Antenna Design

An UHF RFID tag antenna is designed to transmit and receive the information from the RF interrogator. A smaller footprint antenna is designed for the RF tag to operate in a frequency band from 902-928 MHz by meandering the conventional dipole antenna. ANSYS HFSS[®] (2019, ANSYS, Inc., Canonsburg, PA, USA) is used to simulate the design of the antenna with Roger's 4350 ($\epsilon_r = 3.66$, and $\tan\delta = 0.003$) dielectric substrate with thickness of 1.52 mm. The antenna is fabricated using the conventional photolithography process. The schematic of the antenna along with its dimensions and its frequency response is shown in Fig. A.2A. The measured frequency response matches closely with the simulated frequency response, as shown in shown in Fig. A.2B.

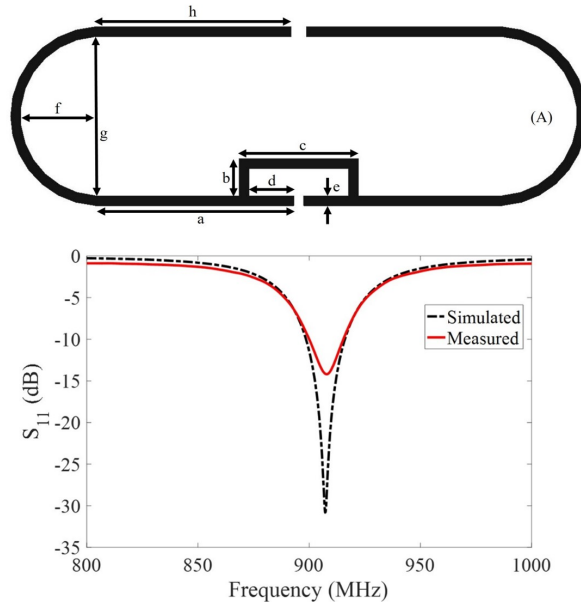


Figure A.2: UHF RFID Antenna: (A) Schematic of the dipole antenna and dimensions, (B) Simulated and measured frequency response

Table A.1: Dimensions of the 915 MHz antenna

Parameter	a	b	c	d
Dimensions (mm)	20.0	3.75	12.0	4.5
Parameter	e	f	g	h
Dimensions (mm)	1.0	8.0	16.0	19.75

A.3.2 RF to DC converter

The antenna receives the RF signal from the interrogator as a single frequency continuous wave at the chosen UHF RFID frequency of 908 MHz. The received signal is backscattered with the modulated sensor information generated by the oscillator coupled with the multisensing module. The oscillator requires a DC supply to operate, which is harvested from the received RF signal from the interrogator using an RF-to-DC converter (rectifier). The implemented converter is a five-stage Dickinson charge pump rectifier that can convert a range of input RF power (0 dBm to -6 dBm) to DC output voltage. A Zener diode is connected in parallel to the output of the charge pump circuit to limit the maximum rectifier's up converted DC voltage to 5 V. A high efficiency regulator (TPS79718) from Texas Instruments is used to regulate the up converted voltage signal to 1.8 V in order to supply the required DC power for the oscillator.

The designed rectifier with voltage regulator is tested with a range of received RF power from 0 dBm to -7 dBm. The output voltage of 1.8 V is connected to a variable load resistance to calculate the total available DC power at the output of RF-to-DC converter unit. The corresponding output DC power range from 350 μ W to 10 μ W for the input RF power from 0 dBm to -7 dBm as shown in Fig.A.3.

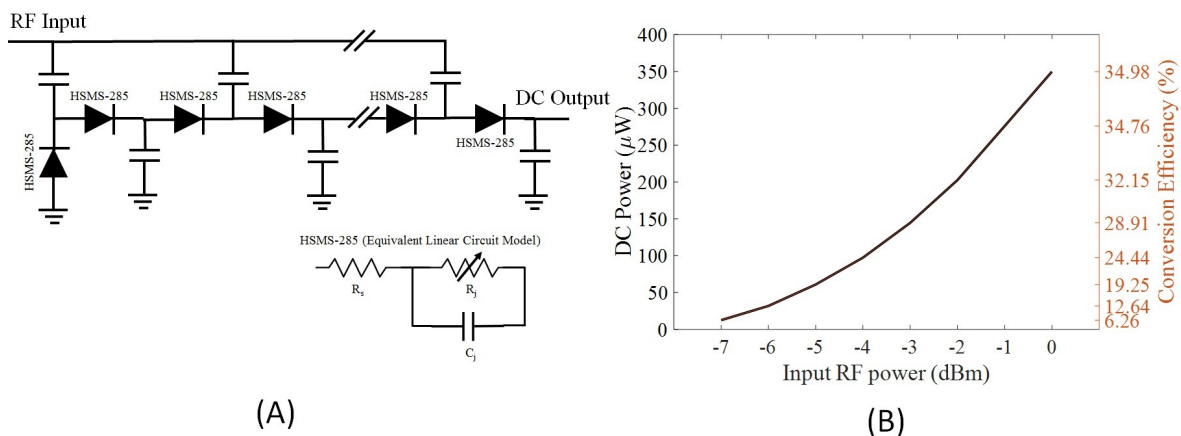


Figure A.3: (A) Schematic of RF-to-DC converter, (B) Input RF power vs Output DC power

The minimum power required to operate the frequency oscillator at 150 kHz is 30 μ W, as explained in the next section, which can be harvested from a minimum input RF power of -6 dBm,

making it the minimum operating limit or the sensitivity level of the designed multisensing RF tag.

A.3.3 Multi-sensing Module

The multisensing module generates a wide range of frequencies according to the number of sensors coupled to the low frequency oscillator through a single-pole-multiple-throw (SPMT) switch. The oscillation frequency range is defined by the available channel bandwidth of the RFID system. Within the available bandwidth, a number of subbands are allocated to each sensor element coupled to the oscillator. The different sensor elements change the oscillation frequency according to the change in their respective physical parameter (for example, temperature, luminescence, humidity, etc). Although a SPDT switch (TS5A2053) was used for the prototype as the prototype uses two example sensors, multiple sensors can be connected by changing the switch. The switch couples the oscillator to different sensing elements by selecting a single sensor at a given point of time. The toggle frequency should be fast enough to sweep through all the coupled sensors in minimum time while maintaining the integrity of the output frequency signal from the oscillator, which is defined by the oscillator's stability time. In this work the toggle frequency is set to 6 kHz for selecting in between temperature and luminescence sensors, which is found experimentally to get the stable oscillations in minimum time. The toggle frequency of 6 kHz corresponds to a single sensor read time of approximately 160 μ s.

The multisensing frequency source is realized using an ultra low power oscillator IC (LTC6906) from Linear Technology with an operating voltage range from 1.8 V to 5.5 V. In the proposed passive wireless multiple sensing application, the minimum power consumption is paramount, for which an experiment is performed to generate a fixed 100 KHz signal while feeding the oscillator with a range of input voltages from 1.8- 5 V, and the corresponding current consumption plot is shown in Fig. A.4A. A linear relationship exists between the current and the voltage, and a minimum current is drawn for the minimum input required voltage of 1.8 V.

A ultra low power oscillator IC that generates a single tone frequency based on the value of the resistance across it is chosen due to the wide availability of a variety of resistive sensors. The selected

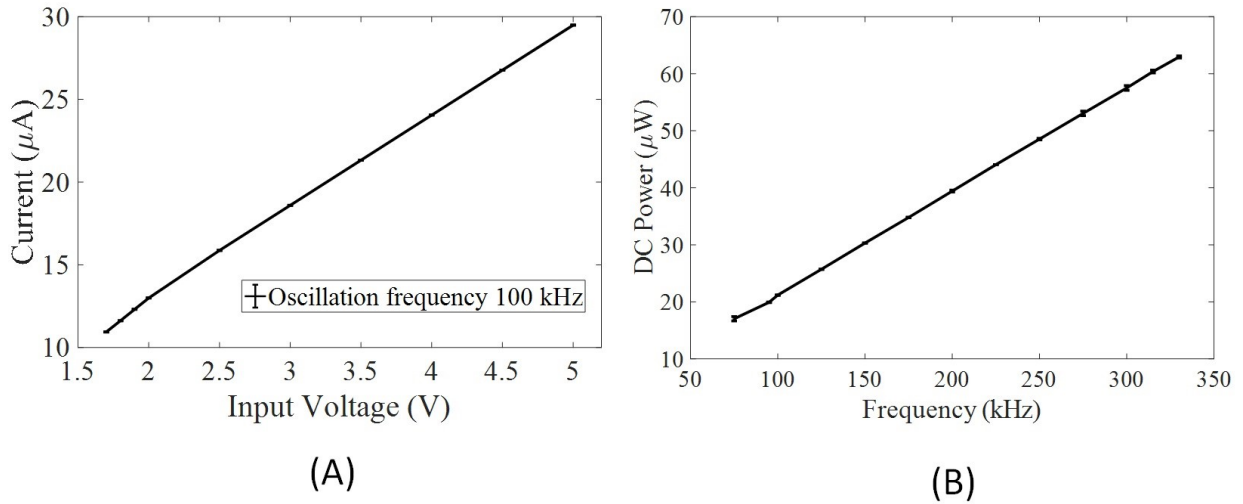


Figure A.4: (A) Input voltage vs Input current at 100 kHz oscillation frequency, (B) Oscillation frequency in kHz vs required Input power in microwatts

oscillator can generate frequencies from 10 kHz to 1 MHz according to the coupled resistance. The oscillator's power consumption increases with the increase in frequency, an experiment is performed to extract the power requirements to generate a range of frequency signals from 75- 325 kHz. A variable resistor is used to change the oscillation frequency, and the required minimum input voltage of 1.8 V is supplied to the oscillator. The oscillator's required DC power is calculated by measuring the current consumption at 1.8 V for different oscillation frequencies. The plot of oscillation frequency vs required DC power is shown in Fig. A.4B.

The oscillator is capable of generating a frequency as low as 10 kHz, where the DC power requirements would be even lower. But in this paper, the frequency operation lower than 75 kHz is avoided intentionally due to the presence of phase noise skirt in the UHF carrier frequency signal. Hence, the lower frequency signals may get affected by the higher noise level and introduce difficulties in detection by the interrogator. The lower frequency modulation can be used with the other carrier signals with a very low phase noise level. The upper bound on modulation frequency is set by the channel bandwidth of the UHF RFID protocol, which is 300 kHz or ± 150 kHz on both size of the carrier wave. According to the plot shown in Fig. A.4B, the maximum power required to generate 150 kHz is $30\mu\text{W}$. The circuit diagram of the multisensing module with modulator is

shown in Fig.A.5.

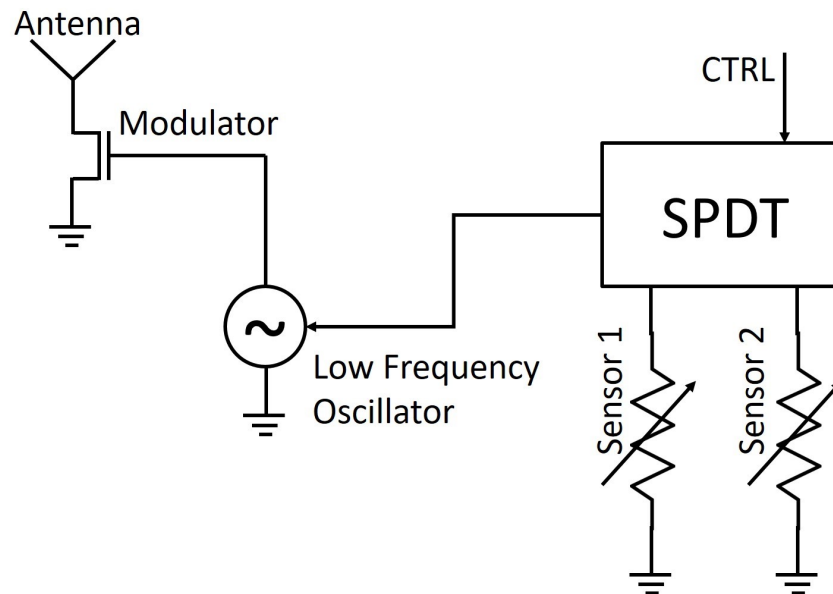


Figure A.5: Circuit diagram of the designed multi-sensing module

A.3.4 Modulator

The frequency signal generated by the oscillator according to the different sensor values is modulated to a high frequency carrier signal for information transmission. A 25 kHz band is assigned to each sensor with a guard band, also 25 kHz, in between each sensor bands, as shown in Fig. A.6A. The frequency band for the first sensor is from 75 kHz to 100 kHz, and the second sensor is from 125 kHz to 150 kHz. The UHF RFID band is used for the communication, a frequency of 908 MHz is selected to modulate, for instance, 100 kHz and 150 kHz signals representing first and second sensors, respectively.

A MOSFET (BF904) from NXP semiconductors is used to modulate or mix the low frequency information signal with the high frequency carrier signal. First, the multisensor RF tag is tested in a wired setup. A 10 dB directional coupler is used to feed the 908 MHz signal across the drain and source pin of the MOSFET, and the low frequency signal from the oscillator is fed into the gate pin. The back-scattered signal with the sensor modulation is measured at the coupled port of the directional coupler as shown in Fig. A.6B. The received frequency signal of 100 kHz and 150 kHz

belongs to the preallocated sub-bands, which represents a physical parameter with a specific value. For validation purpose, the sub-bands are generated using variable resistors.

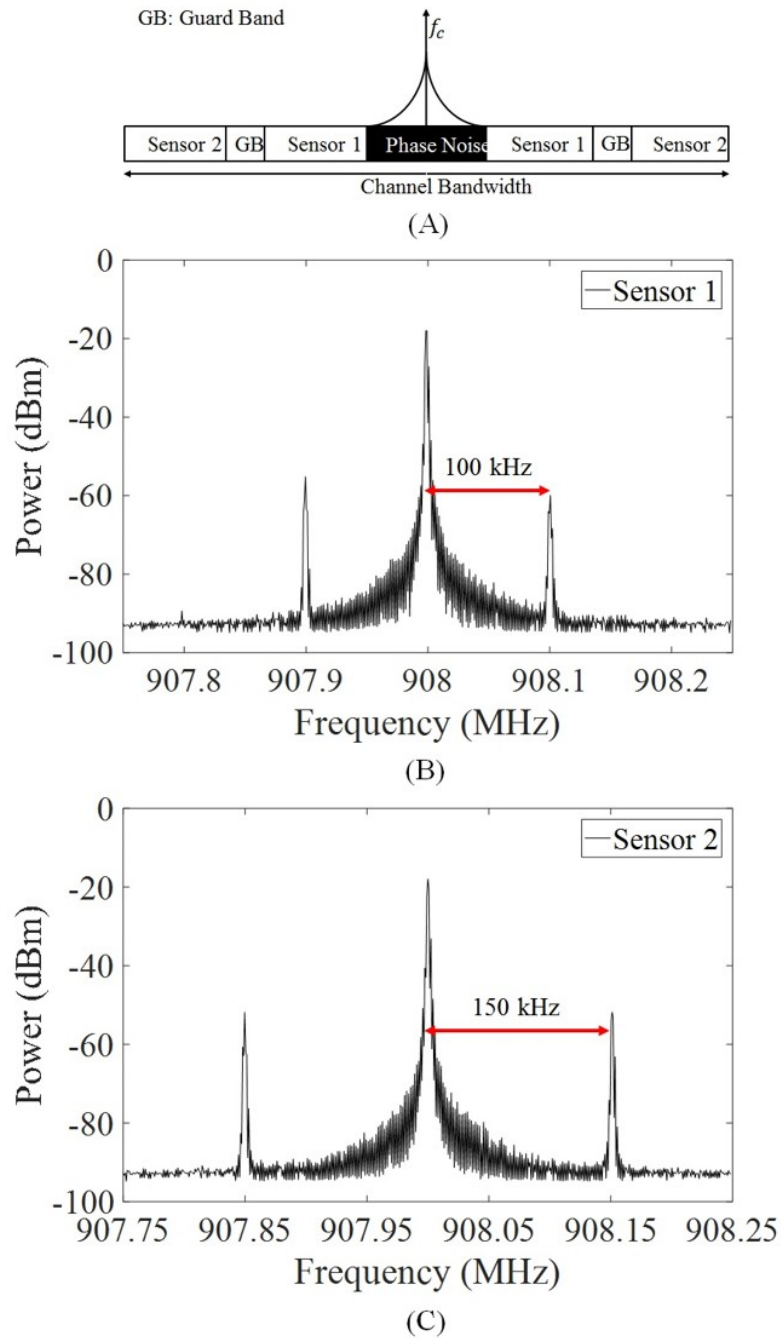


Figure A.6: Sensing information modulation: (A) Schematic of the modulation scheme and (B) Modulated sensor information of 100 kHz and 150 kHz on 908 MHz carrier frequency

A.3.5 RF Interrogator

The wireless communication with a multisensor RF tag requires a custom designed RF interrogator, which transmits and receives the UHF RF signal. The interrogator consists of an RF source that can generate UHF continuous wave, which is radiated using a commercial patch antenna with 6 dBi gain. The multisensor RF tag receives a single frequency signal from the tag antenna and backscatters the information in the form of modulated RF signal, which is received by using the same transceiver antenna. A circulator is connected at the front end of the interrogator to isolate the forward and backward propagating signal to and from the transceiver antenna. The received signal is demodulated and the sensor response is obtained. A RF mixer was used for demodulation by feeding a reference UHF signal into LO PORT and the back-scattered modulated signal into the RF port after 36 dB amplification using a LNA. The demodulated signal is acquired at the IF PORT of the mixer. The schematic of the RF interrogator is shown in Fig.A.7, where the RF interrogator transmit and receives information to and from the multisensor RF tag. The complete RF interrogator was assembled using commercial RF parts from Minicircuits.

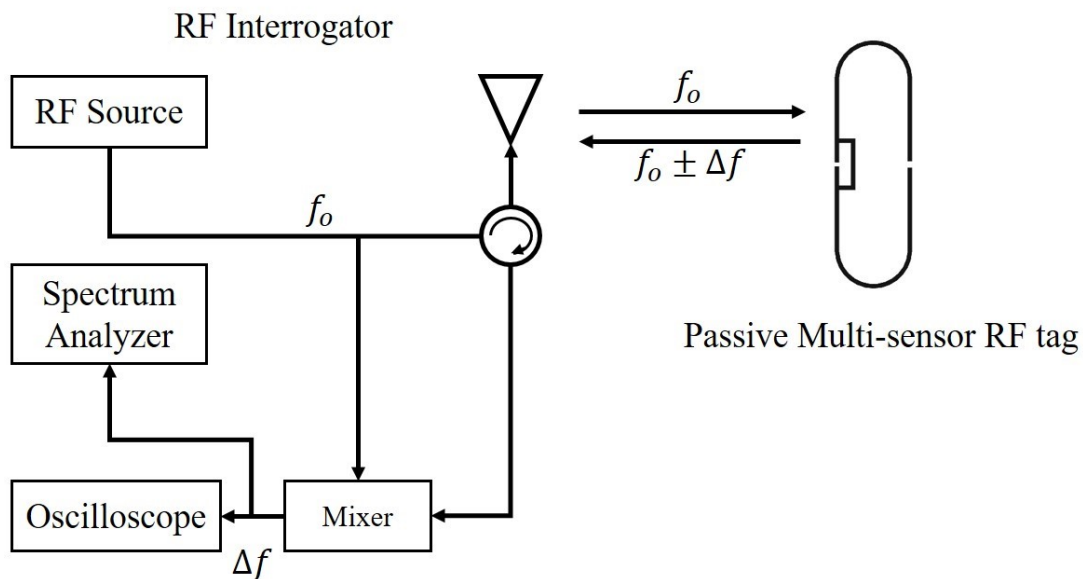


Figure A.7: Schematic of the RF interrogator radiating +36 dBm EIRP and visualizing the back reflected sensor information using a spectrum analyzer and an oscilloscope

A.4 Results

For demonstrating the real-time passive wireless multisensor platform, the experiments are performed in two different configurations: Wired for validation and wireless for demonstration. The wired validation is performed to check the effects of input RF power on side band power, a measure of resistance required to generate the frequency from 75 kHz to 150 kHz, and the relationship of temperature and luminescence sensor with the resistance. The wireless demonstration of temperature and luminescence shows the successful communication from RF tag to interrogator by visualizing the demodulated sensor information using spectrum analyzer and oscilloscope in frequency domain and time domain, respectively.

A.4.1 Wired Validation

The performance of multisensor RF tag is tested by establishing a direct wired connection through the antenna port. Similar setup as described earlier, a 10 dB directional coupler is used to feed the UHF RF power into the multisensor RF tag and the reflected signal is acquired at the coupled port using a spectrum analyzer. First experiment is performed to test the minimum input RF power required to activate the multisensor RF tag and the effects of variable input RF power on the reflected modulated side band power. The oscillator is set to generate 100 kHz and 150 kHz frequency signal, which represents the information from the first and second sensor, respectively. The minimum RF power required to activate the multisensor RF tag is found out to be -6 dBm at which the oscillator generates a frequency up to 150 kHz and successfully modulates it on the carrier signal. The back reflected power at the modulated side bands do not vary with the input RF power range from 0 to -6 dBm, as shown in Fig. A.8, as the output voltage level of the oscillator is fixed at $1.8 V_{pp}$ according to the input DC supply.

Second set of experiments are performed for validating the resistance required to generate the frequency range in the available bandwidth from 75-150 kHz. A variable resistor is used to change the oscillation frequency. The decreasing resistance range of 440 k Ω to 340 k Ω is required for 75

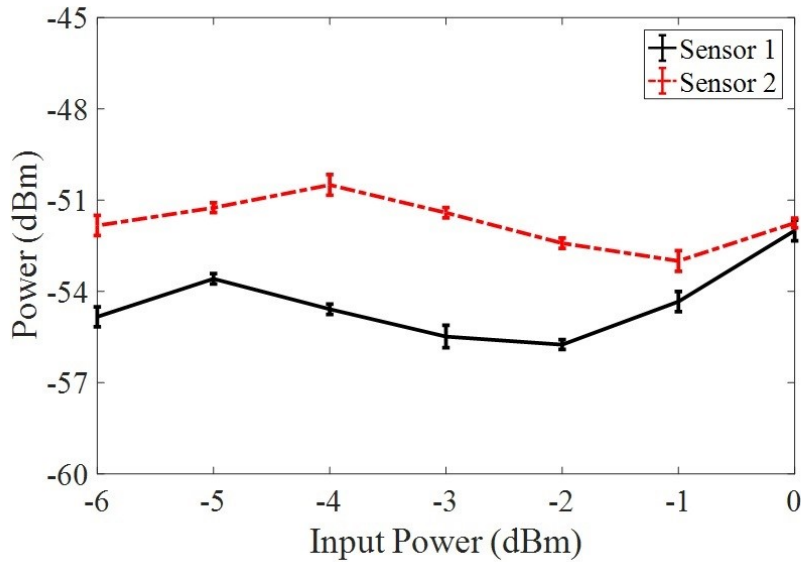


Figure A.8: Wired validation: Received side band power of a carrier signal due to first and second sensor with varying input power

kHz to 100 kHz and 260 k Ω to 220 k Ω for 125 kHz to 150 kHz. Another advantage of using such a high resistance reduces the power consumption significantly. A guard band from 341 k Ω to 259 k Ω (101 kHz to 124 kHz) is adopted for easier classification (differentiation) and detection of different sensor type and data, respectively.

The resistance based temperature and luminescence sensors are selected for demonstrating the real-time passive wireless multi-sensing capability. A commercial temperature sensor IC [148] is selected as first sensor element that is able to detect a range from 25 $^{\circ}$ C to 60 $^{\circ}$ C, and a commercial light-dependent resistor (LDR) [149] is selected as the second sensor element that is able to detect the luminescence from 0-20 fc. The temperature sensor IC changes its resistance from 100 k Ω to 8 k Ω for the given temperature range, which is tailored to 440 k Ω to 348 k Ω by adding a series resistance of 340 k Ω in order to generate the respective oscillation frequencies with in the range from 75-100 kHz. Similarly, for LDR, the resistance range is tailored to generate the resistance range from 260 k Ω to 220 k Ω for a given luminescence range while generating the frequency from 125-150 kHz. The temperature and luminescence relation with frequency is shown in Fig. A.9. As shown in Fig. A.9, the linear sensitivities are respectively 0.53 (kHz/ $^{\circ}$ C) and 0.862 (kHz/fc)

for the temperature and light sensor. The R-square value for the linear fits is 0.84 and 0.464 for temperature and light sensors, respectively. However, the R-square value improves to 0.987 and 0.711, respectively with second-order polynomial fit.

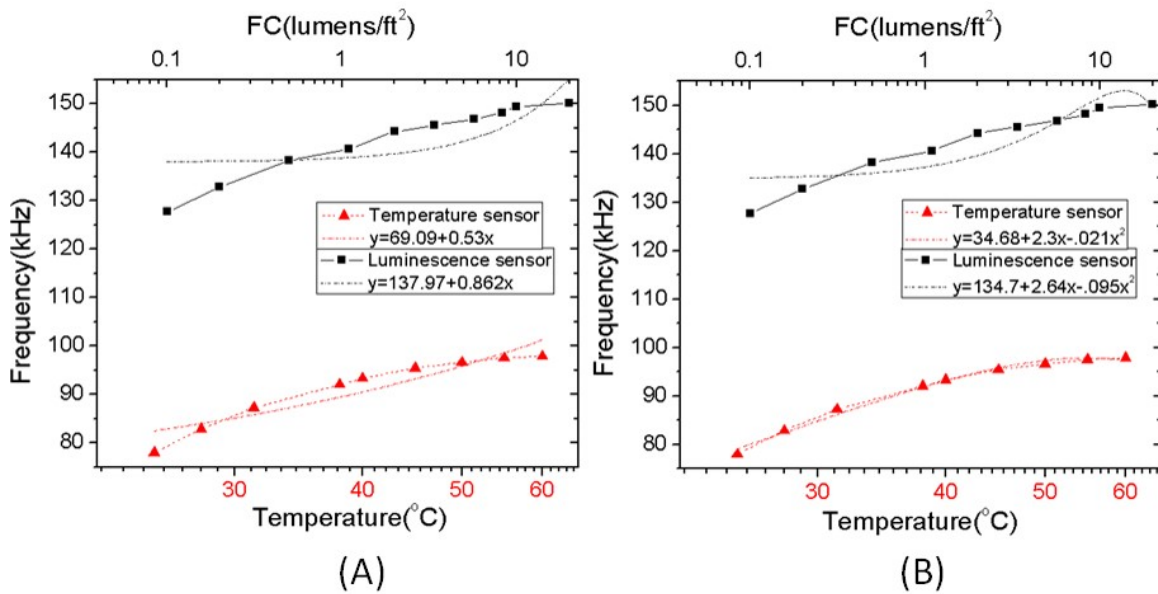


Figure A.9: Frequency change of temperature and luminescence sensors (A) with linear fit and (B) with second order polynomial fit

A.4.2 Wireless Demonstration

A wireless communication in between the RF interrogator and the multisensing RF tag is demonstrated by transmitting an RF power of +9 dBm using a 6 dBi gain patch antenna. The operating frequency is 908 MHz and multiple sensor tag measurements are acquired with 6 to 14 inches of separation from the interrogator's antenna. Prototype of the passive RF tag with PCB assembly and antenna is shown in Fig.A.10.

The wirelessly received power at the RF tag with varying read range is experimentally measured and compared in Fig. A.11 with the ideal received power using Friis's transmission equation. The antenna's interference from nearby objects, multi-path propagation, and noise in the system effects the carrier's received power and introduce a deviation of ± 1.5 dBm from ideal measurements. The multisensor RF tag, backscatter frequency modulated sensor information, and the received side

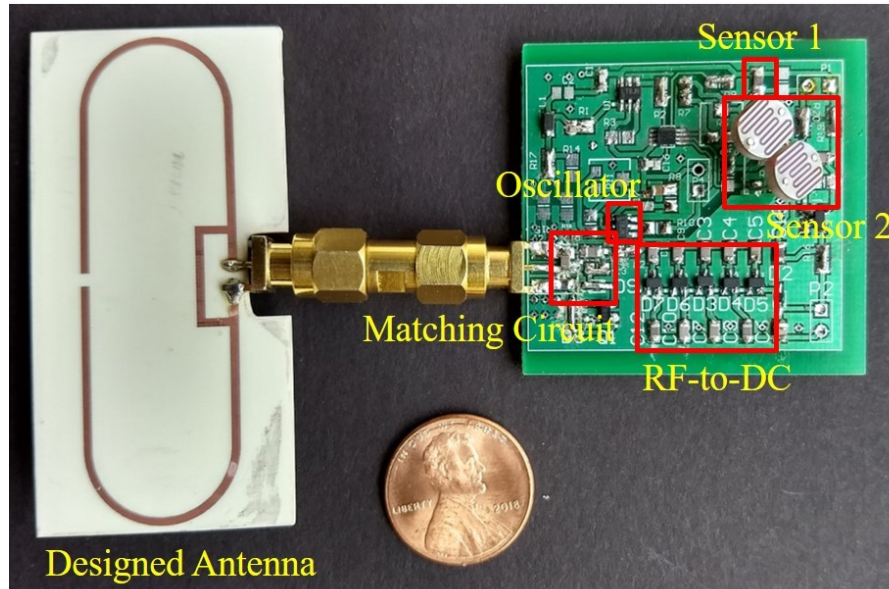


Figure A.10: The prototype of RF Tag with designed antenna, integrated sensors, and assembled PCB

band power for both sensors are shown in Fig.A.11. The received side band power decreases with the increase in interrogator-tag separation. The RF tag receives the required minimum RF power of -6 dBm at a distance of 12 inches, which is the communication range with 9 dBm radiated power. An additional experiment is performed to test the maximum read range while transmitting the maximum allowable EIRP of 36 dBm, with the sensitivity of -6 dBm, the multisensor RF tag is able to communicate the sensor information up to 10 ft.

The temperature and luminescence sensors reflect back the information signal in the form of modulated side band frequencies. The received frequency for temperature and luminescence sensor are 82.34 kHz and 149.59 kHz, which corresponds to 27.8°C and 13 fc. The temperature and lighting conditions of the experimenting lab are verified using a commercial temperature and light measuring instrument from URCERI. The frequency spectrum of the received demodulated signal is shown in Fig. A.12A. The frequency signal (sensor data) peaks are clearly visible, the frequency modulation of the sensor data is immune to any multi-path interference or noise in the propagation. The time domain representation of the demodulated RF signal is shown in Fig. A.12B, where the information signals from the first and second sensors are repeating in time with a time period of

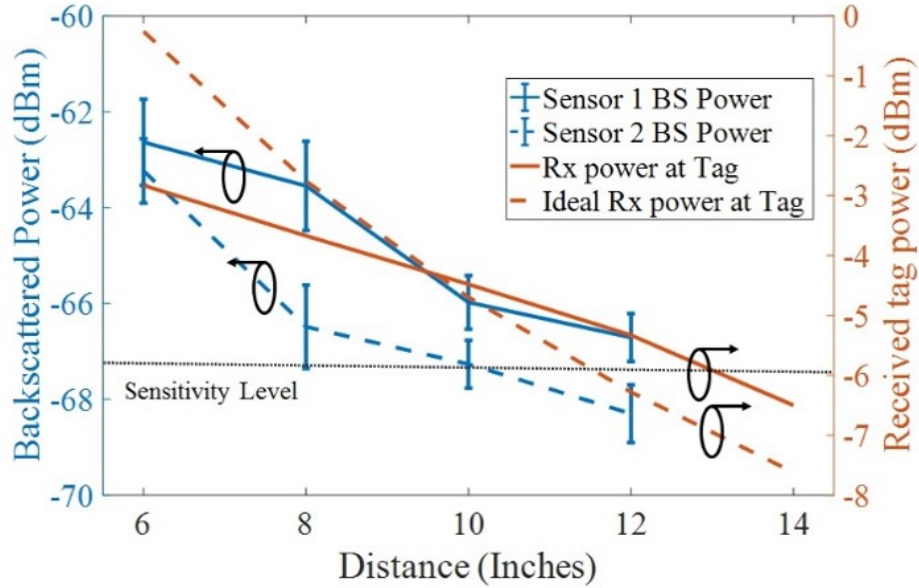


Figure A.11: Wireless demonstration with 9 dBm transmitted power at 908 MHz: Received RF power at multisensor tag vs distance and backscattered

approximately $160 \mu\text{s}$. The temperature and luminescence signals with 82.34 kHz and 149.59 kHz frequencies, respectively, are shown in zoomed section. The demodulated signal is amplified using a 40 dB low frequency amplifier before acquiring the data using an oscilloscope.

The sensors used in the system are analog in nature. Hence, the minimum resolution of the sensors depends on the measurement instrument used at the interrogator. For a standard oscilloscope with 1% measurement accuracy for bandwidth up-to 200 kHz, the minimum resolution will be 2.6 $^{\circ}\text{C}$ for temperature sensor and 1.2 fc for the photosensor.

A.5 Discussion, Challenges and Limitations

A passive multiple sensing platform is designed, developed and demonstrated using a power efficient analog frequency modulation. The sensing system operates in UHF RFID band from 902-928 MHz and back-scatters the multiple sensor information in the form of frequency modulation. The ultra low power frequency oscillator is connected on the board, which changes its oscillation frequency according to sensor information. In this work, a resistance based oscillator is used for multisensor module. The oscillator can be designed with a combination of RLC elements where

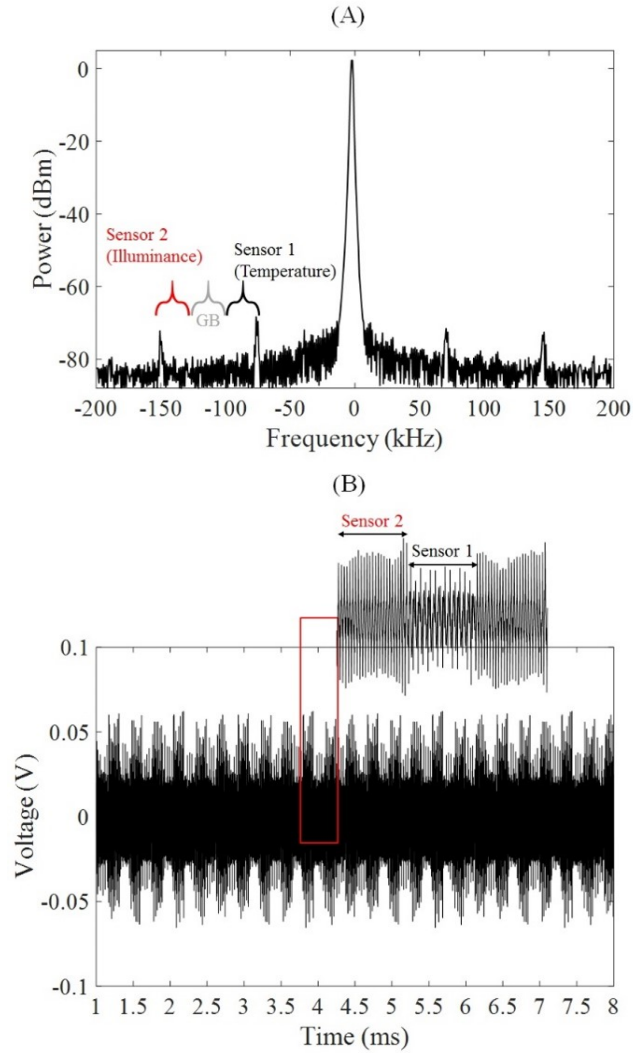


Figure A.12: Wireless demonstration with 9 dBm transmitted power at 908 MHz: (A) Frequency spectrum of the demodulated sensor data, and (B) Received sensor information in time domain with a switching frequency of 6 kHz ($\sim 160 \mu s$)

the resonance can be changed by varying the resistance, capacitance, or inductance. The operating frequency range is limited by the total available bandwidth in which a number of subbands are allocated to different sensor types. To integrate a large number of sensors within a single channel bandwidth, the size of subband and guard band can be reduced. For operating at a lower frequency, the phase noise issues can be eliminated using harmonic communication method [87, 150]. The system's reliability depends on the voltage level of the oscillator, switch, and sensors. As long as the tag obtains its minimum power, the regulator will maintain its constant voltage level ensuring

proper functioning of all components. The interrogation distance of the system is limited by the DC power requirement of the multi-sensor RF tag that can be improved by implementing a more efficient RF-to-DC conversion mechanism.

There can be interference among the sensors when used together in the system. However, the interference is primarily due to the leakage through the switch selecting one sensor at a time between the both. According to the datasheet, the SPDT switch has isolation of 68 dB for switching clock operating below 10 MHz, which means the desired sensor signal level will be 68 dB above the undesired sensor signal. To further reduce the interference, a higher isolation switch should be used. Other challenge of the passive multiple sensing system is to communicate with multiple RF tags simultaneously and extract the multisensor information from each tag. It requires an additional information layer to classify different multisensor RFID nodes and extract the information. The multiple tag communication protocol is a well studied and a number of efficient circuitries are available in the literature [49, 134], but digital sensing is very power inefficient due to ADC requirements.

A.6 Summary

A passive multisensing RF system is shown for real-time communication with the multiple sensors coupled to an RF tag. The demonstrated multisensor RF tag is able to communicate with an RF interrogator up-to a read range of 10 ft. The RF tag uses an oscillator to generate a unique single frequency signal corresponding to the temperature and luminescence sensing values, and transmit the information by frequency modulating a 908 MHz RFID carrier signal. Each of the sensors' information is modulated within the available channel bandwidth of 300 kHz at the pre-allocated frequency range from 75-100 KHz and 125-150 kHz. The back-scattered frequency modulated signal is immune to noise or interference due to multi-path propagation, and power efficient as it eliminates the requirement of any analog to digital conversion. The demonstrated analog frequency modulation based passive RF system shows an efficient, real-time and long-range multi-sensor information transmission method for IoT based applications.

APPENDIX B

IDENTIFICATION AND SENSING SYSTEM (ISS): AN OPEN SOURCE RFID PLATFORM

B.1 Introduction

In this chapter, we present ISS; an RFID platform for both single band (902-928 MHz) and harmonic (433-434 MHz) band operation. The platform operates on modified EPC Gen2 RFID protocol to accommodate identification and sensing together. The ISS supports communication with digital sensor tags, which makes it ideal for passive impedance (resistance, capacitance, and inductance) measurement. The working ISS is demonstrated by wirelessly communicating with a digital sensor. The custom-designed interrogator and tags for ISS wirelessly communicate with single or multiple sensor tags in its field of view. Additionally, a performance evaluation study is shown for single vs harmonic frequency operation.

B.2 Design

The design section of ISS comprised of three unique hardware elements; two types of RFID tags and an RFID interrogator. The first designed RFID tag uses a conventional single-frequency RFID communication mechanism, which is required to study well known phase noise issues. Second, RFID tag uses a harmonic communication mechanism to overcome the limitations of the conventional system. At last, a multifrequency interrogator is designed to communicate with both single-frequency and harmonic-frequency RFID tags. All three elements are discussed in detail below.

B.2.1 Digital Single-frequency RFID Tag

The design of a digital single-frequency RFID tag has been widely studied. The hardware implementation of this work is highly inspired from the Wireless Identification and Sensing Platform

(WISP), which acts as a base for this new development work [86, 135]. The software providing logic to ISS is developed from scratch to accommodate new requirements, like; custom interrogator, variable data rate, timing, etc. Therefore, we called it modified EPC Gen2 RFID protocol. The hardware implementation and software stack for tag are discussed in following sections. The schematic of the designed single frequency RFID tag is shown in Fig.B.1.

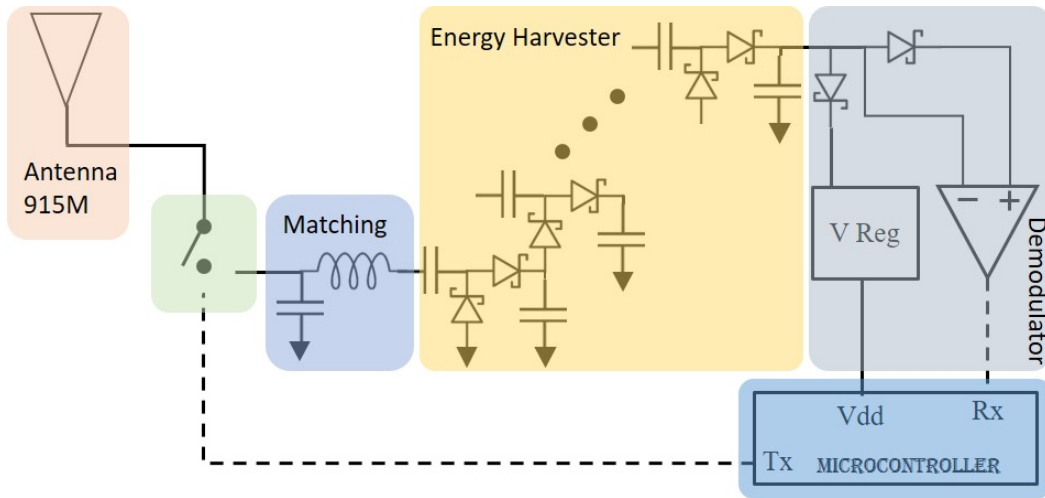


Figure B.1: Schematic of the digital single frequency tag for receiving and transmitting at 915 MHz

B.2.1.1 Modified EPC Gen2 RFID tag protocol implementation

The RFID tag protocol is divided into two main parts; receiver and transmitter. The receiver part can decode the digital commands sent from the interrogator and respond accordingly. The general EPC Gen2 protocol for RFID requires a tag to implement 11 mandatory commands for commercial use. However, we only implemented 6 (Query, QueryAdjust, QueryRep, ACK, NAK, Req_RN) for the research and development ease, which are enough to have a reliable communication with multiple RFID tags in the field of view. The RFID tag holds one of the states (Ready, Arbitrate, Reply, Acknowledged), which is switched according to the received command. When a tag will reach "Reply" state, it prepares for transmitting identification or sensing information.

The transmitter part can either operate in ID only or ID with sensor configuration. If operating in ID-only mode, the tag calculates CRC-16 for the given EPC and appends together all components

required according to the data frame shown in Table.B.1.

Table B.1: Data frame format for Digital ID Reply

P	EPC	CRC-16
---	-----	--------

Where P is Preamble, EPC is Electronic Product Code (40-bits), and CRC-16 is Packet Cyclic Redundancy Check (16-bits).

On the other hand, if the tag has an integrated sensor, it uses ADC to convert the sensor data into digital bits and append it together according to the data frame shown in Table.B.2.

Table B.2: Data frame format for Digital ID with Sensor Data Reply

P	EPC	ST	SP	SD	CRC-16
---	-----	----	----	----	--------

Where, P, EPC, and CRC-16 are same as above. Additionally, ST is Sensor Type (8-bits), SP is Sensing Parameter (4-bits), SD is Sensor Data (12-bits).

The preamble and product code are used as defined in EPC Gen2 protocol [151]. An example EPC: 0×E200A10090 is used in this paper for demonstration. The implementation list of sensing parameters and sensing type is shown in Table B.3 and Table B.4. The codes shown in this table will be used throughout this chapter for consistency.

Table B.3: 4-bit codes for different sensing parameters

Sensing Parameters	4-bit Code
Resistive	0000
Capacitive	0001
Inductive	0010
Voltage	0011

According to this proposed format, 16 different types of sensing parameters and 256 different sensors can be coded as prior knowledge, so each sensor tag can be characterized correctly.

The binary sequence for the data frame is encoded using FM0 (Miller method) technique before transmission for reliable data transfer as described in EPC Gen2 RFID protocol. The default

Table B.4: 8-bit codes for different sensor types

Sensor Type	8-bit Code
Temperature	00000000
Pressure	00000001
pH	00000010
Humidity	00000011

reply rate is 60 kbps with encoded bits, which can go up-to 106 kbps. At higher data rate, the power requirements for the computation also increase. The power harvesting mechanism and ASK modulation mechanism for transferring bits is explained below.

B.2.1.2 915 MHz Energy Harvester

The single frequency operation works in a frequency range from 902-928 MHz. The schematic of the designed energy harvester is shown in Fig.B.2A. The on-board energy harvester circuit converts the RF signal into DC signal for executing the protocol stored in the microcontroller. The input impedance of the energy harvester is a function of input power, therefore, a sweep from -2 to -10 dBm is performed to ensure good matching with wide range of input power levels. The measured frequency response of the designed energy harvester with power sweep is shown in Fig.B.2B.

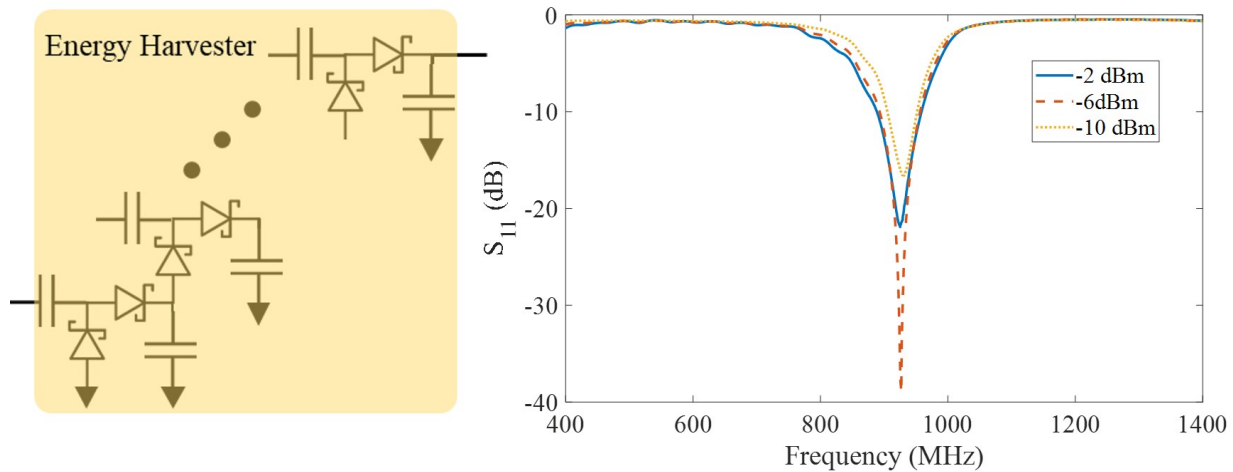


Figure B.2: (A) Schematic of the designed energy harvester, (B) Measured frequency response of the energy harvester with input power sweep

B.2.1.3 ASK Modulator

An ASK modulator is used to backscatter the RF signal from the tag with the ID and sensor data bits. An ultra low power SPST RF switch (HMC550) is used to introduce an impedance mismatch that translates into an amplitude shift of the backreflected signal. A simple setup with RF circulator and designed RFID tag shown in Fig.B.3A for checking the modulation signal. The port 1 of the circulator is connected to RF source that feeds the RFID tag at port 2 and the reflected signal from the tag is read by an oscilloscope from port 3. The acquired back reflected signal is shown in Fig.B.3B.

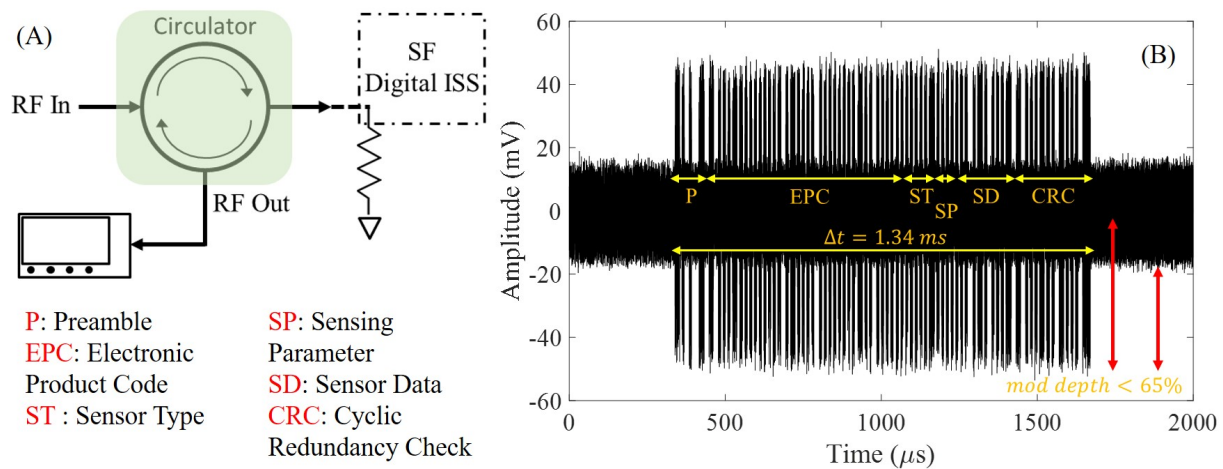


Figure B.3: (A) Measurement setup for ASK modulation at 915 MHz, (B) Measured back reflected RF signal with modulated ID

B.2.2 Digital Harmonic-frequency RFID Tag

The digital harmonic-frequency RFID tag is designed to overcome the phase noise issue of the single-frequency operation as shown in Chapter 3. The tag protocol for harmonic RFID is the same as the single frequency RFID system. The major difference is in the operating frequency and generation of harmonic signals. A new energy harvester is designed to operate at 434 MHz, while the switch for modulation is placed on the output path before the nonlinear elements for generating harmonic signals. The schematic of the digital harmonic-frequency RFID tag is shown in Fig.B.4.

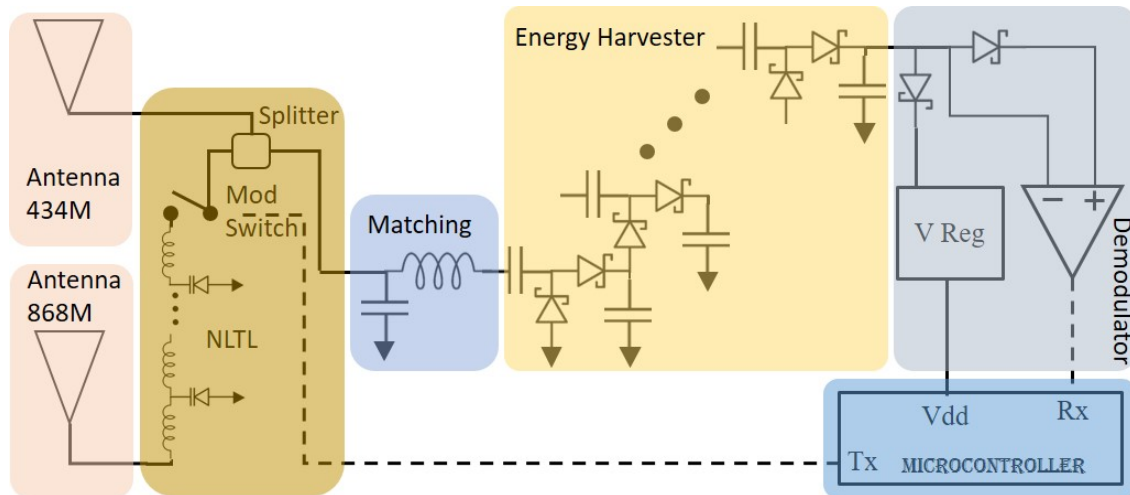


Figure B.4: Schematic of the digital harmonic tag for receiving at 434MHz and transmitting at 868MHz

B.2.2.1 434 MHz Energy Harvester

The energy harvester at 434 MHz is tested for impedance matching at various power levels. The frequency response for the power sweep is shown in Fig.B.5. The energy harvester is fed from port 1 of RF splitter, which receives the signal from antenna connected to the input port.

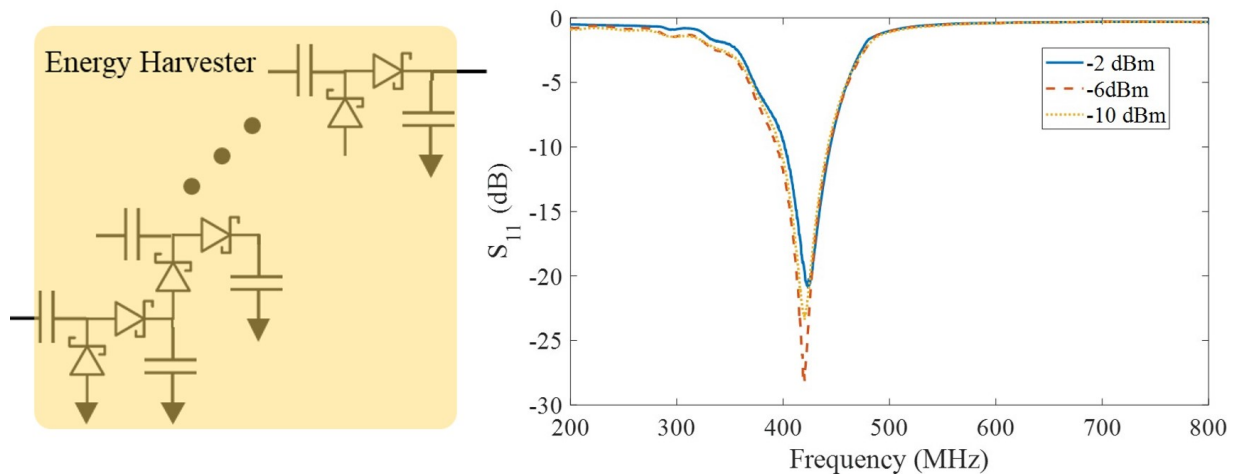


Figure B.5: Schematic of the 434-868 MHz digital RFID tag

B.2.2.2 OOK Modulator

The OOK switch (HMC550) is used to modulate the digital data with backreflected harmonic signals. The splitter at tag input feeds the RF switch from port 2. The output of the switch is connected to the nonlinear element (NLTL) for harmonic generation. The output of NLTL is connected to the oscilloscope for checking the modulation, the acquired signal is shown in Fig.B.6B.

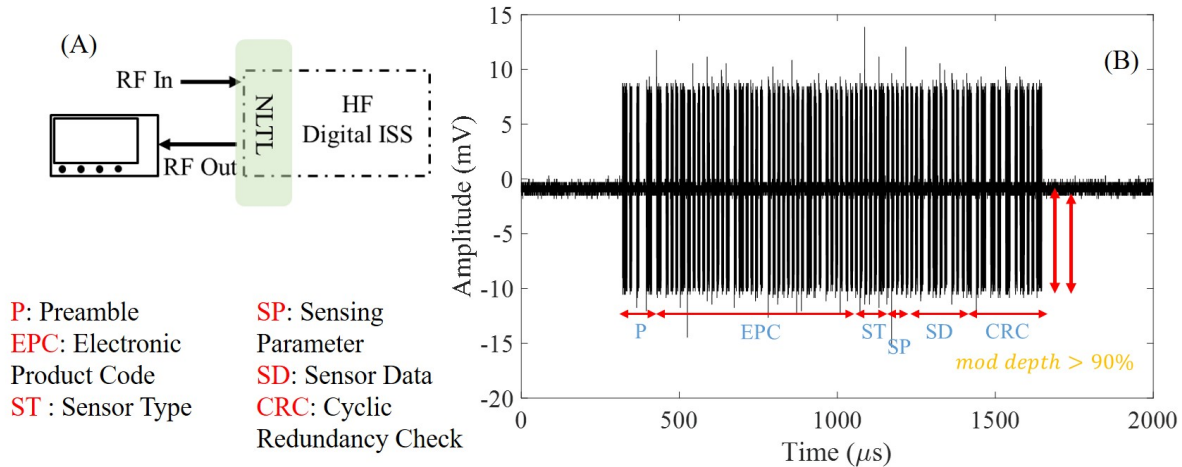


Figure B.6: (A) Measurement setup for ASK modulation at 434 MHz, (B) Measured back reflected RF signal with modulated ID

B.2.3 Multi-frequency RFID Interrogator

Most of the sensor integrated RFID development work is conventionally performed around the existing EPC gen2 protocol and off-the-self interrogator, which was never meant to be designed for sensing applications. The multiple bottle neck problems (self-jamming, digital only) of the conventional interrogators cannot be eliminated using next generation tag design. For pushing the boundaries in passive RF sensing and communication, a new interrogator needs to be designed as well. We are proposing an architecture for a multifrequency interrogator.

A new custom interrogator is designed to communicate with the ISS's digital single and harmonic frequency RFID tags. The basic functionality of an interrogator is to transmit and receive RF signals, which needs to be modulated on the way-out and demodulated on the way-in. Both

the modulator and demodulator are part of the RF front-end, with additional peripherals like power amplifier, LNA, filters, heterodyning mixer, etc. The block diagram of the designed interrogator with multi-frequency operation and hybrid reception is shown in Fig.B.7.

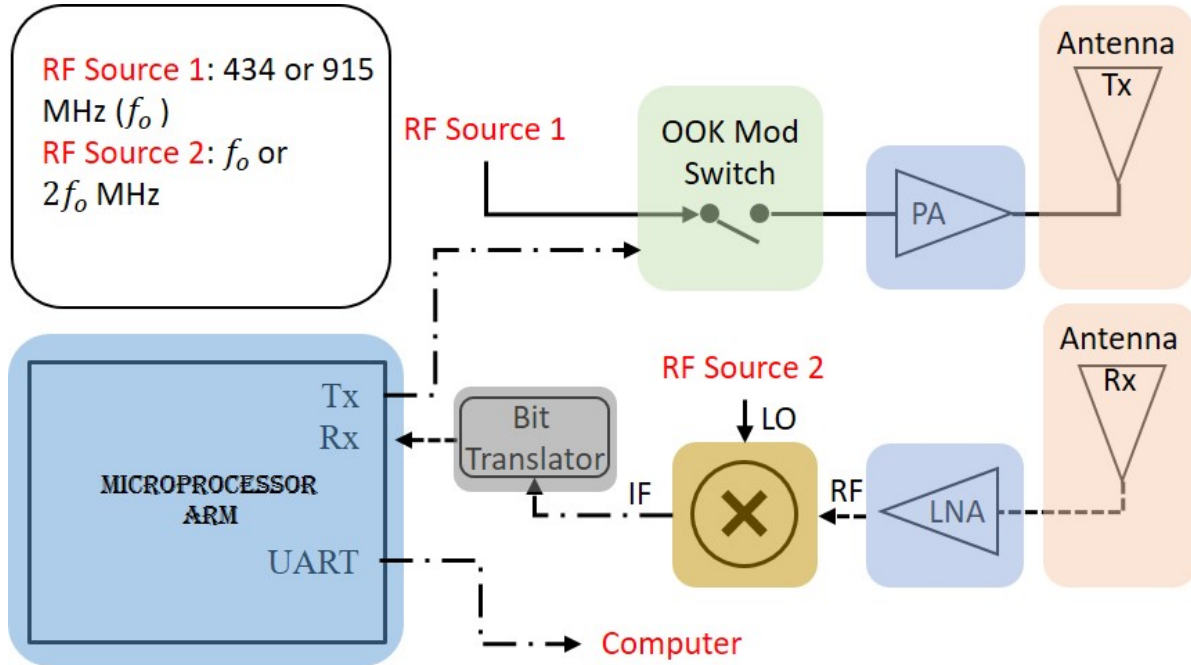


Figure B.7: Block diagram of the ISS interrogator

A continuous RF source of 915 MHz and 434 MHz is required. The 915 MHz and 434 MHz RF sources are fed into an OOK modulator, implemented using SPST RF switch (name switch). The modulator receives digital command bits from the on-board processing unit, to power all available digital RFID tags in the field of view. The processing unit also selects the single or harmonic mode of operation. The modulated signal from RF switch is passed down to a +30 dB power amplifier (MPA-10-40) that can be transmitted using the interrogator's respective antenna (915 MHz or 434 MHz). The tag in field-of-view reply to the interrogator's command accordingly, which is received using either a 915 MHz antenna or 868 MHz antenna, depends on the mode of operation. The received signal is amplified +25 dB using LNA (MAR-8ASM+) and fed into the RF PORT of an RF mixer. The RF mixer is part of the super heterodyning, required to precisely decouple the modulated information from the carrier wave. A secondary RF source (either 915 MHz or 868 MHz) is used to provide the signal at the LO PORT of the mixer. The digital information is further

extracted using a comparator and 1-bit translator, so that the processing unit can understand the signal and apply respective logic.

The interrogator transmits ‘Query’ command for the tags available in field-of-view, to respond. If an RF sensor tag (single or harmonic) responds with a ‘RN16’ to ‘Query’ command, the interrogator sends an ‘ACK’ command for asking for its ‘EPC’. If a tag receives the correct ‘ACK’, it responds with either digital ID-only or sensor integrated EPC. The interrogator checks the received EPC and decodes the digital data. The digital sensor data can be directly stored in the interrogator’s memory for later processing. The transmitted ‘Query’ command at 915 MHz and the demodulated received reply ‘RN16’ are shown in Fig.B.8.

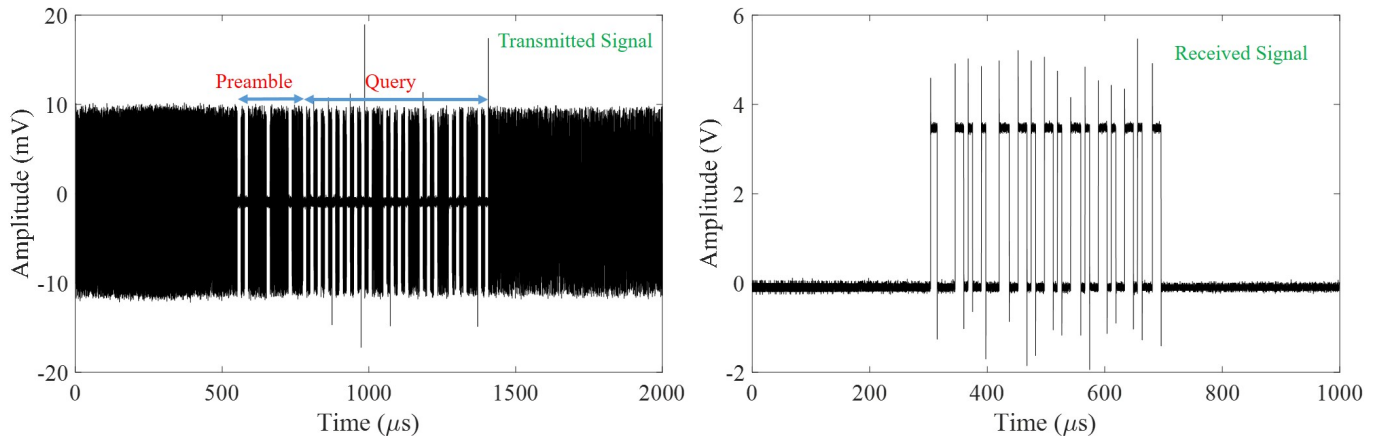


Figure B.8: (A) Modulated “Query” command on 915 MHz signal, (B) Demodulated received reply “RN16” from 915 MHz

The digital processes used for the interrogator is implemented on Raspberry Pi 3’s board with ARM microprocessor. A bare metal code is developed for modified EPC Gen2 interrogator protocol, that can send 6 mandatory commands (Query, QueryRep, QueryAdj, ACK, NAK and ReqRN). The code also controls the operating mode at single or harmonic frequency and set the correct switches for receiving 915 MHz or 868 MHz signal.

B.3 Wireless Communication Demonstration

First, the interrogator is turned on with an output power of +7 dBm at 915 MHz. The digital single-frequency RFID tag is placed 10 inches from the interrogator and communicated wirelessly

for both ID and sensor information. A variable voltage source is used to demonstrate the tag capabilities to digitize the sensor's signal and combine with the EPC data frame. The voltage change can imitate a resistive type temperature or pressure sensor that can be connected to a voltage divider circuit for acquisition.

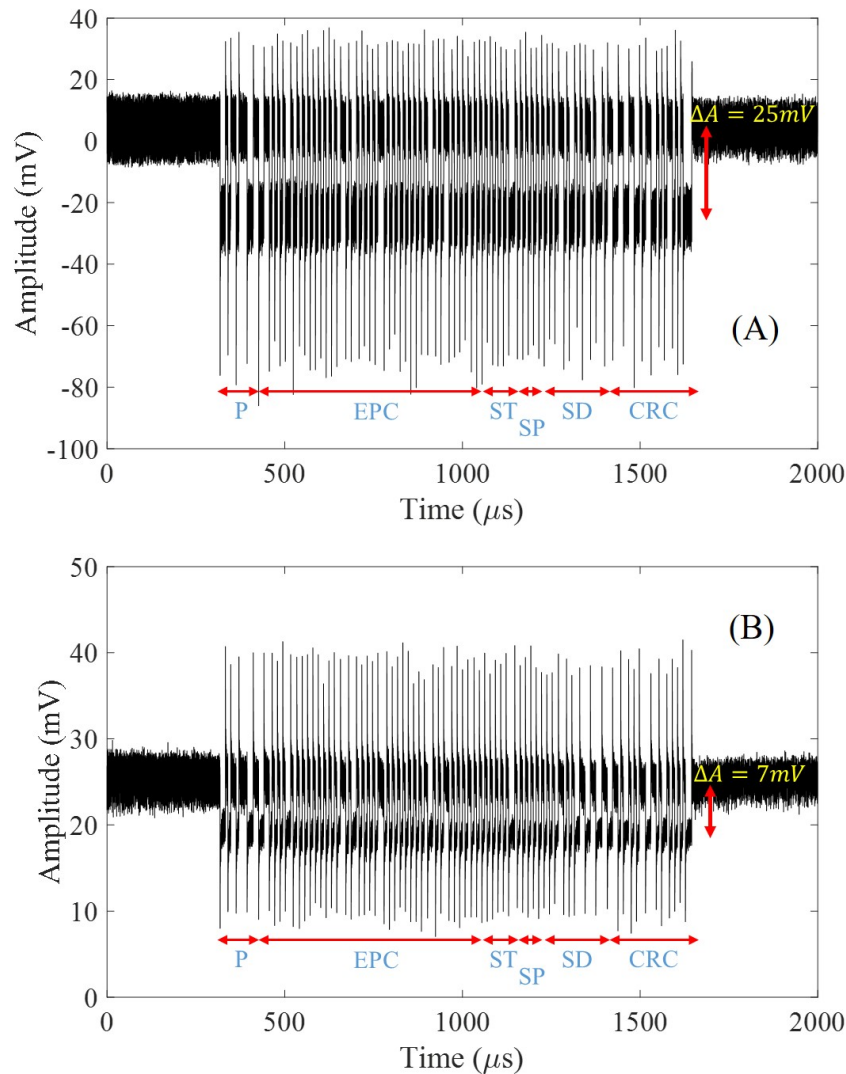


Figure B.9: Digital RFID data received at 915 MHz with +7 dBm transmitted power; (A) with 5 inch interrogation distance, (B) with 10 inch interrogation distance

The raw received EPC with sensor data is plotted in Fig.B.9. The two plots show the change in signal at the interrogator's receiver due to change in tag's distance. Fig.B.9A shows larger change in amplitude of the received signal due to higher received power at 5 inch separation.

The received signal is converted into bits using a comparator and the bit level is shifted to 3.3V for proper detection using the interrogator's microprocessor. The received data bits are decoded according to the width of 0's and 1's. Six different voltage values are applied to the tag from 0V to 1.0V at a step size of 0.2V. The interrogator decoded the values and gave a hex output as shown in Fig.B.10.

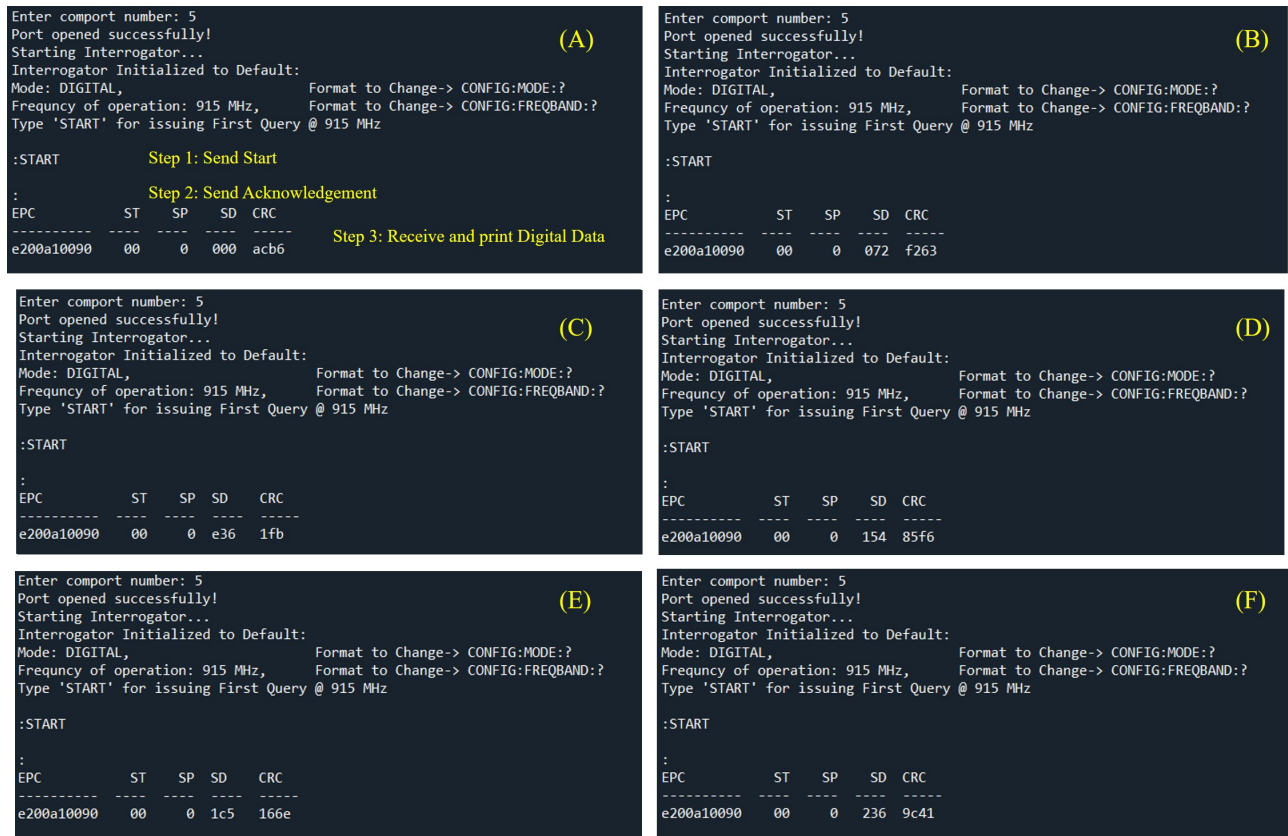


Figure B.10: Snapshots of tag and interrogator communication in digital single-frequency mode; (A) Decoded output with 0.0V at tag, (B) Decoded output with 0.2V at tag, (C) Decoded output with 0.4V at tag, (D) Decoded output with 0.6V at tag, (E) Decoded output with 0.8V at tag, (F) Decoded output with 1.0V at tag

The received hex values are plotted according to the known input voltage. The graph is shown in Fig.B.11.

The designed digital RFID tag successfully worked in single-frequency communication mode. The interrogator received the RFID tag signal and demodulated for extracting sensor's information. The digital sensor information is acquired and checked against the input parameter (voltage).

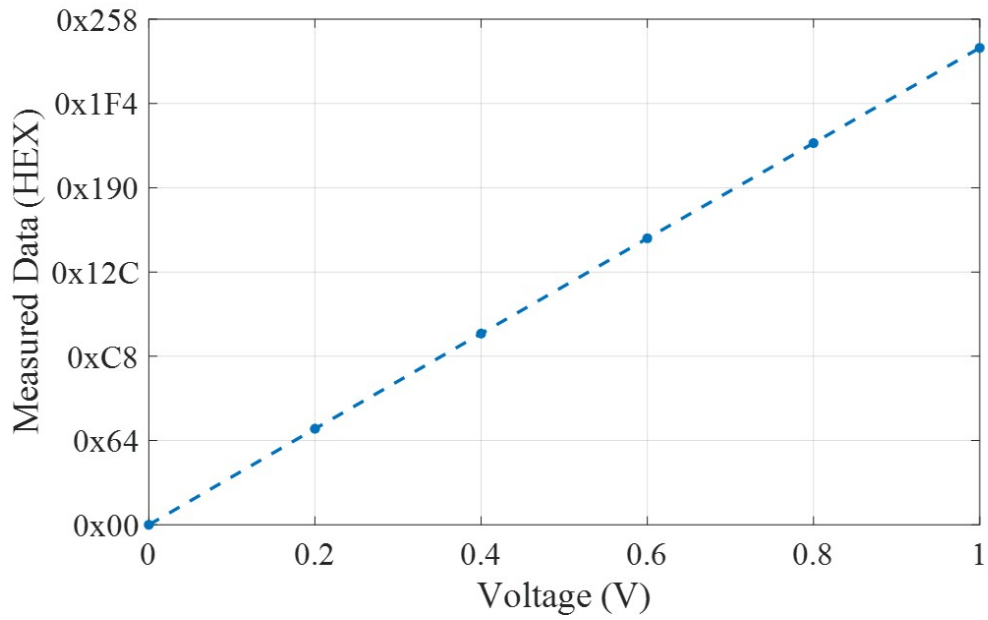


Figure B.11: Received digital sensor data at 915 MHz

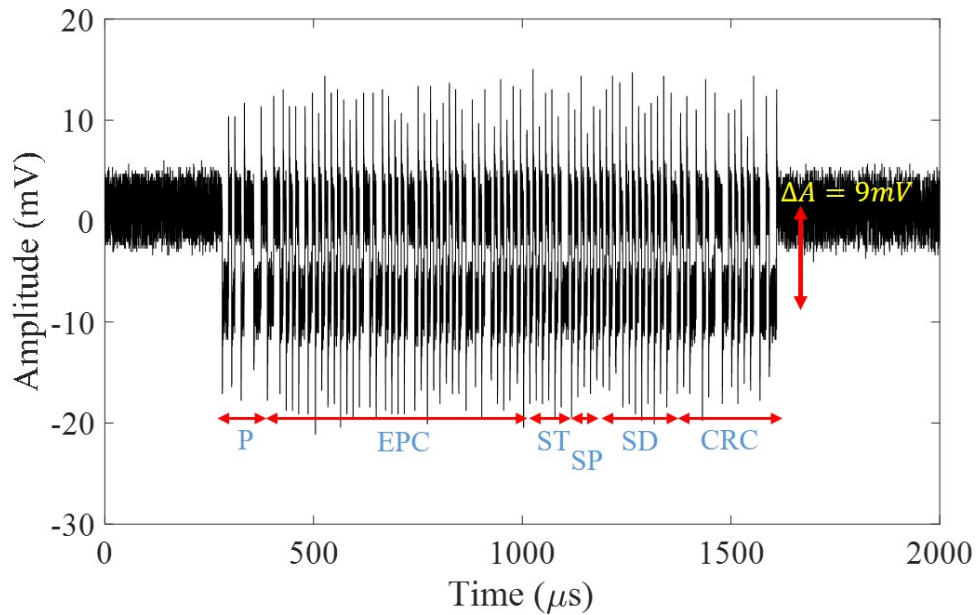


Figure B.12: Digital RFID data received at 868 MHz with +7 dBm transmitted power with 10 inch interrogation distance

Second, the interrogator is turned on with an output power of +7 dBm at 434 MHz. The digital harmonic-frequency RFID tag is placed 10 inches from the interrogator and communicated wirelessly. The variable voltage source is attached for imitating the sensor change, similar to previous experiments. The received signal at 868 MHz is demodulated using an RF mixer and the output is shown in Fig.B.12.

The received signal is converted into bits using a comparator and bit level shifter as before. The experiment with six different voltage values at the tag from 0V to 1.0V at a step size of 0.2V is repeated for harmonic-frequency RFID tag. The interrogator decoded the received values at 868 MHz and gave a hex output as shown in Fig.B.13.

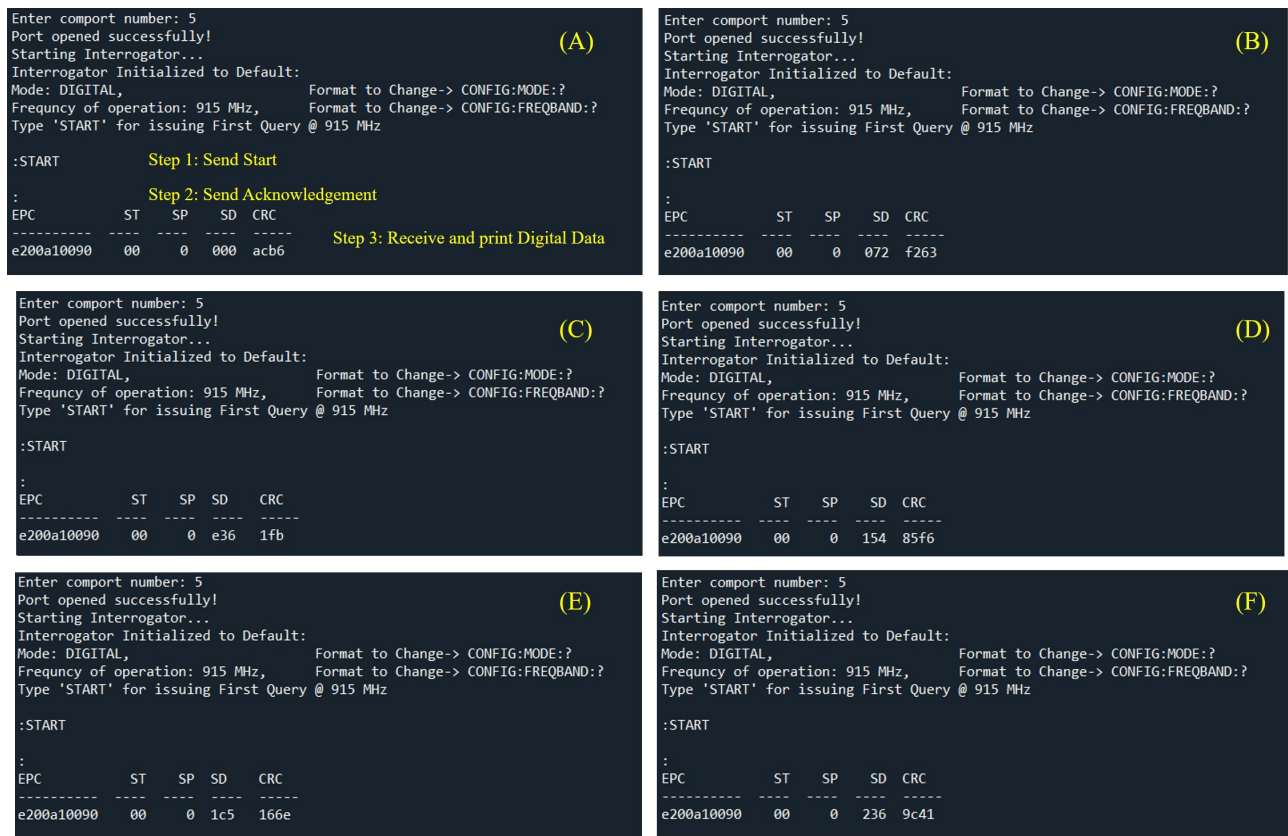


Figure B.13: Snapshots of tag and interrogator communication in digital harmonic-frequency mode; (A) Decoded output with 0.0V at tag, (B) Decoded output with 0.2V at tag, (C) Decoded output with 0.4V at tag, (D) Decoded output with 0.6V at tag, (E) Decoded output with 0.8V at tag, (F) Decoded output with 1.0V at tag

The received hex values are plotted according to the known input voltage. The graph is shown

in Fig.B.14.

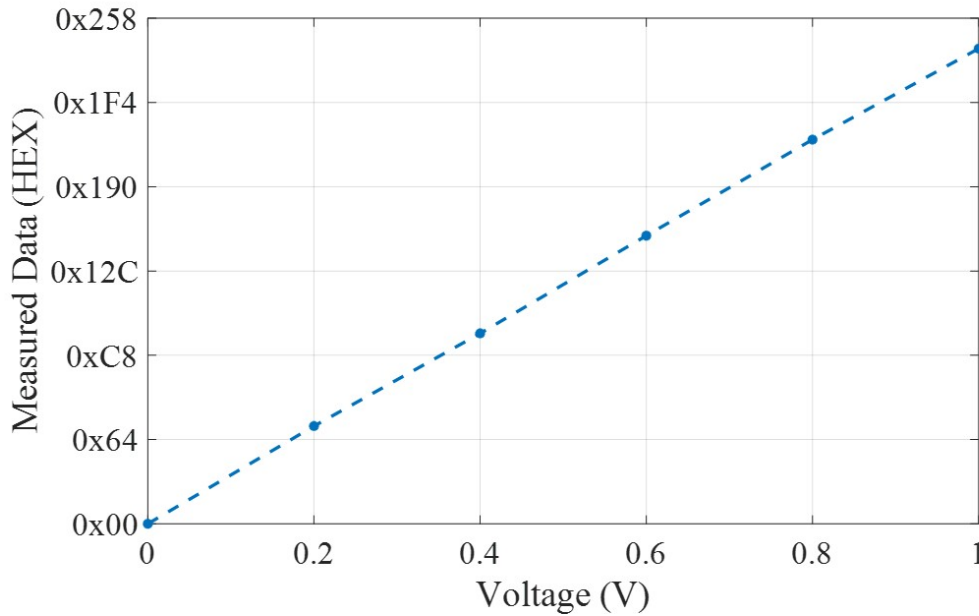


Figure B.14: Received digital sensor data at 868 MHz

The designed digital RFID tag successfully worked in harmonic-frequency communication mode. The interrogator received the RFID tag signal and demodulated for extracting sensor's information.

B.4 Summary

The battery-free wireless RFID communication using single and harmonic frequency operation is shown. The receiver with an energy harvester can power the microcontroller and demodulate the digital signal. The software for RFID tag works reliably and able to decode commands from the interrogator and respond accordingly. The tag software control the modulation switch for impedance mismatch and able to reflect back the ID and sensor information. ADC is used to digitize the sensor's information, which is combined with the tag's EPC and back-reflected to the interrogator.

The interrogator is able to transmit and receive digital signals at multiple frequencies. The receiver of the interrogator acquires the backscattered data from the digital RFID tags and decodes

ID and sensor information.

The multifrequency interrogator and tag implementation for digital battery-free communication is achieved. The well-known shortcomings of the conventional single frequency RFID communication are mitigated using harmonic operation.

BIBLIOGRAPHY

BIBLIOGRAPHY

- [1] X. Shi, V. T. Rathod, S. Mukherjee, L. Udpa, and Y. Deng, "Multi-modality strain estimation using a rapid near-field microwave imaging system for dielectric materials," *Measurement*, vol. 151, p. 107243, 2020. [Online]. Available: <https://www.sciencedirect.com/science/article/pii/S026322411931108X>
- [2] Z. Li, B. B. Shenoy, L. Udpa, and Y. Deng, "Magnetic Barkhausen Noise Technique for Early Stage Fatigue Prediction in Martensitic Stainless-Steel Samples (invited)," *Journal of Nondestructive Evaluation, Diagnostics and Prognostics of Engineering Systems*, pp. 1–18, 04 2021. [Online]. Available: <https://doi.org/10.1115/1.4050842>
- [3] S. Datta, X. Shi, S. Mukherjee, Y. Deng, and L. Udpa, "Model-Based Study of a Metamaterial Lens for Nondestructive Evaluation of Composites," *Journal of Nondestructive Evaluation, Diagnostics and Prognostics of Engineering Systems*, vol. 3, no. 4, 05 2020, 041001. [Online]. Available: <https://doi.org/10.1115/1.4047027>
- [4] M. Rautela, S. Gopalakrishnan, K. Gopalakrishnan, and Y. Deng, "Ultrasonic guided waves based identification of elastic properties using 1D-convolutional neural networks," in *2020 IEEE International Conference on Prognostics and Health Management (ICPHM)*, 2020, pp. 1–7.
- [5] D. Kumar, S. Karuppuswami, Y. Deng, and P. Chahal, "A wireless shortwave near-field probe for monitoring structural integrity of dielectric composites and polymers," *NDT & E International*, vol. 96, pp. 9–17, 2018. [Online]. Available: <https://www.sciencedirect.com/science/article/pii/S0963869517306886>
- [6] G. Piscitelli, A. C. Esposito, L. Faella, R. Prakash, and A. Tamburrino, "Monotonicity principle for nonlinear electrical conductivity tomography," *Inverse Problems*, dec 2020. [Online]. Available: <https://doi.org/10.1088/1361-6420/abd29a>
- [7] A. Tamburrino, G. Piscitelli, and Z. Zhou, "Monotonicity principle for magnetic induction tomography," 2020.
- [8] S. Karuppuswami, E. Rothwell, P. Chahal, and M. Havrilla, "A triaxial applicator for the measurement of the electromagnetic properties of materials," *Sensors*, vol. 18, no. 2, 2018. [Online]. Available: <https://www.mdpi.com/1424-8220/18/2/383>
- [9] G. Webb, P. Vardanega, and C. Middleton, "Categories of SHM deployments: technologies and capabilities," *Journal of Bridge Engineering*, vol. 20, no. 11, p. 04014118, 2014.
- [10] G. Song, C. Wang, and B. Wang, "Structural health monitoring (SHM) of civil structures," *Applied Sciences*, vol. 7, no. 8, 2017. [Online]. Available: <http://www.mdpi.com/2076-3417/7/8/789>
- [11] A. News. (2018) Miami bridge collapse. [Online]. Available: <https://6abc.com/6-dead-10-injured-after-bridge-collapse-at-florida-intl-univ/3220344/>

- [12] R. Insider. (2018) Railway bridge collapse. [Online]. Available: <https://www.romania-insider.com/floods-romania-june-2018/>
- [13] T13. (2018) Cancura bridge collapse. [Online]. Available: <http://www.t13.cl/noticia/nacional/colapso-puente-cancura-deja-muerto-y-seis-heridos>
- [14] T. telegraph. (2018) Calcutta bridge collapse. [Online]. Available: <https://www.telegraphindia.com/india/no-room-for-repairs-complains-mamata/cid/1666742>
- [15] PHMSA. (2018) Pipeline failures. [Online]. Available: <https://www.phmsa.dot.gov/data-and-statistics/pipeline/pipeline-incident-20-year-trends>
- [16] NTSB. (2018) Pipeline failures. [Online]. Available: <https://www.nts.gov/investigations/AccidentReports/Pages/pipeline.aspx>
- [17] H. News. (2017) Natural gas leak. [Online]. Available: <https://www.hcn.org/issues/49.22/infographic-a-map-of-leaking-natural-gas-pipelines-across-the-nation>
- [18] C. R. Farrar and K. Worden, “An introduction to structural health monitoring,” *Philosophical Transactions of the Royal Society A: Mathematical, Physical and Engineering Sciences*, vol. 365, no. 1851, pp. 303–315, 2006.
- [19] D. Kumar, S. Mondal, A. Kaur, Y. Deng, and P. Chahal, “An RF backscatterer system for real-time multi-sensing applications,” *Sensors and Actuators A: Physical*, vol. 303, p. 111685, 2020. [Online]. Available: <https://www.sciencedirect.com/science/article/pii/S0924424719307162>
- [20] D. Kumar and Y. Deng, “An efficient multisensing system for SHM of oil and gas pipelines,” *Review of Progress in Quantitative Nondestructive Evaluation*, vol. 46, 2019. [Online]. Available: <https://www.iastatedigitalpress.com/qnde/article/id/8571>
- [21] C. Kralovec and M. Schagerl, “Review of structural health monitoring methods regarding a multi-sensor approach for damage assessment of metal and composite structures,” *Sensors*, vol. 20, no. 3, 2020. [Online]. Available: <https://www.mdpi.com/1424-8220/20/3/826>
- [22] H. Ahmed, H. M. La, and N. Gucunski, “Review of non-destructive civil infrastructure evaluation for bridges: State-of-the-art robotic platforms, sensors and algorithms,” *Sensors*, vol. 20, no. 14, 2020. [Online]. Available: <https://www.mdpi.com/1424-8220/20/14/3954>
- [23] J. Zheng, Y. Zhang, D. Hou, Y. Qin, W. Guo, C. Zhang, and J. Shi, “A review of nondestructive examination technology for polyethylene pipe in nuclear power plant,” *Frontiers of Mechanical Engineering*, vol. 13, no. 4, 2018. [Online]. Available: <https://doi.org/10.1007/s11465-018-0515-9>
- [24] S. Abbas, F. Li, and J. Qiu, “A review on shm techniques and current challenges for characteristic investigation of damage in composite material components of aviation industry,” *Materials Performance and Characterization*, vol. 7, no. 1, pp. 224–258, 2018. [Online]. Available: <https://doi.org/10.1520/MPC20170167>

- [25] W. Ostachowicz, R. Soman, and P. Malinowski, "Optimization of sensor placement for structural health monitoring: A review," *Structural Health Monitoring*, vol. 18, no. 3, pp. 963–988, 2019. [Online]. Available: <https://doi.org/10.1177/1475921719825601>
- [26] H. Rocha, C. Semprimoschnig, and J. P. Nunes, "Sensors for process and structural health monitoring of aerospace composites: A review," *Engineering Structures*, vol. 237, p. 112231, 2021. [Online]. Available: <https://www.sciencedirect.com/science/article/pii/S0141029621003813>
- [27] Z. H. Warsi, S. M. Irshad, F. Khan, M. A. Shahbaz, M. Junaid, and S. U. Amin, "Sensors for structural health monitoring: A review," in *2019 Second International Conference on Latest trends in Electrical Engineering and Computing Technologies (INTELLECT)*, 2019, pp. 1–6.
- [28] S. Mukherjee, L. Udpa, S. Udpa, E. J. Rothwell, and Y. Deng, "A time reversal-based microwave imaging system for detection of breast tumors," *IEEE Transactions on Microwave Theory and Techniques*, vol. 67, no. 5, pp. 2062–2075, 2019.
- [29] R. Jacobs, M. Alzuhiri, M. Golkowski, and Y. Deng, "Low-power microwave induced thermoacoustic imaging: Experimental study and hybrid fem modeling," *Progress In Electromagnetics Research*, vol. 91, pp. 265–277, 2019.
- [30] S. Mondal, S. Karuppuswami, R. Steinhorst, and P. Chahal, "A wearable passive pH sensor for health monitoring," in *2019 IEEE 69th Electronic Components and Technology Conference (ECTC)*, 2019, pp. 1240–1245.
- [31] S. Mukherjee, X. Shi, L. Udpa, S. Udpa, Y. Deng, and P. Chahal, "Design of a split-ring resonator sensor for near-field microwave imaging," *IEEE Sensors Journal*, vol. 18, no. 17, pp. 7066–7076, 2018.
- [32] C. Liu, M. Al Qaseer, and R. Zoughi, "Wideband double-ridged TEM horn for nondestructive evaluation and imaging applications," in *2020 Antenna Measurement Techniques Association Symposium (AMTA)*, 2020, pp. 1–4.
- [33] K. Brinker, M. Dvorsky, M. T. Al Qaseer, and R. Zoughi, "Review of advances in microwave and millimetre-wave NDT&E: principles and applications," *Philosophical Transactions of the Royal Society A*, vol. 378, no. 2182, p. 20190585, 2020.
- [34] M. T. Ghasr, Y. Gao, and R. Zoughi, "Handheld microwave imaging system for the inspection of non-metallic structures," *Review of Progress in Quantitative Nondestructive Evaluation*, 2019.
- [35] I. Mehdipour, R. Zoughi, and K. H. Khayat, "Feasibility of using near-field microwave reflectometry for monitoring autogenous crack healing in cementitious materials," *Cement and Concrete Composites*, vol. 85, pp. 161–173, 2018. [Online]. Available: <https://www.sciencedirect.com/science/article/pii/S0958946517305565>
- [36] R. Kumar, J. H. Lang, T. Hamer, and D. L. Trumper, "Towards high-bandwidth capacitive imaging," in *2016 IEEE SENSORS*, 2016, pp. 1–3.

- [37] A. Jacques, "Q factor measurements on L-C circuits," *Amateur Radio in Space (AMSAT)*, p. 11, 2012. [Online]. Available: http://ve2azx.net/technical/Q-FactorMeas_on_LC_Circuits.pdf
- [38] S. G. Taylor, E. Y. Raby, K. M. Farinholt, G. Park, and M. D. Todd, "Active-sensing platform for structural health monitoring: Development and deployment," *Structural Health Monitoring*, vol. 15, no. 4, pp. 413–422, 2016. [Online]. Available: <https://doi.org/10.1177/1475921716642171>
- [39] N. A. Tanner, J. R. Wait, C. R. Farrar, and H. Sohn, "Structural health monitoring using modular wireless sensors," *Journal of Intelligent Material Systems and Structures*, vol. 14, no. 1, pp. 43–56, 2003. [Online]. Available: <https://doi.org/10.1177/1045389X03014001005>
- [40] E. Yasar and Y. Erdogan, "Correlating sound velocity with the density, compressive strength and young's modulus of carbonate rocks," *International Journal of Rock Mechanics and Mining Sciences*, vol. 41, no. 5, pp. 871–875, 2004.
- [41] S. Mondal, K. P. Wijewardena, S. Karuppuswami, N. Kriti, D. Kumar, and P. Chahal, "Blockchain inspired rfid-based information architecture for food supply chain," *IEEE Internet of Things Journal*, vol. 6, no. 3, pp. 5803–5813, 2019.
- [42] S. Cho, C.-B. Yun, J. Lynch, A. Zimmerman, B. Spencer, and T. Nagayama, "Smart wireless sensor technology for structural health monitoring of civil structures," *Steel Structures*, vol. 8, pp. 267–275, 01 2004.
- [43] S. Karuppuswami, S. Mondal, D. Kumar, and P. Chahal, "A compact wireless passive breath analyzer for health monitoring," in *2020 IEEE 70th Electronic Components and Technology Conference (ECTC)*, 2020, pp. 1010–1015.
- [44] P. Chahal, D. Kumar, S. Mondal, and S. Karuppuswami, "Systems and methods for a multiband sensing platform," May 28 2020, uS Patent App. 16/695,758.
- [45] R. Nopper, R. Niekrawietz, and L. Reindl, "Wireless readout of passive LC sensors," *IEEE Transactions on Instrumentation and Measurement*, vol. 59, no. 9, pp. 2450–2457, 2010.
- [46] S. Karuppuswami, L. L. Matta, E. C. Alocilja, and P. Chahal, "A wireless RFID compatible sensor tag using gold nanoparticle markers for pathogen detection in the liquid food supply chain," *IEEE Sensors Letters*, vol. 2, no. 2, pp. 1–4, 2018.
- [47] A. Deivasigamani, A. Daliri, C. H. Wang, and S. John, "A review of passive wireless sensors for structural health monitoring," *Modern Applied Science*, vol. 7, no. 2, p. 57, 2013.
- [48] H. Shen, L. Li, and Y. Zhou, "Fully integrated passive UHF RFID tag with temperature sensor for environment monitoring," in *ASIC, 2007. ASICON'07. 7th International Conference on. IEEE*, 2007, pp. 360–363.
- [49] *SL900A EPC Class 3 Sensory Tag Chip - For Automatic Data Logging*, AMS, 10 2018, rev. 1.12.

- [50] A. P. Sample, D. J. Yeager, P. S. Powledge, A. V. Mamishev, J. R. Smith *et al.*, “Design of an RFID-based battery-free programmable sensing platform,” *IEEE transactions on instrumentation and measurement*, vol. 57, no. 11, p. 2608, 2008.
- [51] Y. Su, A. Wickramasinghe, and D. C. Ranasinghe, “Investigating sensor data retrieval schemes for multi-sensor passive rfid tags,” in *2015 IEEE International Conference on RFID (RFID)*, April 2015, pp. 158–165.
- [52] S. Mondal, D. Kumar, and P. Chahal, “A continuous-mode single-antenna harmonic rfid tag,” *IEEE Microwave and Wireless Components Letters*, vol. 30, no. 4, pp. 441–444, 2020.
- [53] S. Karuppuswami, S. Mondal, D. Kumar, and P. Chahal, “Rfid coupled passive digital ammonia sensor for quality control of packaged food,” *IEEE Sensors Journal*, vol. 20, no. 9, pp. 4679–4687, 2020.
- [54] S. Mondal, S. Karuppuswami, D. Kumar, A. Kaur, and P. Chahal, “A miniaturized dual band antenna for harmonic rfid tag,” in *International Symposium on Microelectronics*, vol. 2019, no. 1. International Microelectronics Assembly and Packaging Society, 2019, pp. 000 033–000 036.
- [55] S. Mondal, D. Kumar, M. I. Ghazali, P. Chahal, L. Udpa, and Y. Deng, “Monitoring and localization of buried plastic natural gas pipes using passive rf tags,” in *AIP Conference Proceedings*, vol. 1949, no. 1. AIP Publishing LLC, 2018, p. 020020.
- [56] I. Amenabar, A. Mendikute, A. López-Arraiza, M. Lizaranzu, and J. Aurrekoetxea, “Comparison and analysis of non-destructive testing techniques suitable for delamination inspection in wind turbine blades,” *Composites Part B: Engineering*, vol. 42, no. 5, pp. 1298 – 1305, 2011. [Online]. Available: <http://www.sciencedirect.com/science/article/pii/S1359836811000539>
- [57] P. A. Joosse, M. J. Blanch, A. G. Dutton, D. A. Kouroussis, T. P. Philippidis, and P. S. Vionis, “Acoustic emission monitoring of small wind turbine blades,” *Journal of Solar Energy Engineering*, vol. 124, no. 4, pp. 446–454, 2002.
- [58] R. A. Raišutis, E. Jasiūnienė, and E. Žukauskas, “Ultrasonic NDT of wind turbine blades using guided waves,” *Ultragarsas*, vol. 63, no. 1, pp. 7–11, 2008.
- [59] R. Raišutis, E. Jasiūnienė, R. Šlitteris, and A. Vladišauskas, “The review of non-destructive testing techniques suitable for inspection of the wind turbine blades,” *Ultragarsas" Ultrasound"*, vol. 63, no. 2, pp. 26–30, 2008.
- [60] Z. Li, C. Soutis, A. Haigh, R. Sloan, A. Gibson, and N. Karimian, “Microwave imaging for delamination detection in T-joints of wind turbine composite blades,” in *2016 46th European Microwave Conference (EuMC)*, Oct 2016, pp. 1235–1238.
- [61] D. Palumbo, R. Tamborrino, U. Galietti, P. Aversa, A. Tatì, and V. Luprano, “Ultrasonic analysis and lock-in thermography for debonding evaluation of composite adhesive joints,” *NDT E International*, vol. 78, no. Supplement C, pp. 1 – 9, 2016. [Online]. Available: <http://www.sciencedirect.com/science/article/pii/S0963869515000985>

- [62] C. Meola, S. Boccardi, G. Carlomagno, N. Boffa, F. Ricci, G. Simeoli, and P. Russo, “Impact damaging of composites through online monitoring and non-destructive evaluation with infrared thermography,” *NDT E International*, vol. 85, no. Supplement C, pp. 34 – 42, 2017. [Online]. Available: <http://www.sciencedirect.com/science/article/pii/S0963869516301323>
- [63] C. C. Ciang, J.-R. Lee, and H.-J. Bang, “Structural health monitoring for a wind turbine system: a review of damage detection methods,” *Measurement Science and Technology*, vol. 19, no. 12, p. 122001, 2008. [Online]. Available: <http://stacks.iop.org/0957-0233/19/i=12/a=122001>
- [64] G. S. Park and E. S. Park, “Improvement of the sensor system in magnetic flux leakage-type nondestructive testing (NDT),” *IEEE Transactions on Magnetics*, vol. 38, no. 2, pp. 1277–1280, Mar 2002.
- [65] N. V. Nair, V. R. Melapudi, H. R. Jimenez, X. Liu, Y. Deng, Z. Zeng, L. Udpa, T. J. Moran, and S. S. Udpa, “A gmr-based eddy current system for nde of aircraft structures,” *IEEE Transactions on Magnetics*, vol. 42, no. 10, pp. 3312–3314, Oct 2006.
- [66] Y. Xiong, Z. Liu, C. Sun, and X. Zhang, “Two-dimensional imaging by far-field superlens at visible wavelengths,” *Nano Letters*, vol. 7, no. 11, pp. 3360–3365, 2007, pMID: 17918904. [Online]. Available: <http://dx.doi.org/10.1021/nl0716449>
- [67] D. F. Pieper and K. M. Donnell, “Application of frequency selective surfaces for inspection of layered structures,” in *2015 IEEE International Instrumentation and Measurement Technology Conference (I2MTC) Proceedings*, May 2015, pp. 1204–1209.
- [68] J. W. Pang and I. P. Bond, “A hollow fibre reinforced polymer composite encompassing self-healing and enhanced damage visibility,” *Composites Science and Technology*, vol. 65, no. 11, pp. 1791 – 1799, 2005. [Online]. Available: <http://www.sciencedirect.com/science/article/pii/S0266353805000783>
- [69] F. Yan, j. Roger L. Royer, and J. L. Rose, “Ultrasonic guided wave imaging techniques in structural health monitoring,” *Journal of Intelligent Material Systems and Structures*, vol. 21, no. 3, pp. 377–384, 2010.
- [70] S. Karuppuswami, A. Kaur, M. I. M. Ghazali, and P. Chahal, “RFID compatible sensor tags for remote liquid sample interrogation,” in *2016 IEEE 66th Electronic Components and Technology Conference (ECTC)*, May 2016, pp. 2401–2407.
- [71] S. Karuppuswami, N. Wiwatcharagoses, A. Kaur, and P. Chahal, “Capillary condensation based wireless volatile molecular sensor,” in *2017 IEEE 67th Electronic Components and Technology Conference (ECTC)*, May 2017, pp. 1455–1460.
- [72] S. Karuppuswami, A. Kaur, H. Arangali, and P. P. Chahal, “A hybrid magnetoelastic wireless sensor for detection of food adulteration,” *IEEE Sensors Journal*, vol. 17, no. 6, pp. 1706–1714, March 2017.

- [73] S. Karuppuswami, H. Arangali, and P. Chahal, "A hybrid electrical-mechanical wireless magnetoelastic sensor for liquid sample measurements," in *2016 IEEE 66th Electronic Components and Technology Conference (ECTC)*, May 2016, pp. 2535–2540.
- [74] N. Wiwatcharagoses, K. Y. Park, and P. Chahal, "Metamaterial-inspired sensor on porous substrate for detection of volatile organic compounds in air," in *2016 IEEE 66th Electronic Components and Technology Conference (ECTC)*, May 2016, pp. 1557–1562.
- [75] W. B. Weir, "Automatic measurement of complex dielectric constant and permeability at microwave frequencies," *Proceedings of the IEEE*, vol. 62, no. 1, pp. 33–36, Jan 1974.
- [76] R. Luebbers, "Lossy dielectrics in fdfd," *IEEE Transactions on Antennas and Propagation*, vol. 41, no. 11, pp. 1586–1588, Nov 1993.
- [77] S. Chisca, I. Sava, V. E. Musteata, and M. Bruma, "Dielectric and conduction properties of polyimide films," in *CAS 2011 Proceedings (2011 International Semiconductor Conference)*, vol. 2, Oct 2011, pp. 253–256.
- [78] B. Riddle, J. Baker-Jarvis, and J. Krupka, "Complex permittivity measurements of common plastics over variable temperatures," *IEEE Transactions on Microwave theory and techniques*, vol. 51, no. 3, pp. 727–733, 2003.
- [79] K. Naito, Y. Kagawa, S. Utsuno, T. Naganuma, and K. Kurihara, "Dielectric properties of eight-harness-stain fabric glass fiber reinforced polyimide matrix composite in the THz frequency range," *NDTE International*, vol. 42, no. 5, pp. 441 – 445, 2009.
- [80] J. Landt, "The history of RFID," *IEEE potentials*, vol. 24, no. 4, pp. 8–11, 2005.
- [81] F. Wu, F. Kuo, and L.-W. Liu, "The application of RFID on drug safety of inpatient nursing healthcare," in *Proceedings of the 7th international conference on Electronic commerce*. ACM, 2005, pp. 85–92.
- [82] B. Yan and G. Huang, "Application of RFID and internet of things in monitoring and anti-counterfeiting for products," in *Business and Information Management, 2008. ISBIM'08. International Seminar on*, vol. 1. IEEE, 2008, pp. 392–395.
- [83] M. Buettner, R. Prasad, M. Philipose, and D. Wetherall, "Recognizing daily activities with RFID-based sensors," in *Proceedings of the 11th international conference on Ubiquitous computing*. ACM, 2009, pp. 51–60.
- [84] D. Delen, R. Sharda, and B. C. Hardgrave, "The promise of RFID-based sensors in the perishables supply chain," *IEEE Wireless Communications*, vol. 18, no. 2, 2011.
- [85] K. S. Rao, P. V. Nikitin, and S. F. Lam, "Antenna design for UHF RFID tags: A review and a practical application," *IEEE Transactions on antennas and propagation*, vol. 53, no. 12, pp. 3870–3876, 2005.
- [86] Y. Ma, X. Hui, and E. C. Kan, "Harmonic-wisp: A passive broadband harmonic RFID platform," in *Microwave Symposium (IMS), 2016 IEEE MTT-S International*. IEEE, 2016, pp. 1–4.

- [87] S. Mondal and P. Chahal, "A passive harmonic RFID tag and interrogator development," *IEEE Journal of Radio Frequency Identification*, vol. 3, no. 2, pp. 98–107, June 2019.
- [88] A. Boaventura, J. Santos, A. Oliveira, and N. B. Carvalho, "Perfect isolation: Dealing with self-jamming in passive RFID systems," *IEEE Microwave Magazine*, vol. 17, no. 11, pp. 20–39, 2016.
- [89] M. Sajid and S. Chiu, "Canceling self-jammer and interfering signals in an RFID system," Aug. 16 2011, US Patent 8,000,674.
- [90] S. Tedjini, Y. Duroc, G. A. Vera, C. Loussert, and M. Recouly, "RFID communication system," Sep. 27 2016, US Patent 9,455,769.
- [91] I. Mayordomo and J. Bernhard, "Implementation of an adaptive leakage cancellation control for passive uhf RFID readers," in *RFID (RFID), 2011 IEEE International Conference on*. IEEE, 2011, pp. 121–127.
- [92] R. Rimini, P. D. Heidmann, and J. P. Burke, "Method and apparatus for adaptive non-linear self-jamming interference cancellation," Jun. 3 2014, US Patent 8,744,377.
- [93] M. I. M. Ghazali, S. Karuppuswami, and P. Chahal, "3-D printed embedded passive harmonic sensor tag as markers for buried assets localization," *IEEE Sensors Letters*, vol. 3, no. 4, pp. 1–4, April 2019.
- [94] S. Mondal, D. Kumar, and P. Chahal, "A wireless passive pH sensor with clutter rejection scheme," *IEEE Sensors Journal*, vol. 19, no. 9, pp. 3399–3407, May 2019.
- [95] H. Huang, P.-Y. Chen, C.-H. Hung, R. Gharpurey, and D. Akinwande, "Frequency hopped wireless passive sensing system with harmonic transponder antenna sensor," in *Microwave Symposium (IMS), 2015 IEEE MTT-S International*. IEEE, 2015, pp. 1–4.
- [96] K. Rasilainen, J. Ilvonen, A. Lehtovuori, J.-M. Hannula, and V. Viikari, "On design and evaluation of harmonic transponders," *IEEE Transactions on Antennas and Propagation*, vol. 63, no. 1, pp. 15–23, 2015.
- [97] P. V. Nikitin and K. Rao, "Harmonic scattering from passive UHF RFID tags," in *Antennas and Propagation Society International Symposium, 2009. APSURSI'09. IEEE*. IEEE, 2009, pp. 1–4.
- [98] G. A. Vera, Y. Duroc, and S. Tedjini, "RFID test platform: Nonlinear characterization," *IEEE Transactions on Instrumentation and Measurement*, vol. 63, no. 9, pp. 2299–2305, 2014.
- [99] G. Vera, Y. Duroc, and S. Tedjini, "Analysis of harmonics in UHF RFID signals," *IEEE Transactions on Microwave Theory and Techniques*, vol. 61, no. 6, pp. 2481–2490, 2013.
- [100] G. A. Vera, Y. Duroc, and S. Tedjini, "Tag-to-reader harmonic link in passive UHF RFID," in *Microwave Symposium (IMS), 2014 IEEE MTT-S International*. IEEE, 2014, pp. 1–4.

- [101] G. A. Vera, S. D. Nawale, Y. Duroc, and S. Tedjini, “Read range enhancement by harmonic energy harvesting in passive UHF RFID,” *IEEE Microwave and Wireless Components Letters*, vol. 25, no. 9, pp. 627–629, 2015.
- [102] D. Allane, G. A. Vera, Y. Duroc, R. Touhami, and S. Tedjini, “Harmonic power harvesting system for passive RFID sensor tags,” *IEEE Transactions on Microwave Theory and Techniques*, vol. 64, no. 7, pp. 2347–2356, 2016.
- [103] D. Allane, Y. Duroc, G. A. Vera, R. Touhami, and S. Tedjini, “On energy harvesting for augmented tags,” *Comptes Rendus Physique*, vol. 18, no. 2, pp. 86–97, 2017.
- [104] *Higgs® 3, ALC-360-SOT*, Alien Technology, LLC, 11 2016.
- [105] N. Pillin, C. Dehollain, and M. J. Declercq, “Read range limitation in if-based far-field RFID using ASK backscatter modulation,” in *2009 Ph.D. Research in Microelectronics and Electronics*, July 2009, pp. 348–351.
- [106] D. Kuester and Z. Popovic, “How good is your tag?: RFID backscatter metrics and measurements,” *IEEE Microwave Magazine*, vol. 14, no. 5, pp. 47–55, July 2013.
- [107] S. Mondal, M. I. M. Ghazali, S. Karuppuswami, A. Kaur, and P. Chahal, “A nonlinear transmission line based harmonic RF tag,” in *2017 IEEE 67th Electronic Components and Technology Conference (ECTC)*, May 2017, pp. 2237–2242.
- [108] G. Andia, Y. Duroc, and S. Tedjini, *Non-Linearities in Passive RFID Systems: Third Harmonic Concept and Applications*. John Wiley & Sons, 2018.
- [109] H. Cho, Y.-W. Seo, B. V. Kumar, and R. R. Rajkumar, “A multi-sensor fusion system for moving object detection and tracking in urban driving environments,” in *2014 IEEE International Conference on Robotics and Automation (ICRA)*. IEEE, 2014, pp. 1836–1843.
- [110] C. Tang, H. F. Rashvand, G. Y. Tian, P. Hu, A. I. Sunny, and H. Wang, “Structural health monitoring with WSNs,” *Wireless Sensor Systems for Extreme Environments: Space, Underwater, Underground, and Industrial*, pp. 383–408, 2017.
- [111] US-EIA, *Outlook for future emissions*, 2018. [Online]. Available: https://www.eia.gov/energyexplained/index.php?page=environment_outlook_for_emissions
- [112] S. K. Rajah and S. Nasr, “Longitudinal stresses in pressure pipeline design—A critical review,” *Pipelines 2008: Pipeline Asset Management: Maximizing Performance of our Pipeline Infrastructure*, pp. 1–12, 2008.
- [113] X. Wu, H. Lu, and S. Wu, “Stress analysis of parallel oil and gas steel pipelines in inclined tunnels,” *SpringerPlus*, vol. 4, no. 1, pp. 1–25, 2015.
- [114] J. Makar, R. Rogge, and S. McDonald, “Circumferential failures in grey cast iron pipes,” in *Proceedings of the AWWA Infrastructure Conference, Chicago, IL, USA*. Citeseer, 2002, pp. 10–13.

- [115] Z. Liu and Y. Kleiner, “State-of-the-art review of technologies for pipe structural health monitoring,” *IEEE Sensors Journal*, vol. 12, no. 6, pp. 1987–1992, June 2012.
- [116] A. M. Obeid, F. Karray, M. W. Jmal, M. Abid, S. M. Qasim, and M. S. BenSaleh, “Towards realisation of wireless sensor network-based water pipeline monitoring systems: a comprehensive review of techniques and platforms,” *IET Science, Measurement Technology*, vol. 10, no. 5, pp. 420–426, 2016.
- [117] J. Weber, J. Shi, and C. Zhang, “Embedded capacitance sensor array for structural health monitoring of pipeline systems,” *ASME Pressure Vessels and Piping Conference*, vol. 5, 2017.
- [118] H. Qingmin, R. Liang, J. Wenling, Z. Pinghua, and S. Gangbing, “An improved negative pressure wave method for natural gas pipeline leak location using fbg based strain sensor and wavelet transform,” *Mathematical Problems in Engineering*, vol. 2013, p. 8, 2013.
- [119] M. Jang and K.-S. Yun, “Mems capacitive pressure sensor monolithically integrated with cmos readout circuit by using post CMOS processes,” *Micro and Nano Systems Letters*, vol. 5, no. 1, p. 4, 2017.
- [120] M. I. M. Ghazali, *Additive Manufacturing for Electronic Systems (AMES)*. Michigan State University. Electrical Engineering, 2019.
- [121] C. Hong, Y. Zhang, and L. Borana, “Design, fabrication and testing of a 3d printed fbg pressure sensor,” *IEEE Access*, vol. 7, pp. 38 577–38 583, 2019.
- [122] J. Park, J.-K. Kim, D.-S. Kim, A. Shanmugasundaram, S. A. Park, S. Kang, S.-H. Kim, M. H. Jeong, and D.-W. Lee, “Wireless pressure sensor integrated with a 3d printed polymer stent for smart health monitoring,” *Sensors and Actuators B: Chemical*, vol. 280, pp. 201 – 209, 2019. [Online]. Available: <http://www.sciencedirect.com/science/article/pii/S0925400518317696>
- [123] J. Yoon, B. Choi, Y. Lee, J. Han, J. Lee, J. Park, Y. Kim, D. M. Kim, D. H. Kim, M. Kang, S. Kim, and S. Choi, “Monolithically 3d-printed pressure sensors for application in electronic skin and healthcare monitoring,” in *2017 IEEE International Electron Devices Meeting (IEDM)*, 2017, pp. 40.2.1–40.2.4.
- [124] M. Cattani, C. A. Boano, D. Steffelbauer, S. Kaltenbacher, M. Günther, K. Römer, D. Fuchs-Hanusch, and M. Horn, “Adige: An efficient smart water network based on long-range wireless technology,” in *Proceedings of the 3rd International Workshop on Cyber-Physical Systems for Smart Water Networks*, ser. CySWATER ’17. New York, NY, USA: ACM, 2017, pp. 3–6. [Online]. Available: <http://doi.acm.org/10.1145/3055366.3055367>
- [125] A. M. Sadeghioon, N. Metje, D. Chapman, and C. Anthony, “Water pipeline failure detection using distributed relative pressure and temperature measurements and anomaly detection algorithms,” *Urban Water Journal*, vol. 15, no. 4, pp. 287–295, 2018. [Online]. Available: <https://doi.org/10.1080/1573062X.2018.1424213>

- [126] A. B. Noel, A. Abdaoui, T. Elfouly, M. H. Ahmed, A. Badawy, and M. S. Shehata, "Structural health monitoring using wireless sensor networks: A comprehensive survey," *IEEE Communications Surveys Tutorials*, vol. 19, no. 3, pp. 1403–1423, thirdquarter 2017.
- [127] J.-H. Kim, G. Sharma, N. Boudriga, S. Iyengar, and N. Prabakar, "Autonomous pipeline monitoring and maintenance system: A RFID-based approach," *EURASIP Journal on Wireless Communications and Networking*, vol. 2015, no. 1, p. 262, Dec 2015. [Online]. Available: <https://doi.org/10.1186/s13638-015-0495-y>
- [128] S. Mondal, K. Wijewardena, S. Karrapuswami, D. Kumar, P. Chahal, M. Ghannam, and M. Cuddihy, "A wireless battery-less seat sensor for autonomous vehicles," in *2020 IEEE 70th Electronic Components and Technology Conference (ECTC)*, 2020, pp. 2289–2294.
- [129] L. Lin, M. Ma, F. Zhang, F. Liu, Z. Liu, and Y. Li, "Fabrications and performance of wireless LC pressure sensors through Itcc technology," *Sensors*, vol. 18, no. 2, 2018. [Online]. Available: <http://www.mdpi.com/1424-8220/18/2/340>
- [130] M. Boada, A. Lazaro, R. Villarino, and D. Girbau, "Battery-less NFC sensor for pH monitoring," *IEEE Access*, vol. 7, pp. 33 226–33 239, 2019.
- [131] K. Opasjumruskit, T. Thanthipwan, O. Sathusen, P. Sirinamarattana, P. Gadmanee, E. Pootarapan, N. Wongkomet, A. Thanachayanont, and M. Thamsirianunt, "Self-powered wireless temperature sensors exploit RFID technology," *IEEE Pervasive computing*, no. 1, pp. 54–61, 2006.
- [132] *EPC C1 G2 compliant UHF RFID tag with power harvesting and SPI communication for external low power sensors and actuators, ANDY100*, Farsens, 3 2016, v09.
- [133] *RFMicron Magnus S3 Sensor IC*, RFMicron, 2015, pB003P11.
- [134] *Higgs4 IC EPC Global Compliant Class-1 Generation-2*, Alien, 6 2014, rev. 1.3.5.
- [135] S. Naderiparizi, A. N. Parks, Z. Kapetanovic, B. Ransford, and J. R. Smith, "Wispcam: A battery-free rfid camera," in *2015 IEEE International Conference on RFID (RFID)*, April 2015, pp. 166–173.
- [136] H. Huang, P.-Y. Chen, C.-H. Hung, R. Gharpurey, and D. Akinwande, "A zero power harmonic transponder sensor for ubiquitous wireless μ l liquid-volume monitoring," *Scientific reports*, vol. 6, no. 1, pp. 1–10, 2016.
- [137] S. Mondal, D. Kumar, S. Karuppuswami, and P. Chahal, "A harmonic rf phase-shifter based wireless ph sensor," in *2018 IEEE 68th Electronic Components and Technology Conference (ECTC)*, 2018, pp. 796–801.
- [138] D. Kumar, S. Mondal, Y. Deng, and P. Chahal, "Wireless battery-free harmonic communication system for pressure sensing," *Micromachines*, vol. 11, no. 12, 2020. [Online]. Available: <https://www.mdpi.com/2072-666X/11/12/1043>
- [139] *NPI-19 Series Medium Pressure Sensor*, NOVA Sensor, 12 2015.

- [140] *MIXED SIGNAL MICROCONTROLLER*, Texas Instruments, 1 2012, sLAS578J.
- [141] C. Ding, A. A. H. Damen, and P. P. J. van den Bosch, “Robust vibration isolation by frequency-shaped sliding surface control with floor velocity/acceleration measurement,” in *IECON 2010 - 36th Annual Conference on IEEE Industrial Electronics Society*, Nov 2010, pp. 1627–1632.
- [142] J. P. Sebastia, J. A. Lluch, J. R. L. Vizcaino, and J. S. Bellon, “Vibration detector based on gmr sensors,” *IEEE Transactions on Instrumentation and Measurement*, vol. 58, no. 3, pp. 707–712, March 2009.
- [143] *TDC1000 Ultrasonic Sensing Analog Front End (AFE) for Level Sensing, Flow Sensing, Concentration Sensing, and Proximity Sensing Applications*, Texas Instruments, 8 2015, sNAS648B.
- [144] *TDC7200 Time-to-Digital Converter for Time-of-Flight Applications in LIDAR, Magnetostrictive and Flow Meters*, Texas Instruments, 3 2016, sNAS647D.
- [145] M. M. Islam, K. Rasilainen, and V. Viikari, “Implementation of sensor rfid: Carrying sensor information in the modulation frequency,” *IEEE Transactions on Microwave Theory and Techniques*, vol. 63, no. 8, pp. 2672–2681, Aug 2015.
- [146] S. M. Noghabaei, R. L. Radin, Y. Savaria, and M. Sawan, “A high-efficiency ultra-low-power cmos rectifier for rf energy harvesting applications,” in *2018 IEEE International Symposium on Circuits and Systems (ISCAS)*, May 2018, pp. 1–4.
- [147] P. Chahal, F. Morris, and G. Frazier, “Zero bias resonant tunnel schottky contact diode for wide-band direct detection,” *IEEE Electron Device Letters*, vol. 26, no. 12, pp. 894–896, Dec 2005.
- [148] *NTC Thermistors, NCP18WM474J03RB*, muRata, 8 2018, <https://www.murata.com/>.
- [149] *CDS Photoconductive Photocells, PDV-P7002*, Luna Optoelectronics, 4 2016, <https://lunainc.com/wp-content/uploads/2016/06/PDV-P7002.pdf>.
- [150] D. Kumar, S. Mondal, S. Karuppuswami, Y. Deng, and P. Chahal, “Harmonic rfid communication using conventional uhf system,” *IEEE Journal of Radio Frequency Identification*, pp. 1–1, 2019.
- [151] *EPC™ Radio-Frequency Identity Protocols Generation-2 UHF RFID*, GS1 EPC global Inc, 4 2015, version 2.0.1.